On intraseasonal variability in the tropics: tropical cyclones, the Madden-Julian Oscillation, and equatorial waves

by

Jonathan Lin

B.S.E., Princeton University (2017)

Submitted to the Department of Earth, Atmospheric and Planetary Sciences
in partial fulfillment of the requirements for the degree of

Doctor of Philosophy

at the

MASSACHUSETTS INSTITUTE OF TECHNOLOGY

December 2021

Author .....
Department of Earth, Atmospheric and Planetary Sciences
December 20, 2021

Certified by .....
Kerry Emanuel
Cecil & Ida Green Professor of Atmospheric Sciences
Thesis Supervisor

Accepted by .....
Robert D. van der Hilst
Schlumberger Professor of Earth and Planetary Sciences
Head of Department of Earth, Atmospheric, and Planetary Sciences

On intraseasonal variability in the tropics: tropical cyclones, the Madden-Julian Oscillation, and equatorial waves

by

Jonathan Lin

Submitted to the Department of Earth, Atmospheric and Planetary Sciences
on December 20, 2021, in partial fulfillment of the
requirements for the degree of
Doctor of Philosophy

Abstract

This dissertation addresses some aspects of tropical intraseasonal variability, which is dominated by tropical cyclones, equatorial waves, and the Madden-Julian Oscillation (MJO). Because these phenomena have significant societal impacts on sub-seasonal time scales, and it is important to understand how they interact with the large-scale atmosphere. The first part of this thesis develops Forecasts of Hurricanes using Large Ensemble Output (FHLO), a large-ensemble, probabilistic tropical cyclone forecast model. FHLO incorporates the state-dependent forecast uncertainty by sampling the internal variability of ensemble numerical weather prediction models. It is shown that including state-dependent forecast uncertainty can lead to significant improvements in pointwise wind speed forecasts on lead times longer than around 3-days. The second part of this thesis addresses how tropical disturbances interact with the stratosphere. A linear framework in which a convecting, quasi-equilibrium troposphere is coupled to a dry, passive stratosphere is developed. It is shown that smaller scale waves are strongly damped by the stratosphere, while slower propagating waves, such as Rossby waves and the MJO, are less affected by the stratosphere. Excitation of the barotropic mode by the stratosphere and surface friction is also analyzed. In particular, it is found that surface friction can excite the barotropic mode far away from the equator, though the poleward extent of the barotropic mode is strongly controlled by how much energy leaks into the stratosphere. The last part of this thesis extends the linear framework to include non-zero zonal wind in the stratosphere, to understand how stratospheric circulations, like the Quasi-Biennial Oscillation, can influence the strength of the MJO. It is found that the tropospheric barotropic mode can be phase-shifted by stratospheric winds, but only under unrealistic forcings at the tropopause. Upward wave radiation is found to be stronger under easterly than westerly winds in the stratosphere, because of increased upward energy flux by Kelvin waves. The effect of the stratosphere on cirrus clouds is also investigated. It is shown that dynamical modulation of lower stratospheric clouds, and anomalous advection of upper-tropospheric ice clouds, can explain why the MJO is stronger under easterly than westerly phases of the QBO.

Thesis Supervisor: Kerry Emanuel
Title: Cecil & Ida Green Professor of Atmospheric Sciences

Acknowledgments

First, I would like to thank my advisor, Kerry, for graciously giving me the opportunity to study atmospheric science and patiently allowing me the freedom to explore a variety of topics. I cannot count the number of times I have sought his advice, and his mentorship has greatly shaped the scientist I am today. In addition, I am also thankful for the guidance of my thesis committee, Tim Cronin, Glenn Flierl, and Adam Sobel, all of whom gave me thoughtful advice on how to improve various aspects of my work. I would also like to thank Jonathan Vigh and the entire HFIP team, who welcomed me to spend a summer at NCAR through the ASP Graduate Visitor program. The mentorship and support Jonathan has provided me throughout graduate school has been very valuable. I have learned a great deal since starting at MIT, and am grateful for the intellectually stimulating environment that is EAPS.

The research presented in this thesis would not be possible without the gracious financial support of a number of sources: the American Meteorological Society fellowship, the Norman C. Rasmussen fellowship, the MIT EAPS Charney prize, the NSF grant ICER-1854929, and the NOAA HFIP grant NA18NWS4680058. I am also thankful for the ensemble weather data used in chapter 2, which was only possible through the effort of the TIGGE (The Interactive Grand Global Ensemble) program.

I will always be grateful for a number of friendships that may have started at different points in my life, but all grew stronger throughout my time at MIT. In no particular order, Amir, Daniel, David, Derek, Diana, Eric X., Ibanca, Julia P., Julia W., Laura, Matthieu, Minseung, Mohammed, Monika, Pritpal, Raj, Raphael, Rohini, Roy, Sophia, Sydney, Tom, Vibhaa.

Finally, I am eternally grateful for the love and support of my father Senshang, my mother Chingchyi, and my brother Spencer. This PhD would not be possible without their constant belief in me.

During the pandemic quarantine, I found a letter I wrote in second grade, which stated "when I grow up, I want to be a weather scientist". I didn't understand what it meant back then, but now I do. Some dreams do come true.

Contents

Chapter 1

Introduction

Intra-seasonal variability describes variations in weather on time-scales less than a season. In the tropics, or locations that generally lie between the Tropics of Cancer ($\approx 23°$N) and Tropics of Capricorn ($\approx 23°$S), intra-seasonal variability is dominated by tropical cyclones, the Madden Julian oscillation (MJO), and equatorial waves. Understanding the dynamics of these pheneomena is vital to answering questions such as why tomorrow, next week, or even next month will be windier, rainier, or cloudier than usual. Using both applied and theoretical approaches, this thesis attempts to take a small step towards improving our understanding of a few aspects of intraseasonal variability in the tropics.

1.1 Tropical Cyclones

Tropical cyclones (TCs), or hurricanes in the Western hemisphere, are low-pressure storms that bring extreme winds, rainfall, and storm surge to coastal locations around the world. Each year, numerous lives and billions of dollars in damage are lost to TC impacts (Pielke et al., 2008). To mitigate losses and allow societies to undertake life-saving precautions, TC forecasts must be provided with sufficient lead-time and be reasonably accurate and reliable.

However, because atmospheric flow is chaotic, there is always inherent uncertainty in weather forecasts, especially when considering weather impacts at a fixed point in

space. For instance, it is not uncommon for one to check their phone to look at the daily weather report and see a 50% chance of rain. This is a probabilistic forecast: it does not state that it will or will not rain, but rather, the chance of rain, which allows us to quantify uncertainty. For extreme weather events like tropical cyclones, it is not only important to communicate the *potential* of high-impact weather, but also the *uncertainty* in the forecast. Unfortunately, it is not straightforward to derive forecast probabilities for tropical-cyclone associated weather at a single point. The first step towards point-wise probabilistic tropical cyclone forecasts was undertaken by DeMaria et al. (2009) (affiliated with the National Hurricane Center), who developed a model to predict the probability that tropical-cyclone induced wind speeds would exceed a certain threshold at a fixed location.

In chapter 2, I develop and evaluate a probabilistic tropical cyclone forecast model, FHLO (Forecasts of Hurricanes using Large-Ensemble Output). Unlike the probabilistic wind speed model of the National Hurricane Center, which samples uncertainty from a climatological error distribution, this model generates uncertainty by sampling spread from ensemble numerical weather prediction (NWP) models using a large number of ensemble members. After incorporating the state-dependent uncertainty in large-scale flow (as sampled by the ensemble NWP models, we found that forecasts of exceedance wind speeds, or the probability that the wind will exceed a certain threshold, were improved on lead times greater than 3 days. This chapter was published in Weather and Forecasting.[1]

1.2 Equatorial Waves and the MJO

Long before satellite observations of the tropics became available, Taroh Matsuno predicted the presence of tropical waves that propagate eastward and westward along the equator (Matsuno, 1966). It was not until the work of Wheeler and Kiladis (1999) that the existence of a broad spectrum of equatorial waves became well known: anal-

[1]Chapter 2 is an edited version of: Lin, J., K. Emanuel, and J. L. Vigh, 2020: Forecasts of Hurricanes Using Large-Ensemble Outputs. *Weather and Forecasting* **35 (5)**, 1713-1731.

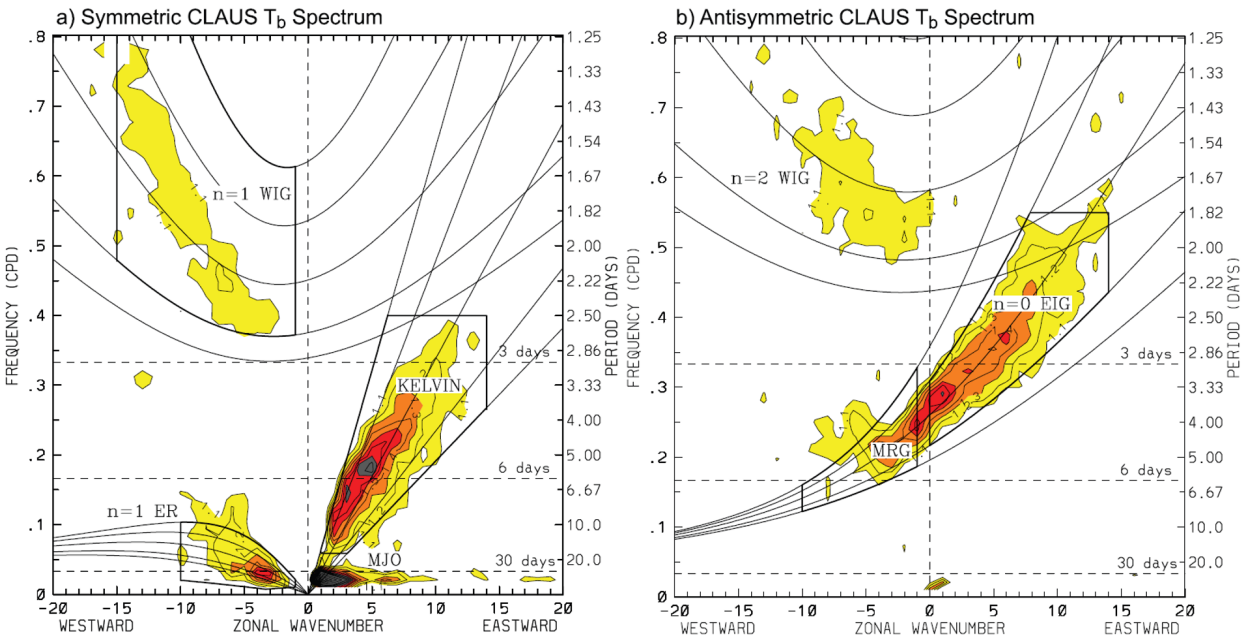

Figure 1-1: Wave number-frequency power-spectrum ratio of the (a) symmetric and (b) antisymmetric brightness temperatures from July 1983 to June 2005. Ratio is calculated by dividing the raw power by a smoothed background spectrum. Shading begins where the signals are significant at greater than the 95% level. Dispersion curves of neutral equatorial waves overlaid. Figure adapted from Kiladis et al. (2009).

yses of satellite observations of brightness temperatures show that, in wave number-frequency space, there are prominent peaks along the dispersion curves of the linear, neutral equatorial modes (see Figure 1-1) that Matsuno had predicted more than 30 years prior. Matsuno (1966) was the first to show the complete set of linear solutions to the inviscid shallow water equations on a beta plane:

$$\frac{\partial u}{\partial t} - fv = -\frac{\partial \phi}{\partial x}$$
$$\frac{\partial v}{\partial t} + fu = -\frac{\partial \phi}{\partial y}$$
$$\frac{\partial \phi}{\partial t} + c^2\left(\frac{\partial u}{\partial x} + \frac{\partial v}{\partial x}\right) = 0$$

where u is the zonal velocity, v is the meridional velocity, ϕ is the geopotential, $c = \sqrt{gH}$ is the gravity wave speed, and the Coriolis parameter $f = f_0 + \beta y$. Assuming equatorial motion ($f_0 = 0$), the equations can be combined to eliminate u and ϕ to

obtain:

$$\frac{1}{c^2}\frac{\partial^3 v}{\partial t^3} - \frac{f^2}{c^2}\frac{\partial v}{\partial t} - \frac{\partial}{\partial t}\Big(\frac{\partial^2 v}{\partial x^2} + \frac{\partial^2 v}{\partial y^2}\Big) - \beta\frac{\partial v}{\partial x} = 0$$

If we search for solutions of $v = V(y)\exp(i(kx - \omega t))$, the resulting dispersion relation is:

$$\frac{\partial^2 v}{\partial t^2} + \Big(\frac{\omega^2}{c^2} - k^2 - \frac{\beta k}{\omega} - \frac{\beta^2 y^2}{c^2}\Big)v = 0$$

The solutions to these are parabolic cylinder functions, which have the form, $D_m(y) = H_m(y)\exp(-y^2/2)$, where $H_m(y)$ are Hermite polynomials of order m. This dispersion relation supports a beautiful spectrum of equatorial waves, including Rossby waves, Kelvin waves, gravity waves, and mixed Rossby-gravity waves (Yanai waves), as shown from the dispersion curves in Figure 1-1.

An immediate question one might ask is why the shallow water equations can so accurately predict the power spectrum of equatorial waves in the tropics. After all, even without other forms of damping, these waves are neutral, i.e. they are not unstable and do not grow in the tropical atmosphere. To start, we look at the correspondence between the shallow water equations and the primitive equations. The shallow water equations can be derived from the linearized, hydrostatic, continuously stratified Boussinesq equations, under the mathematical assumption that the vertical structure of the solutions are separable from the time-varying and horizontal components of the flow (of course, the boundaries then become important in setting the vertical modes, as we shall see later). The solution to the vertical structure of the flow reduces to a Sturm-Liouville form, in which the infinite number of vertical eigenfunctions are complete and orthogonal. Because of this property, each vertical eigenfunction can be considered separately, reducing the primitive equations to shallow water form. The eigenvalues associated with these eigenfunctions set the "equivalent depth" of each vertical mode. Thus, when "forcing" is confined to one particular vertical mode, the shallow water equations can serve as a useful approximation for atmospheric flow.

What is the extent to which these assumptions hold in the tropics? To answer this, we look to the the convective statistical equilibrium hypothesis, which holds that the rate of production of convectively available potential energy (CAPE) by the large-

scale environment is very nearly balanced by its consumption via convection (Arakawa and Schubert, 1974). A stronger corollary of this hypothesis is that the vertical temperature profile in the tropics is very nearly moist-adiabatic - moist convection determines the lapse rate. Indeed, observations in the tropics support the statistical equilibrium model for convection in the tropics (Betts, 1982; Xu and Emanuel, 1989). This means that the vertical structure in the tropics can indeed be approximated as a single vertical mode.

We can also show this mathematically. Under the assumption that the lapse rate in the troposphere is strictly neutral to moist convection (an assumption we will call strict quasi-equilibrium), the saturation moist entropy, s^*, becomes constant with height. Combining this with hydrostatic balance and linearizing yields (Emanuel, 1987):

$$\frac{\partial \phi'}{\partial p} = -\left(\frac{\partial T}{\partial p}\right)_{s^*} s^{*\prime} \tag{1.1}$$

Since s^* is constant in height, the above may be directly integrated from the surface upwards to yield:

$$\phi'(p) = [\phi'] + s^{*\prime}([T(p)] - T(p)) \tag{1.2}$$

where primes indicate perturbation quantities, bracketed quantities are pressure-weighted vertical averages, and $[T(p)]$ is the vertically averaged mean temperature following a moist adiabat. This is a remarkable approximation: it shows the geopotential vertical structure is a sum of two components, a *barotropic* component that is independent with height, and a *baroclinic* mode that is only a function of temperature differences from the vertically averaged temperature. Since heating is typically confined to the baroclinic mode (as a consequence of moist convection), it now seems reasonable that the shallow water equations can reasonably represent the real tropical atmosphere.

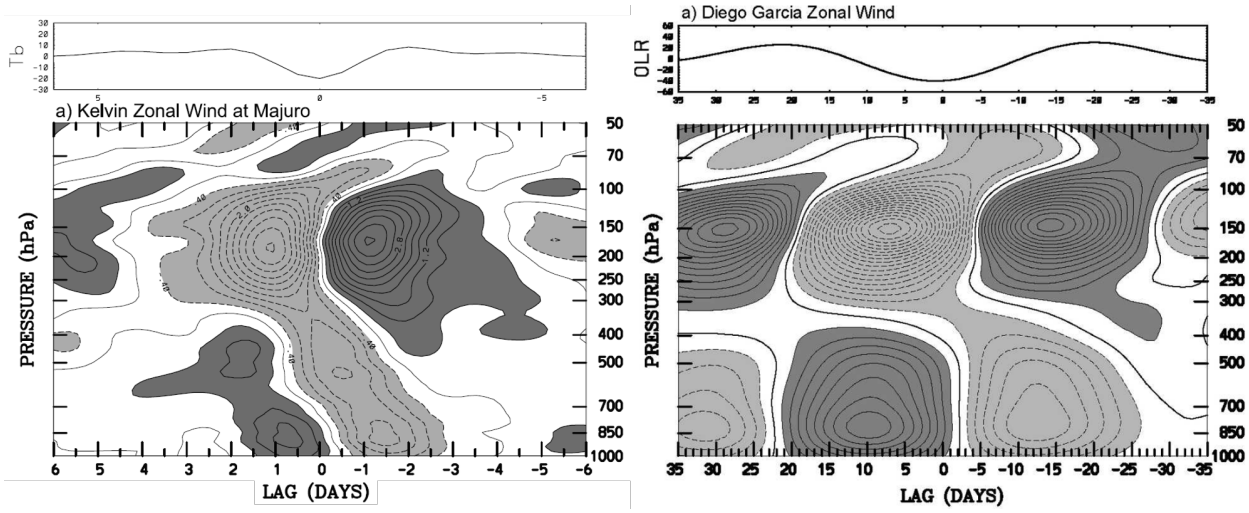

Figure 1-2: (Left) Time-height cross-section of zonal wind anomalies associated with Kelvin waves, from radiosonde data at Majuro (7.1°N, 171.4°E). (Right) Same as left but for zonal wind anomalies associated with the MJO, at Diego Garcia (7.3°S, 72.4°E). Adapted from figure 8 of Kiladis et al. (2005) and figure 4 of Kiladis et al. (2009)

There are still a number of outstanding questions, however. To start, the MJO does not lie on any dispersion relation curve from the original Matsuno equations. In addition, observations of equatorial waves indicate the presence of vertical modes other than the baroclinic mode. Figure 1-2 shows zonal wind anomalies associated with Kelvin waves and the MJO, using data from radiosondes at tropical islands (Kiladis et al., 2005, 2009). For the Kelvin wave, there is a baroclinic mode structure, but also a westward tilt with height in the lower troposphere that indicates the presence of an additional vertical mode. For the MJO, there is a strong first baroclinic mode structure, and possibly a barotropic mode of much smaller magnitude.

In addition, the rigid-lid approximation is often used to simply mathematical treatment of equatorial waves. The rigid-lid approximation assumes that there is a fixed, unmoving boundary at the tropopause. This is quite far from the truth. Though the stratosphere has a larger stratification than the troposphere, its stratification is not infinite, and there is undoubtedly energy propagation from the troposphere to the stratosphere. There are signals of this occurring in radiosonde data shown in Figure

1-2.

Chapters 3 and 4 of this thesis attempts to answer a few of these outstanding questions:

- **What about the barotropic mode**? The barotropic mode has often been ignored in equatorial wave dynamics. But, it can clearly still be excited even under strict quasi-equilibrium models. What is the extent to which the barotropic mode can couple with the baroclinic mode? Does it significantly change the structure and growth rate of equatorial waves? (Chapter 3)

- **How do equatorial waves interact with the stratosphere**? Yano and Emanuel (1991) showed that the stratosphere selects for larger scale $v = 0$ waves. Does this result generalize to all equatorial waves? (Chapter 3)

- **How does the MJO interact with the stratosphere**? Since the MJO propagates very slowly, does it negligibly interact with the stratosphere? In addition, recent analyses of observations indicate that the MJO is strongly modulated by an oscillatory pattern of wind in the stratosphere known as the Quasi Biennial Oscillation (QBO). How can we understand the mechanisms through which stratospheric winds control tropospheric organized convection? (Chapter 4)

In chapter 3, I formulate an idealized, theoretical framework to investigate the effect stratospheric coupling and surface friction have on equatorial waves. Previous work analyzed the presence of the stratosphere on a small subset of equatorial waves, the Kelvin wave, and found that the stratosphere has a strong damping effect on smaller scale equatorial waves, since these waves propagate very quickly into the stratosphere (Yano and Emanuel, 1991). In this chapter, I extend the results of Yano and Emanuel (1991) to higher orders of equatorial waves. In particular, I coupled a strict quasi-equilibrium troposphere to a dry passive stratosphere, and looked for wave-like, linear solutions. I found that the stratosphere can also act as a significant scale selection mechanism for eastward propagating Kelvin, mixed Rossby-gravity,

and gravity waves. On the other hand, I found that the stratosphere has a negligible effect on westward propagating Rossby waves, as well as slow, eastward propagating disturbances like the MJO. Surface friction is found to act purely as a damping mechanism for equatorial waves. This chapter was accepted for publication in the Journal of Atmospheric Science.[2]

While the work of Chapter 3 formulates a framework by which to understand coupled troposphere-stratosphere interactions in the tropics, it does so under a zero mean stratospheric wind. The zonal wind in the stratosphere is, in fact, non-zero, which has a number of significant effects on the troposphere. For example, the Quasi-Biennial Oscillation, a stratospheric mode of variability in which the lower stratospheric zonal winds shift between easterlies and westerlies approximately every 28 months (Baldwin et al., 2001), has been observed to modulate the strength of the MJO (Yoo and Son, 2016). Chapter 4 extends the linear framework to include non-zero mean wind in the stratosphere, and uses the framework to investigate mechanisms that are responsible for this puzzling connection. In particular, I analyze how the mean wind in the stratosphere can modulate (1) the magnitude of upward wave radiation and (2) cirrus-cloud feedbacks, which has been shown to be important to destabilize the MJO (Khairoutdinov and Emanuel, 2018). Under linear dynamics, I show that the wave-energy loss to the stratosphere is stronger under easterly winds, which results in a stronger MJO under westerly stratospheric winds. This, however, is opposite of the observed relationship, where the MJO is stronger under easterly stratospheric winds. I then develop a prognostic equation for cirrus clouds, and show that (1) dynamical modulation of cirrus clouds by upward propagating waves and (2) advection of high clouds by the background zonal wind, can lead to damping of the MJO under westerly flow in the stratosphere. This chapter has been submitted for publication in the Journal of Atmospheric Science.

Finally, the conclusion summarizes the main results from this thesis. I also outline some future directions to take this research.

[2]Chapter 3 is an edited version of: Lin, J., and K. Emanuel, 2022: On the Effect of Surface Friction and Upward Radiation of Energy on Equatorial Waves. *Journal of Atmospheric Science*. Accepted for publication.

Chapter 2

Forecasts of Hurricanes using Large-Ensemble Outputs

Abstract

This chapter describes the development of a model framework for Forecasts of Hurricanes using Large-ensemble Outputs (FHLO). FHLO quantifies the forecast uncertainty of a tropical cyclone (TC) by generating probabilistic forecasts of track, intensity, and wind speed that incorporate the state-dependent uncertainty in the large-scale field. The main goal is to provide useful probabilistic forecasts of wind at fixed points in space, but these require large-ensembles (O(1000)) to flesh out the tails of the distributions. FHLO accomplishes this by using a computationally inexpensive framework, which consists of three components: (1) a track model that generates synthetic tracks from the TC tracks of an ensemble numerical weather prediction (NWP) model, (2) an intensity model that predicts the intensity along each synthetic track, and (3) a TC wind field model that estimates the time-varying two-dimensional surface wind field. The intensity and wind field of a TC evolve as though the TC were embedded in a time-evolving environmental field, which is derived from the forecast fields of ensemble NWP models. Each component of the framework is evaluated using 1000-member ensembles and four years (2015-2018) of TC forecasts in the Atlantic and Eastern Pacific basins. We show that the synthetic track algorithm generates tracks that are statistically similar to those of the underlying global ensemble models. We show that FHLO produces competitive intensity forecasts, especially when considering probabilistic verification statistics. We also demonstrate the reliability and accuracy of the probabilistic wind forecasts. Limitations of the model framework are also discussed.

2.1 Introduction

Tropical cyclones (TCs) are complex weather systems that bring flooding, storm surge, high winds, and other hazards to many coastal and island locations. Each year, TCs cause billions of dollars in damage to businesses and property and result in the loss of numerous lives (Pielke et al., 2008). To mitigate such losses and allow vulnerable populations to undertake life-saving preparations, TC forecasts must be provided with sufficient lead-time and be reasonably accurate and reliable. Forecasts of TCs have traditionally been separated into two categories: (1) track forecasts, which predict the location of the TC center, and (2) intensity forecasts, which, in the Atlantic basin, predict the 1-minute maximum sustained surface wind anywhere in the storm (Landsea and Franklin, 2013). The forecasting community has used such metrics to quantify errors in forecast models. Through substantial model improvements, better observations, and improved data assimilation methods, forecast skills for track and intensity have been steadily improving (DeMaria et al., 2014).

One of the advantages of separating TC forecasts into track and intensity is that it allows for straightforward evaluation of model performance. However, there are some significant drawbacks with this approach. First, by definition, deterministic forecasts do not quantify the uncertainty in the track and intensity of a TC, which can be an issue if the intensity of the TC strongly depends on its track. The concept of quantifying forecast uncertainty is not new. In 1992, the National Meteorological Center (NMC) and the European Center for Medium Range Weather Forecasting (ECMWF) began running ensemble numerical weather prediction (NWP) systems to forecast the range of future weather conditions, by slightly perturbing the initial conditions and model physics of each member of the ensemble NWP system (Tracton and Kalnay, 1993; Molteni et al., 1996). Since then, ensemble forecasts have proven to be vital to advancing probabilistic forecasts of weather, which in turn allow us to quantify weather-related risks (Gneiting and Raftery, 2005).

The various components of the TC forecast (e.g., track, intensity, size, rainfall) affect the specific hazards (e.g., wind speed, waves, surge inundation, and riverine

flood inundation) that are experienced at a given location. The specific impacts that then result depend on the vulnerability and exposure of the asset at that location. Thus, the ability to quantify the uncertainty of TC wind speed forecasts is of utmost importance, especially for vulnerable communities. Much work on the intrinsic predictability of TCs has focused on the importance of both large-scale influences (Emanuel et al., 2004; Zhang and Tao, 2013; Kieu and Moon, 2016) and convective scale processes (Van Sang et al., 2008; Sippel and Zhang, 2008; Judt et al., 2016). Initial condition uncertainty in the intensity and inner-core moisture has also been suggested to play a significant role in TC forecast uncertainty (Emanuel and Zhang, 2016, 2017). In light of this, deterministic forecasts of TCs may be highly misleading, and probabilistic forecasts that can sample the inherent forecast uncertainty are preferred. It is no surprise, then, that ensemble prediction systems (EPSs) have enhanced probabilistic forecasts of TCs (Majumdar and Finocchio, 2010; Hamill et al., 2011). Another approach to generating members of an ensemble is to combine the predictions of many different, independent, models, as is done for some "super-ensemble" models (Williford et al., 2003; Vijaya Kumar et al., 2003); in fact, even a simple average of the forecasted tracks from a variety of dynamical models has been shown to outperform any of the individual models (Goerss, 2000).

Since the wind field of a TC can span hundreds of kilometers, the position and intensity of a TC are insufficient for specifying the conditions at fixed points. In practice, interested parties should be more concerned about the wind speed probability distribution at a single location (point-wise wind speed probabilities), rather than the TC's maximum wind speed or exact center location. Unfortunately, due to computational constraints, ensemble NWP models are typically run with inadequate horizontal resolution to resolve strong gradients in pressure and temperature that are commonly found in TCs, which often leads to large underestimation of the wind speeds in the simulated TCs (Gentry and Lackmann, 2010; Gopalakrishnan et al., 2011). To make matters worse, an ensemble NWP system usually does not have enough ensemble members to flesh out the highest wind speeds of a point-wise wind distribution. Inadequate horizontal resolution and small ensemble size mean that it is

impractical to use the (insufficiently) resolved wind fields from ensemble NWP models to produce well-resolved probabilistic, point-wise forecasts of wind speeds.

In order to address these issues and communicate the point-wise uncertainty of TC winds, DeMaria et al. (2009) developed the Monte Carlo Probability[1] (MCP) model to estimate the point-wise probability of surface winds exceeding the 34-, 50-, and 64- knot wind speed thresholds. For each forecast, the MCP model generates computationally inexpensive track and intensity realizations by adding random errors to the National Hurricane Center's official forecasts for track, intensity, and wind radii. The errors are sampled from the official forecast track/intensity/wind radii error distributions over the most recent 5 years. However, this method forces the uncertainty in the model to exactly equal the observed average error; in practice, this usually does not reflect the state-dependent uncertainty for a given forecast. Since the forecast uncertainty for each TC can vary greatly, the climatological uncertainty may poorly reflect the true uncertainty in the track/intensity/wind radii forecasts. DeMaria et al. (2013) improved the MCP model to separate the climatological error distributions into three categories, based on the Goerss Predicted Consensus Error (GPCE), a parameter that measures the extent of the track spread among an ensemble system (Goerss, 2007). Goerss (2007) showed that the degree of uncertainty of a forecast could be coarsely predicted based on a low, medium, or high GPCE, and separated the climatological error bins accordingly. While the inclusion of GPCE improved the sharpness of the probabilistic wind forecasts, the MCP model still uses climatologically-based forecast errors (stratified by basin) to generate uncertainty in the official forecast. Ensemble-based uncertainties, on the contrary, characterize the state-dependent uncertainty in the large-scale system. Therefore, a model that is able to draw upon the uncertainty represented in the ensemble members of a NWP model, while maintaining the computationally inexpensive components of the MCP model, could improve on probabilistic wind speed forecasts.

We aim to develop a computationally inexpensive point-wise TC wind speed pre-

[1]The National Hurricane Center's operational version of this model is called the Tropical Cyclone Wind Speed Probabilities Product.

diction framework that is capable of incorporating the state-dependent forecast uncertainty. To be practical, the framework should be capable of quickly generating the large number of ensemble members necessary to create a robust probabilistic forecast. Our proposed framework will address these concerns by using a large ensemble prediction system in which the ensemble members are computationally cheap, stochastic realizations reflecting the uncertainty derived from dynamical ensemble models. Furthermore, our framework is designed to readily scale with advancements in the physics, resolution, and size of ensemble NWP models, especially since there is still much room for improvement in forecasting the intensity of TCs (Emanuel and Zhang, 2016).

The paper is organized as follows. Section 2.2 describes the datasets used in this study. A detailed description of FHLO is provided in section 2.3, followed by an evaluation of the model framework in section 2.4. Section 2.5 concludes with a summary and discussion.

2.2 Data

In this study, we use forecast data from ensemble prediction systems (EPSs) as the primary inputs to FHLO. We use two EPSs in particular: the 51-member global ensemble of the European Center for Medium Range Forecast (ECMWF), and NOAA's 21-member Global Ensemble Forecast System (GEFS). Both ensembles are run multiple times per day and provide an estimate of forecast uncertainty. All ensemble forecast data are obtained from an online portal generously made available by the THORPEX Interactive Grand Global Ensemble (TIGGE) project (Bougeault et al., 2010; Swinbank et al., 2016). The data are obtained on a 0.5° by 0.5° resolution grid. The analyzed tracks of TCs in ensemble forecast models are obtained from the TIGGE Model Tropical Cyclone Track Dataset (National Centers for Environmental Prediction et al., 2008), which is obtained from the Research Data Archive (RDA) maintained by the National Center for Atmospheric Research (NCAR).

We also require initial conditions at each initialization time. For the ECMWF

ensemble, we use the re-analysis fields from the ERA5 atmospheric reanalysis (Hersbach, 2016; Copernicus Climate Change Service, 2017). Note that these fields can have significant differences from the analysis fields of the operational ECMWF model. However, we require high-resolution soundings in order to estimate the potential intensity. Since the high-resolution analysis fields of the operational ECMWF model are not available to the public, we have used the ERA5 fields. For the GEFS, we use the analysis fields from the GFS (Global Forecast System) analysis fields at each model initialization time, obtained through the RDA at NCAR (National Centers for Environmental Prediction, 2015). All analysis fields are obtained on a 0.25 by 0.25 resolution grid. As part of initialization, we also require initialization of the TC itself. To obtain real-time estimates of TC position, intensity, and wind structure, we obtain Automated Tropical Cyclone Forecasting (ATCF) a-decks for each model initialization time (Sampson and Schrader, 2000).

To obtain real-time estimates of the sea-surface temperature, we use the National Centers for Environmental Information's 0.25 Optimum Interpolation Sea Surface Temperature (OISST) dataset (Reynolds et al., 2008). The sea-surface temperature data is provided daily.

Finally, we use the HURDAT2 best-track data to evaluate the performance of the model (Landsea and Franklin, 2013).

2.3 The large-ensemble model for tropical cyclones

In this work, we model TCs by assuming that a TC vortex is embedded within an evolving large-scale environmental field that ultimately determines the TC's intensity. From an ensemble NWP model, such as the Global Ensemble Forecasting System (GEFS), we estimate environmental quantities relevant to the intensity of a TC, such as the saturation entropy deficit and vertical wind shear (Emanuel et al., 2004). By deriving these quantities from multiple members of an ensemble model, we can sample the internal variability in each environmental field. The track module of the large-ensemble model generates realistic tracks from the set of ensemble TC tracks. These

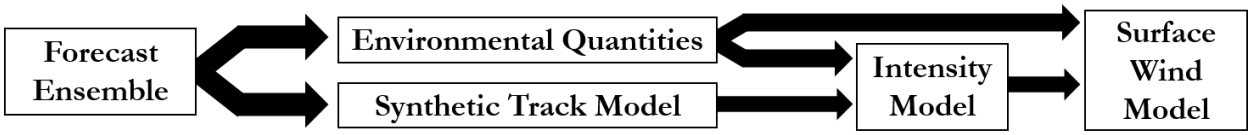

Figure 2-1: Flow of information in FHLO.

tracks, combined with the various environmental fields along these tracks, serve as input into FAST (Emanuel, 2017), a TC intensity model that emulates an idealized, axisymmetric TC model (Emanuel et al., 2004). FAST evaluates the intensity, or maximum azimuthal wind speed, along a specified track through one realization of the large-scale environmental field. Finally, the intensity and environmental fields are used as inputs into a parametric surface wind model, to generate a full spatial wind field of the TC (Chavas et al., 2015). Figure 2-1 summarizes the overall flow of information in the large-ensemble model. Each component of the complete model framework is explained in depth in the following sections.

2.3.1 Synthetic track model

In this section, we describe a track algorithm that draws information from the ensemble track covariance to generate a large number of statistically indistinguishable synthetic tracks. The model is physically motivated by the beta-and-advection model (Marks, 1992), which assumes that TCs are advected by some large-scale steering flow. Since we do not expect the large-scale flow to have considerable fluctuations on short (hourly) time scales, we expect there to be some correlation between the translational speed vector from one time step to the next. Note that the forecasted center of TCs is typically output in 3- or 6-hour increments.

In light of this, we model the distribution of TC translational speeds using a Markov-chain solution. This means we condition on the previous time step translational speed, u_{t-1} and v_{t-1}, where u_{t-1} and v_{t-1} are the zonal and meridional translational speeds at time step $t-1$, respectively, to determine the translational speed at the next discrete time step. Mathematically, this corresponds to $P(u_t, v_t \mid u_{t-1}, v_{t-1})$.

To properly describe this conditional distribution, we expand this as:

$$P(u_t, v_t \mid u_{t-1}, v_{t-1}) = \frac{P(u_{t-1}, v_{t-1}, u_t, v_t)}{P(u_{t-1}, v_{t-1})}$$

Next, we model both joint probability distributions as a mixture of k Gaussian distributions:

$$P(u_{t-1}, v_{t-1}, u_t, v_t) = \sum_{i=1}^{k} w_i N(\boldsymbol{\mu}_i, \boldsymbol{\Sigma}_i)$$

$$P(u_{t-1}, v_{t-1}) = \sum_{j=1}^{m} w_j N(\boldsymbol{\mu}_j, \boldsymbol{\Sigma}_j)$$

where w_i are the weights of each Gaussian mixture, such that $\sum_{i=1}^{k} = 1$. The quantities $\boldsymbol{\mu}_i$, $\boldsymbol{\mu}_j$, $\boldsymbol{\Sigma}_i$, and $\boldsymbol{\Sigma}_j$ must be estimated using the track displacements from the ensemble model. In this study, we set $k = 1$, though future work can explore how increasing k affects the track model.

Given (u_{t-1}, v_{t-1}), we can step the model forward by drawing from the conditional probability above. Integrating forwards in time will generate a synthetic track. The statistical algorithm is relatively fast, as 1000 synthetic tracks can be generated in approximately five minutes on a conventional laptop. For robustness, we require that at least 75% of the global ensemble member tracks have not dissipated before proceeding to the next time step.

Note that this method directly depends on the skill of the ensemble prediction system. While this means that the accuracy of the ensemble covariance algorithm should scale alongside the general accuracy of ensemble NWP models, it also indirectly ties the track algorithm to how accurately the ensemble NWP models simulate the intensity of the analyzed TC. If the TC dissipates too early in the ensemble prediction model, the ensemble track covariance model will generate tracks that also dissipate too early.

Since a potentially unlimited number of synthetic tracks can be generated, robust probabilistic statistics can also be generated. Figure 2-2 shows an example of the corresponding 75-km strike probability for the forecast of Hurricane Irma (2017),

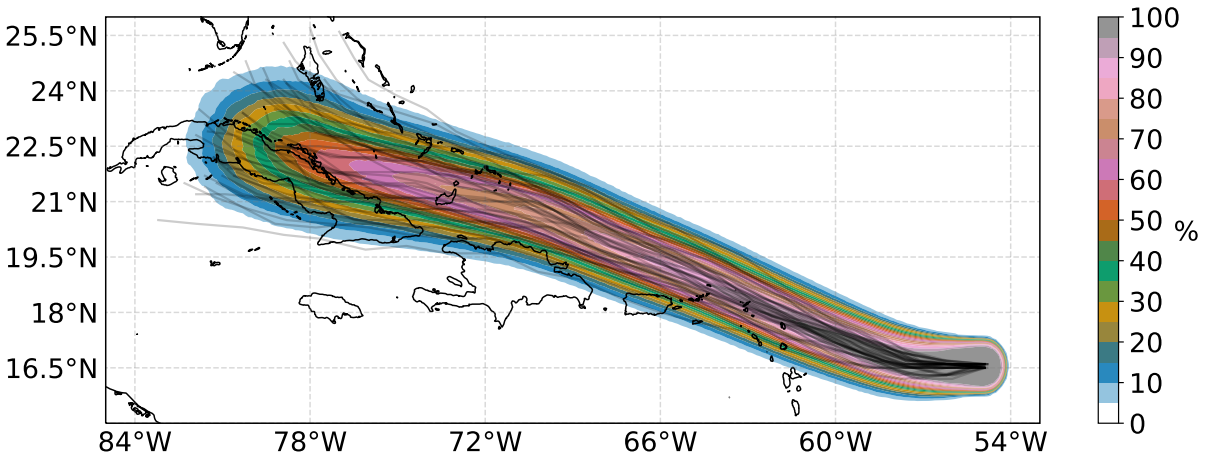

Figure 2-2: 75-km strike probability, for Hurricane Irma in the Atlantic Basin, using 1000 synthetic tracks generated from the ECMWF ensemble. Forecast initialized at 00 UTC on 05 September 2017. Overlaid lines depict TC centers from the ECMWF ensemble.

initialized at 00 UTC on 05 September 2017. While we observe that the density of the 75-km strike probability corresponds well with the density of the actual ensemble tracks for this single case, a large sample size with probabilistic evaluation is needed to fully evaluate the quality of the framework's track predictions. This will be further examined in Section 2.4.4.

2.3.2 Intensity model

The intensity model evaluates the surface azimuthal wind speed along a particular track. Though any computationally inexpensive intensity model can be used in the large-ensemble framework, we choose to use the FAST system, a pair of coupled, non-linear ordinary differential equations that describe the evolution of V, the maximum azimuthal wind, and m, an inner core moisture variable that is bounded between 0 and 1 (Emanuel and Zhang, 2017; Emanuel, 2017). The choice was motivated primarily because the system is framed around physically-based parameters that can be easily

derived from ensemble fields. The equations are included below:

$$\frac{dV}{dt} = \frac{1}{2}\frac{C_k}{h}\Big[\underbrace{\alpha\beta V_p^2 m^3}_{(1)} - \underbrace{(1-\gamma m^3)V^2}_{(2)}\Big] \tag{2.1}$$

$$\frac{dm}{dt} = \frac{1}{2}\frac{C_k}{h}\Big[\underbrace{(1-m)V}_{(3)} - \underbrace{\chi S m}_{(4)}\Big] \tag{2.2}$$

$$\beta = 1 - \epsilon - \kappa \tag{2.3}$$

$$\gamma = \epsilon + \alpha\kappa \tag{2.4}$$

$$\epsilon = \frac{T_s - T_o}{T_s} \tag{2.5}$$

$$\kappa = \frac{\epsilon}{2}\frac{C_k}{C_d}\frac{L_v}{R_d}\frac{q_s^*}{T_s} \tag{2.6}$$

where C_k is the surface enthalpy coefficient, C_d is the surface drag coefficient, h is the atmospheric boundary layer depth, V_p is the potential intensity, α is an ocean interaction parameter which varies between 0 and 1, χ is the mid-level saturation entropy deficit, S is the 250-850-hPa vertical wind shear, T_s is the surface temperature, T_o is the outflow temperature, L_v is a constant latent heat of vaporization, R_d is the dry gas constant, q_s^* is the surface saturation specific humidity, and ϵ is the thermodynamic efficiency [see Emanuel (2017) for further details]. Note that in Emanuel (2017), $\chi = 2.2$, which is a typical value for the saturation entropy deficit, but as discussed presently, we will evaluate its time-evolving value from the global ensemble. The behavior of this system is controlled by four key terms: (1) a spin-up term that represents intensification of the vortex toward its potential intensity because of surface fluxes, (2) a spin-down term from the thermodynamic dampening influence of down-drafts in the inner core, (3) a moistening term that represents surface moisture fluxes from the ocean, and (4) a drying term that mimics eddy entropy fluxes into the TC's eyewall. Though remarkably simple, the FAST equations do have some limitations, which are discussed in the conclusion.

The FAST equations are integrated forwards in time using a Runge-Kutta 4th order numerical scheme with a time step of 450 seconds. As in Emanuel (2017), we set $C_k = 1.2 \times 10^{-3}$, $h = 1400$ m, $\epsilon = 0.33$, $\kappa = 0.1$. Thus, given an initial intensity

and inner core moisture, as well as the vertical wind shear, saturation entropy deficit, and potential intensity along a track, we can solve for the time evolution of V and m. It is worth nothing that in order to properly calculate α, the ocean interaction parameter that modulates V_p, one needs the ocean mixed layer depth, h_m, as well as the sub-mixed layer thermal stratification, Γ. For simplicity, we choose to use climatological values for h_m and Γ (Levitus, 1982). Future work will incorporate this information from a real-time ocean forecast model. Ocean mixing is switched off whenever the sub-mixed layer depth is larger than the depth of the ocean. Finally, a 0.25 bathymetric dataset is used to determine when the center of the TC is over land, during which the potential intensity is set to zero.

In this framework, the three most important environmental quantities that influence the intensity of a TC are: (1) vertical wind shear, (2) saturation entropy deficit, and (3) potential intensity. These dynamic and thermodynamic quantities are defined to be environmental fields, and thus should be evaluated assuming that the considered TC does not exist. In order to progress with the perspective of modeling a TC in a synthetic environment, we need to remove any effects on these fields that are induced by an analyzed TC.

2.3.3 Environmental quantities

Vertical wind shear

In order to calculate the environmental vertical wind shear, the circulation induced by the TC must be removed. One method, for instance, averages winds over some distance larger than the radius of the inner core of the TC (DeMaria and Kaplan, 1994), while other methods set the vorticity and divergence to zero within a specified distance from the TC center, and invert the Poisson equation to find the streamfunction and velocity potential associated with the vortex (Davis et al., 2008; Galarneau and Davis, 2013). Since we desire a continuous spatial field of environmental winds, $\mathbf{u}_{env}$, we choose the latter method, setting the relative vorticity and divergence of the environmental field to zero within an inversion radius of r^* from the vortex center. We

use $r^* = 400$ km, where the magnitude of the axisymmetric component of the vortex's relative vorticity becomes comparable to that of the environmental field. Note that $r^* = 400$ km is around the middle range of r^* values used by Galarneau and Davis (2013), and close to the median outer radius of TCs, inferred using scatterometer data (Chavas and Emanuel, 2010). Fixing r^* is perhaps not the best choice, as Galarneau and Davis (2013) showed that the resulting environmental winds are in fact sensitive to r^*. Future work could include stochastic perturbations to r^*, or optimizing r^* from environmental profiles of relative vorticity. Defining ζ_{vortex} and δ_{vortex} as the vorticity and divergence identified as part of the vortex, respectively, we have:

$$\begin{aligned} \nabla^2 \psi_{vortex} &= \zeta_{vortex} \\ \nabla^2 \Phi_{vortex} &= \delta_{vortex} \\ \mathbf{u}_{vortex} &= \nabla \Phi_{vortex} + \hat{k} \times \nabla \psi_{vortex} \\ \mathbf{u} &= \mathbf{u}_{env} + \mathbf{u}_{vortex} \end{aligned} \tag{2.7}$$

where $\mathbf{u}$ is the wind velocity vector, ψ is the streamfunction, Φ is the velocity potential, ∇ is the gradient operator, and ∇^2 is the Laplacian operator. To solve for $\mathbf{u}_{vortex}$, we must invert the Laplacian operator on a sphere to obtain the corresponding streamfunction and velocity potential. Details on this inversion are included in the appendix. After calculation of the environmental wind at 250-hPa and 850-hPa, we subtract the two to obtain the environmental vertical wind shear. We chose these two levels based on DeMaria and Kaplan (1994), who found that the vertical wind shear between the 250-hPa and 850-hPa levels correlates well with intensity changes in tropical cyclones, though alternative pressure levels could also be used to calculate the vertical wind shear.

Mid-level ventilation

Mid-level ventilation, or the entrainment of low-entropy environmental air into a TC at mid-levels, is one pathway by which vertical wind shear can interact with a TC and cause it to weaken (Simpson and Riehl, 1958; Tang and Emanuel, 2010). In

the ventilation hypothesis, vertical wind shear leads to asymmetric processes that induce eddy fluxes and mixing between the TC eyewall and its environment. If the environmental air is sufficiently low in entropy, downdrafts will occur in the eyewall and disrupt warming of the inner core. The normalized eddy fluxes that result from such ventilation are proportional to χS [see the appendix of Tang and Emanuel (2012)], where S is the 250-850-hPa vertical wind shear, and χ is a scalar that represents the saturation entropy deficit normalized by the air-sea thermodynamic disequilibrium, as in Equation 2.8.

$$\chi = \frac{s_m^* - s_{env}}{s_s^* - s_b} \tag{2.8}$$

The pseudoadiabatic entropy, s, can be approximated following Bryan (2008):

$$s = c_p \log\left(\frac{T}{T_0}\right) - R_d \log\left(\frac{p_d}{p_0}\right) + \frac{L_v q}{T} - R_v q \log(\mathcal{H})$$

where c_p is the specific heat of dry at at constant pressure, q is the specific humidity, $\mathcal{H}$ is the relative humidity, p_d is the dry pressure, R_v is the water vapor gas constant, s_m^* is the inner core saturation entropy, s_{env} is the environmental entropy, s_s^* is the saturation entropy at the sea surface, and s_b is the entropy at the boundary layer. In order to calculate χ at a fixed pressure level p from gridded data, we first assume that temperature perturbations on pressure surfaces are small, and that the inner core is saturated (Emanuel et al., 2008), such that the numerator becomes:

$$s_p^* - s_p \approx \left[\frac{L_v q^*}{T}(1 - \mathcal{H}) + R_v q \log \mathcal{H}\right]\Big|_p$$

To evaluate these quantities, we assume that the air at the sea surface is saturated and at the same temperature and pressure as the sea surface. We also assume that $s_b = s_{LCL}^* = s_p^*$, where s_{LCL}^* is the saturation entropy at the lifted condensation level. The first step assumes adiabatic motion from the boundary layer to the lifted condensation level, which is defined as the top of the boundary layer, and the last

step follows from moist convective neutrality. Then, we have:

$$\chi_p = \frac{[L_v q^* T^{-1}(1-\mathcal{H}) + R_v q \log \mathcal{H}]\big|_p}{s_s^* - s_p^*}$$

While the environmental saturation deficit is typically evaluated at $p = 600$-hPa (Emanuel, 2013), consistent with the mid-level ventilation hypothesis, the 600-hPa level is not available through the TIGGE database. Instead, we calculate χ_p at $p = 500$-hPa and $p = 700$-hPa and take the grid-point maximum between the two levels. To obtain the χ used in FAST, we take the N-th percentile of the distribution of the saturation entropy deficit within r_{env} of the TC center. Since any downdrafts that occur near the core are detrimental to the TC, we take relatively large values of N. The saturation entropy deficit typically increases away from the core, since deep convection near the inner core saturates the mid-levels, such that if N is large enough, we are effectively diagnosing an environmental entropy deficit. To calculate the denominator, we take the median of the air-sea thermodynamic disequilibrium over the inner 200-km from the TC center. When the air-sea disequilibrium is negative, which can occur, for instance, at cold SSTs, we set $\chi = \chi_d$. We also cap χ to a value of χ_d. We estimated the optimal values of N, r_{env}, and χ_d, by finding values that minimized the mean absolute error in intensity. We found $N = 90$th percentile and $r_{env} = 1000$-km for the Atlantic basin, and $N = 50$th percentile and $r_{env} = 900$-km for the Eastern Pacific basin, and $\chi_d = 4$. The large differences in N between the two basins is largely a result of differences in climatology; the density of tropical cyclone forecasts maximizes in thermodynamically favorable environments in the Atlantic, while the opposite is true in the Eastern Pacific.

Potential intensity

The potential intensity of a TC is a theoretical upper bound on its maximum wind speed (Emanuel, 1986). Potential intensity has been verified as a reasonable upper

bound on the intensity of real TCs (Emanuel, 2000), and is defined as:

$$V_p^2 = \frac{T_s - T_o}{T_o} \frac{C_k}{C_d} (k^* - k)$$

where k is the enthalpy of the boundary layer air, and k^* is the saturation enthalpy of the sea surface. In order to calculate potential intensity, an environmental sounding with a high resolution in the vertical is required. Since potential intensity must be evaluated at the eyewall of a TC, we must remove the effect of the global ensemble system's warm core anomaly, which acts to reduce the buoyancy of a parcel lifted from the surface. Previous methods that attempt to account for this deficiency use time-lagged potential intensity fields (Emanuel et al., 2004). One weakness of this method is that it ignores any short-term variability of potential intensity. Instead, we opt to smooth out the effects of an analyzed TC. In order to remove the thermodynamic effect of an analyzed TC, we apply a 9-box smoother across a 10° by 10° grid-box centered on the TC, to the temperature, specific humidity, and sea level pressure fields, holding the boundary fixed and smoothing inwards. This first-order approximation successfully removes the potential intensity minimum near the vortex center and allows us to obtain a robust estimate of the environmental potential intensity. In this study, we calculate the spatially varying potential intensity using the analysis (initialization) fields, which have a high vertical resolution. The potential intensity field is then kept fixed throughout the forecast, though the potential intensity of the TC can still change as it moves in space.

2.3.4 Wind model

Since FAST outputs the maximum surface azimuthal wind speed, we use a parametric wind model and another parameterization to obtain the full TC wind-field as well as the maximum surface wind speed. We first obtain the axisymmetric wind profile by using the physically-based wind model developed by Chavas et al. (2015). We chose this model because of its basis on physical principles, though other wind models, such as the radii-CLIPER model (Knaff et al., 2007), could be used as well. The

wind model developed in Chavas et al. (2015) separates the axisymmetric wind field into two regions, a convecting inner region, and a subsiding outer region, and the equations are below for convenience:

$$\frac{M_{inner}}{M_m} = \frac{2(r/r_m)^2}{1+(r/r_m)^2}$$

$$\frac{\partial M_{outer}}{\partial r} = \frac{2C_d}{W_{cool}} \frac{(rV)^2}{r_0^2 - r^2}$$

where $M = rV + \frac{1}{2}fr^2$ is the angular momentum per unit mass, M_{inner}/M_{outer} is the angular momentum in the inner/outer region, r is the radius from the vortex center, V is the azimuthal wind, r_0 is the outer radius (or radius of vanishing wind), r_m is the radius of maximum winds, W_{cool} is the subsidence rate from tropospheric radiative cooling, and $M_m(r_m, V_m)$ is the angular momentum at the radius of maximum wind, where V_m is the maximum azimuthal wind speed. Because we lack observations of W_{cool}, we set $2C_d/W_{cool} = 1$ s m^{-1}, for simplicity, though the model does have some dependence on the strength of W_{cool} (Chavas and Lin, 2016). The full axisymmetric wind field can be resolved by fixing two of the three free parameters, r_m, r_0, and V_m. V_m is readily obtained from FAST, and we choose to specify r_0 (details on selecting r_0 are described in section 2.3.5). After obtaining the surface axisymmetric wind field, we apply a second model to obtain the asymmetric component of the wind field. This model is based on the isallobaric wind, which occurs whenever the vortex propagates with respect to the low-level wind, which will happen when there is vertical wind shear, **S**. In a reference frame moving with the low-level vortex, vorticity must be increasing downshear of the vortex center, and for this to happen, there must be low-level convergence. We crudely take this into account by representing the vorticity in terms of the maximum azimuthal wind **V** divided by a vortex radial length scale, and the vortex-relative vorticity advection by the shear vector times this vorticity divided by the same length scale. This yields the low-level convergence downshear of the low-level vortex. The associated convergent velocity component is then obtained by integrating over the same length scale. With some empirical adjusting of constants,

this results in:

$$\mathbf{u}_{net} = \mathbf{V} + G\mathbf{u}_t + 0.1\mathbf{S}\frac{|\mathbf{V}|}{15}$$

$$G = \min\left[1, 0.8 + 0.35\Big(1 + \tanh\Big(\frac{\phi - 35}{10}\Big)\Big)\right]$$

where $\mathbf{V}$ is the axisymmetric wind, $\mathbf{u}_t$ is the translational speed of the vortex, $\mathbf{S}$ is the 250-850-hPa vertical wind shear in m s^{-1}, ϕ is the latitude of storm center, $|\mathbf{V}|$ is the magnitude of the axisymmetric wind in kts, and $\mathbf{u}_{net}$ is the net wind at the surface. Finally, the maximum surface wind speed is determined by taking the maximum magnitude of $\mathbf{u}_{net}$ over the domain.

2.3.5 Initialization and parameter estimation

The final component of FAST pertains to initialization. A poor initialization can lead to significant errors in the short-range forecast period (Emanuel and Zhang, 2016, 2017). Since we want to include initial intensity uncertainty in the probabilistic system, we create a synthetic perturbation of the TC intensity analysis over the past 24 hours of the analyzed TC (see Appendix for details). Uncertainties in the intensity observations are taken from climatological errors (Landsea and Franklin, 2013). For each synthetic ensemble member, we use the environmental parameters from the analysis fields to drive FAST, and add a time-varying forcing term to the azimuthal wind (Equation 2.1) such that the modeled maximum surface wind best matches the synthetic perturbation of the observed TC intensity. The initialization period runs from 48 hours before the initial forecast time until the initial forecast time, where the forcing term to the azimuthal wind equation then decays in magnitude as $\exp^{-(t/t_0)^2}$, where t is the forecast lead time and $t_0 = 1$ day.

To initialize the wind field, we take the initial analysis of the maximum extent of the 34-, 50-, and 64- kt winds in each quadrant (obtained from the CARQ lines of the ATCF a-decks), and find the corresponding value of r_0 that allows the modeled asymmetric wind field to best match the analysis. Furthermore, to combat large negative biases in the axisymmetric wind model at radii where $3 \lessapprox r/r_m \lessapprox 6$ (see

Fig. 9 in Chavas et al., 2015), we add a shape parameter k to the axisymmetric wind profile, i.e. for $r > r_m$, $V(r,k) = V(r)^k$. Then, to initialize the wind-field, we find r_0 and k such that the full asymmetric wind field best matches the analysis radii in each quadrant. Finally, if an official forecast of the radii in each quadrant is available, the optimal r_0 and k, given the official forecast of intensity, are used to interpolate r_0 and k forward in the forecast. Otherwise, r_0 and k are kept constant in the forecast. If an initial analysis and forecast of the wind radii do not exist, we set $r_0 = 700$-km and $k = 1$. This may not be realistic, but could be improved upon by using the model developed in Knaff et al. (2017), which predicts the maximum extent of the 34-, 50-, and 64-kt winds. We do not explicitly perturb r_0, though this could be the subject of future work.

2.4 Evaluation of the large-ensemble model

In order to robustly evaluate the skill of FHLO, we run 1000-member ensemble reforecasts for all 00 UTC and 12 UTC cycle TC forecast cases in the Atlantic and Eastern Pacific basins during the years 2015-2018 (the choice of 1000 members is described in the following section). Since all of the aforementioned data used to generate a probabilistic forecast are available in real-time, these reforecasts can be considered equivalent to late-cycle real-time forecasts. Since the skill of FHLO also depends on the skill of the ensemble, we run two variations of 1000-member ensembles, one using data from the ECMWF ensemble (hereafter FHLO-ECMWF) and the other from the GEFS (hereafter FHLO-GEFS). We also combine the two into a 2000-member super-ensemble, which we will denote FHLO-Super. We evaluate the performance of FHLO by using the HURDAT2 best-track data as the observed track, intensity, and wind-radii of each TC (Landsea and Franklin, 2013). For each forecast case, we predict the track distribution, intensity distribution, and probability of exceedance for the 34-, 50-, and 64-kt wind speed thresholds.

2.4.1 Ensemble size

The choice of running 1000-member ensembles is motivated primarily by looking at probability distributions of wind speeds from TCs at a fixed point. To illustrate this, we generate point-wise forecasts of wind speed from Hurricane Maria at San Juan, Puerto Rico, using the ECMWF ensemble initialized on Sept. 18, 2017 00 UTC as input into FHLO. For demonstration, we use 100- and 1000-member FHLO-ECMWF ensembles, as well as a 51-member FHLO-ECMWF model that only uses the tracks from the original ECMWF ensemble (henceforth, RAW-ECMWF). Figure 2-3 shows the time-varying maximum wind speed from Hurricane Maria at San Juan, Puerto Rico, from the 1000-member FHLO-ECMWF and the 51-member RAW-ECMWF. From the eye-test, there is a sampling issue with RAW-ECMWF; there simply are not enough ensemble members to resolve the tail of the distribution. To be more quantitative, we estimate the non-dimensional damage ([0, 1]), f, that represents the fraction of property lost [see Equation 1 of Emanuel (2011)]:

$$f = \frac{v_n^3}{1 + v_n.^3}$$
$$v_n \equiv \frac{\mathrm{MAX}(V - V_{\mathrm{thresh}}, 0)}{V_{\mathrm{half}} - V_{\mathrm{thresh}}}$$

where V is the maximum wind speed, V_{thresh} is the wind speed at which no damage occurs, and V_{half} is the wind speed at which half damage occurs. As the right column of Figure 2-3 shows, there is an inferred probability of zero for $f > 0.3$ from the 51-member RAW-ECMWF. However, as we increase the size of the ensemble, the right tail of the distribution, which represents the most destructive scenarios, is better resolved. Thus, large-ensemble forecasts are necessary to flesh out the tail of wind distributions, which is often critical to decision making. With only a small number of ensemble members, it is extremely difficult to create smooth PDFs of point-wise wind forecasts. We settled on a 1000-member ensemble, since the marginal return on resolving the tail diminishes with further increases in ensemble size.

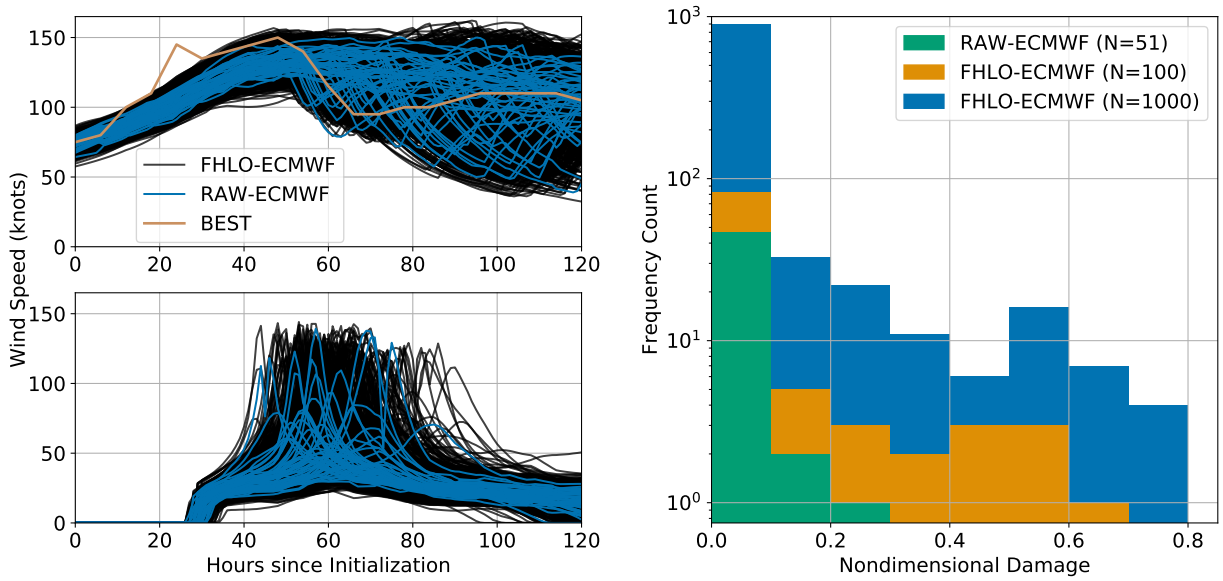

Figure 2-3: Forecasts, initialized at 00 UTC on 18 September 2017, of the time-varying maximum wind speed from Hurricane Maria, (top-left) across the entire storm and (bottom-left) at San Juan, Puerto Rico. Forecasts use the original 1000-member FHLO-ECMWF model and a 51-member FHLO-ECMWF model (RAW-ECMWF) that uses only the original ECMWF ensemble tracks. BEST indicates the best-track intensity of Hurricane Maria. (Right) Distribution of nondimensional damage, f, following Emanuel (2011), for wind speeds observed at San Juan at $t = 60$ hours from initialization, for the RAW-ECMWF model (51 tracks), as well as the 100-member and 1000-member FHLO-ECMWF ensembles.

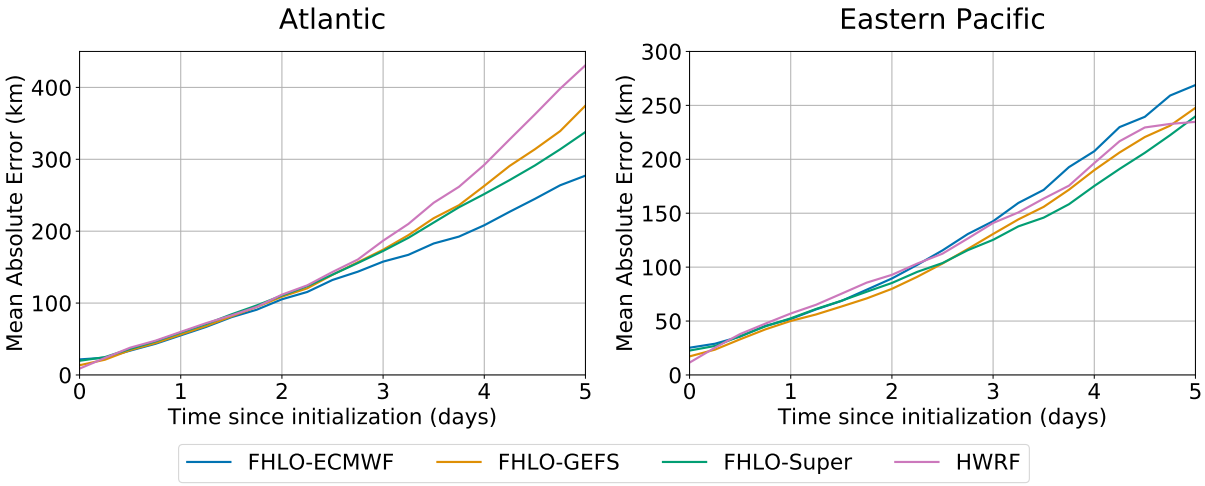

Figure 2-4: Mean absolute error (km) in track as a function of the time since initialization, for the mean of 1000 synthetic tracks for the FHLO-ECMWF, FHLO-GEFS, and FHLO-Super ensembles, as well as the HWRF model. Sample set includes forecasts from 2015-2018 in the (left) Atlantic basin and (right) Eastern Pacific basin.

2.4.2 Track forecasts

In order to verify that the synthetic track algorithm produces tracks that are statistically similar to the set of TC tracks of a given EPS, we evaluate the track error distribution and spread from forecasts of (1) the mean of the synthetic tracks, and (2) the mean of the ensemble system. A two-sample Kolmogorov-Smirnov test indicates that the track error distributions of forecasts from both methods are statistically similar at all lead times, regardless of the ensemble, with $\alpha = 0.05$ (not shown).

Figure 2-4 shows the error between the observed track and the mean of the 1000-member ensemble, which is driven by the tracks of different EPSs. FHLO-GEFS has the smallest initial error for both basins, since the GEFS ensemble relocates the analyzed vortex to the best-guess position at initialization (Liu et al., 2000). In the Atlantic basin, FHLO-ECMWF outperforms all of the other individual models for all other lead times, while FHLO-GEFS has the best performance in the Eastern Pacific. The multi-model super-ensemble, has the lowest mean absolute error (MAE) for almost all lead times in both basins, which is a well-known property of super-ensembles (Williford et al., 2003; Vijaya Kumar et al., 2003). Of course, the best metrics for the evaluation of a large-ensemble are probabilistic metrics. A reliability

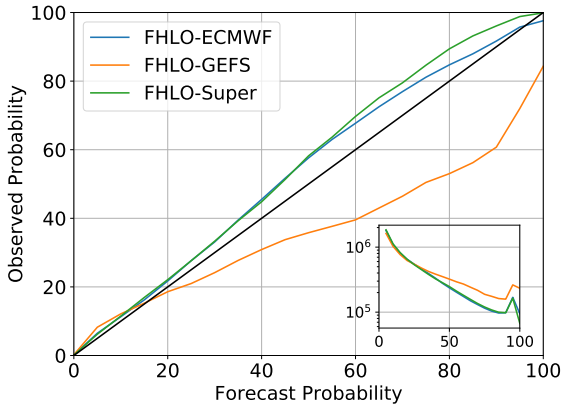

Figure 2-5: The reliability curve for 75-km strike probability, cumulative over 5 days, using the FHLO-ECMWF, FHLO-GEFS, and FHLO-Super ensembles. Solid black line indicates perfect reliability. Sample set includes forecasts from 2015-2018 in the Atlantic and Eastern Pacific basins, and sample size for each model, as a function of forecast probability, is shown in the inset.

diagram assesses the observed probabilities as a function of the forecasted probabilities. A model is said to be reliable if the observed frequencies of an event match the observed frequencies of its forecast probability – that is, the model performs well all the time without its forecasts being overconfident or underconfident. A perfectly reliable model falls along the 1:1 line in a reliability diagram. Figure 2-5 shows the reliability curve for the probability that the center of the TC is within 75-km of a particular grid-point (using a 0.1° resolution grid), cumulative over 5 days. In general, the results demonstrate the reliability of the FHLO-ECMWF strike probabilities, as well as the over-confidence of the FHLO-GEFS strike probabilities. These results are similar to those obtained in Titley et al. (2020). We forgo a detailed evaluation of the synthetic tracks in lieu of evaluating the wind speed exceedance probabilities in section 2.4.4, as the latter cannot be accurate if the former is not.

2.4.3 Intensity forecasts

In this section we evaluate the intensity forecasts of FHLO using traditional, deterministic statistics, as well as probabilistic metrics. When evaluating, we do not explicitly terminate a TC when its simulated intensity falls below the tropical depression

threshold (17 m s^{-1}). Figure 2-6 shows a model comparison of the mean-absolute error in intensity as a function of time since initialization, for forecasts where the initial intensity is greater than 30 m s^{-1} (the reason for applying this filter is described below). Since the mean-absolute error is a deterministic statistic, we take the mean of all the members of each FHLO-ensemble as its deterministic model forecast. In both basins, the intensity error is largely the same between FHLO-ECMWF, FHLO-GEFS, and FHLO-Super for the first two days, likely since the large-scale environments of the ECMWF ensemble and GEFS do not diverge significantly for these short-term timescales. The intensity errors begin to diverge around two days, after which we observe that FHLO-ECMWF and FHLO-Super outperform FHLO-GEFS. The FHLO-based intensity forecasts also have a larger absolute error than the Hurricane Weather Research and Forecasting (HWRF) model, though the FHLO-based ensembles perform comparably to HWRF in the Eastern Pacific. The FHLO-based ensembles have a slight negative bias in the first two days of initialization. In general, however, the bias over the sample set is comparable to that of HWRF.

We also construct an idealized lower bound on the intensity error of the FHLO-based ensembles, to understand the best-case performance of a simple intensity model such as FAST. To gain insight into this, we take the exact same forecast cases, but instead use near-perfect initial conditions and analysis fields to derive the environmental parameters. The near-perfect initial conditions are achieved by running the aforementioned initialization procedure using the best-track of the TC, forcing the model to the observed intensity. Once the initialization procedure hits the initialization time, the model is allowed to evolve freely. Then, the lower-bound error is computed by the divergence of the FAST model from the best track intensity. This is shown as the dashed-black curve in Figure 2-6. In the Eastern Pacific basin, the lower-bound curve suggests that with improved ensemble forecasts and model initialization, the intensity error of the FAST model will also decrease. This is somewhat less true in the Atlantic basin; the lower-bound curve suggests that better initialization could result in improvements in forecasts with lead times of up to 2 days. For lead times longer than 2 days, however, the lower-bound curve is nearly indistinguishable from

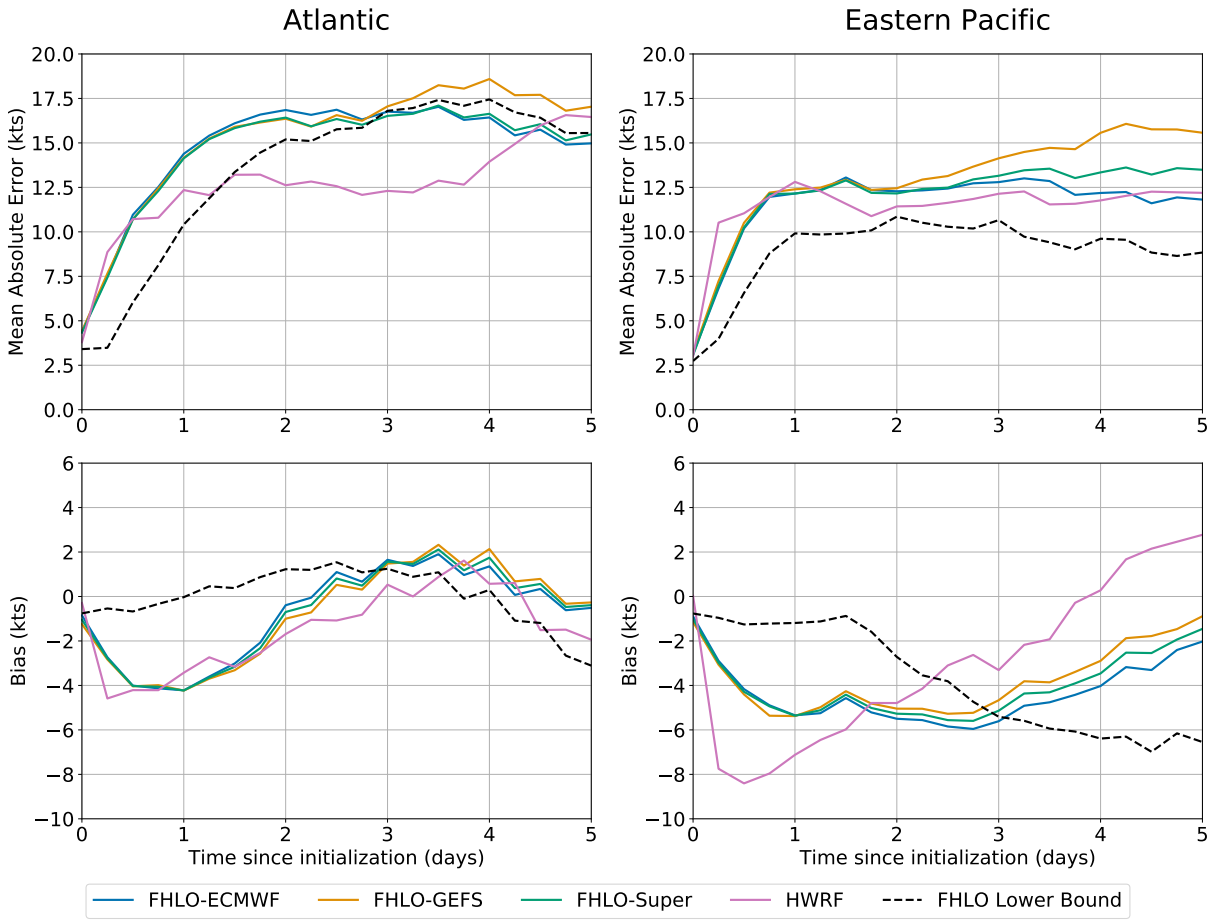

Figure 2-6: The (top) mean absolute error and (bottom) bias of the FHLO-ECMWF, FHLO-GEFS, and FHLO-Super ensemble forecasts. Only forecasts where the initial intensity is greater than 30 m s^{-1} are included in the samples. The dashed-black line represents a lower bound on the intensity error, achieved by using near-perfect initialization and a perfect track. Sample set includes forecasts from 2015-2018 in the (left column) Atlantic basin and (right column) Eastern Pacific basin.

the forecast errors. This may be due to low inherent predictability and/or model error stemming from sub-optimal parameterization of the ventilation, though further investigation is outside the scope of this study. Note that these bounds are derived using the current framework of the model; improvements to the model itself could lower the bound further. Lastly, in some sense, this curve can be loosely compared to the model-error of FAST. While simple models, such as FAST, are unable to physically resolve the atmosphere and are often less accurate than more complex models, they are computationally inexpensive and can be used in large-ensemble studies such as this one. We believe that FAST makes a relatively good trade-off between simplicity and accuracy, though it is unlikely to be the best we can do.

Next, we evaluate the FHLO-based intensity forecasts using probabilistic metrics. A convenient metric to compare deterministic and probabilistic forecasts is the continuous ranked probability score (CRPS), which is the integrated squared difference between the cumulative distribution function (CDF) of the forecast and the observation:

$$CRPS(F, v_{obs}) = \int_{-\infty}^{\infty} (F(v) - 1(v - v_{obs}))^2 \, dv$$

where $F(v)$ is the CDF of the forecast, v_{obs} is the observed intensity, and 1 is the Heaviside step function. For a deterministic forecast, the CRPS simplifies to the mean absolute error. Figure 2-7 shows the CRPS as a function of time since initialization, and we see similar patterns in the results as compared to those of the mean absolute error. In the Atlantic basin, the CRPS of the FHLO-based ensembles is close to that of the deterministic HWRF forecast, for forecast lead-times shorter than four days. For lead-times longer than four days, the CRPS of the FHLO-based ensembles is lower than that of HWRF. In the Eastern Pacific, the CRPS of the FHLO-based ensembles is lower than that of HWRF. This suggests that characterizing both the mean-state and spread of the large-scale flow is paramount to quantifying the uncertainty in the future intensity of a TC.

Finally, it is worth commenting on the filter we used above, where we only considered forecasts where the initial intensity is greater than 30 m s^{-1}. The filter was

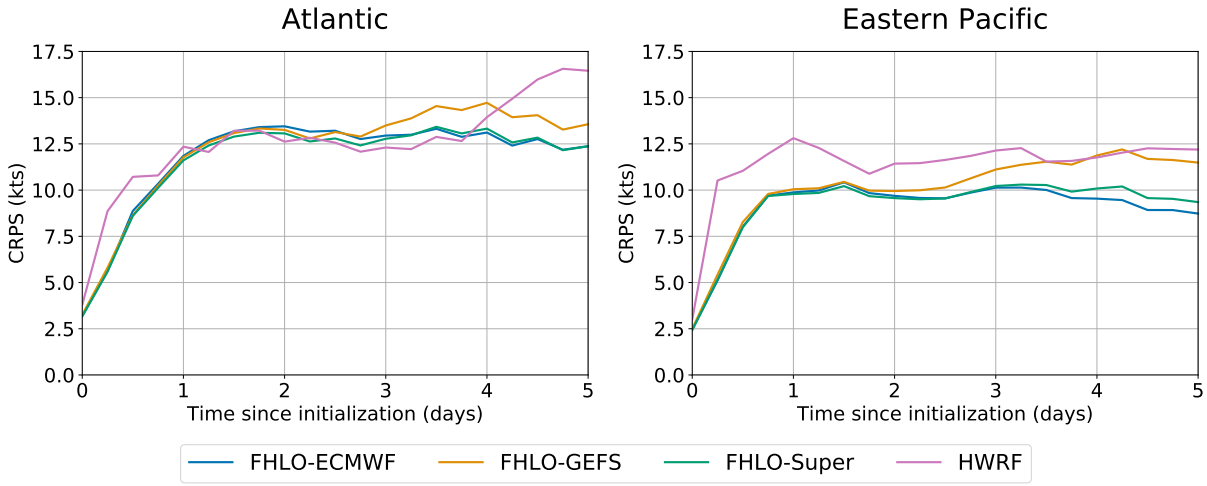

Figure 2-7: The continuous ranked probability score of the FHLO-ECMWF, FHLO-GEFS, and FHLO-Super ensemble forecasts. Only forecasts where the initial intensity is greater than 30 m s^{-1} are included in the samples. Sample set includes forecasts from 2015-2018 in the (left column) Atlantic basin and (right column) Eastern Pacific basin.

specified in order to bypass the issue of cyclogenesis. In general, the mean-absolute error in intensity increases as the initial intensity threshold in the evaluation filter is decreased (not shown), for a variety of reasons. While this may point to deficiencies in applying models based on idealized, axisymmetric TC theory to weak disturbances, there may be additional reasons for this behavior. For instance, a model that does not properly capture the observed intensification rate distribution but is tuned to provide sluggish intensification for weak storms could have the smallest mean absolute error in intensity, since most weak storms do not intensify into strong TCs. While the FAST system does capture the observed intensification rate distribution (Emanuel, 2017), it has the tendency to over-intensify weak disturbances, so long as the mid-level ventilation is not large. Regardless, much work has suggested that the intrinsic predictability of cyclogenesis and subsequent intensification is low (Sippel and Zhang, 2008; Zhang and Sippel, 2009; Zhang and Tao, 2013), and thus TC genesis remains a significant forecasting challenge (Rappaport et al., 2009).

2.4.4 Probabilistic wind speeds

In this section, we evaluate the 34-, 50-, and 64-kt wind speed exceedance probabilities that are generated from the FHLO-based ensembles. For each ensemble member, and at each time step, the full wind-field of the TC is estimated. The evaluation procedure is similar to that in DeMaria et al. (2009), where the probabilities are generated by summing the number of ensemble members where the winds exceed a particular threshold, for each individual grid point. Following the evaluation procedure of DeMaria et al. (2009), we do not include forecast cases of extra-tropical transition. To do this, we truncate any forecasts that extend beyond when the official forecast predicts a transition to an extra-tropical storm. The wind probabilities should also account for the timing of dissipation, and thus we do not modify the forecast if the analyzed storm in the best-track terminates before the end of the forecast, and vice-versa. The latter situation is often more problematic for this model. This is because the ensemble tracks depend on how well the ensemble models resolve the TC on their relatively coarse grids. Finally, in this section, we only evaluate forecasts where the initial TC position is equatorward of 30°. This is a crude way to filter for storms that are characteristically more tropical, which is when we expect the FHLO-based ensembles to work the best. The aforementioned wind model also has more difficulty representing highly-asymmetric wind fields, which is more likely to be the case for storms that are influenced by baroclinicity. Nevertheless, a large fraction (70% in Atlantic, 99% in the Eastern Pacific) of the initial positions of our samples occurred south of 30°. Extending the model verification to latitudes north of 30° is left to future work.

Figure 2-8 shows an example of the exceedance probabilities for the 64-kt wind speed threshold, cumulative over the 5-day forecast period, for Hurricane Irma. The analyzed maximum extent of 64-kt winds, indicated by the thick black contours, are reasonably within the bounds of the probabilistic forecast, except for a mild along-track error. To obtain robust evaluation statistics, we evaluate all the forecasts by analyzing the associated reliability diagrams, multiplicative bias curves, and the maximum threat scores (Wilks, 2011).

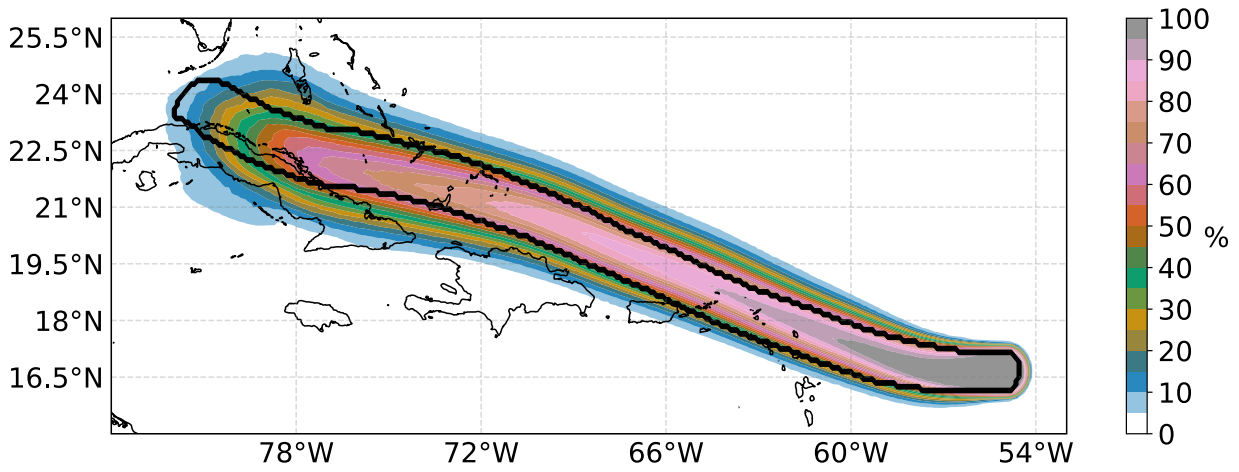

Figure 2-8: Probability of wind exceeding 64-kts over a 5-day period, for Hurricane Irma in the Atlantic Basin, using 1000 ensemble members bootstrapped from the ECMWF ensemble. Forecast initialized at 00 UTC on September 5th, 2017. Black contour depicts extent of the observed 64-kt winds.

Figure 2-9 displays a reliability diagram for the cumulative exceedance wind probabilities using different wind speed thresholds, separated by basin and cumulative time. The results indicate that in general, the exceedance probabilities generated by the FHLO-Super model are reliable at the examined cumulative times and in both basins. We also observe that for probabilities between 0% and 50%, the 34-kt winds are more overdispersive than those for the 50-kt winds, which in turn are more overdispersive than the 64-kt winds. This is likely due to two factors. First, negative biases at $r/r_m \approx 4$ in the axisymmetric wind model cannot be completely eliminated with the shape parameter, though the bias was heavily reduced (not shown). Second, while the TC wind profile is typically dominated by axisymmetric processes near the core, asymmetries often dominate further away from the core. These asymmetries cannot always be represented by the simple asymmetric model in the aforementioned text. The combined effect of both of these factors is likely to underestimate the radial extent of winds at a particular threshold in each quadrant, where the magnitude of this bias decreases as one moves towards the inner core (i.e. we underestimate r_{34}, and less so for r_{50}, and even less for r_{64}). This observed bias could be addressed by adding more degrees of freedom to the wind model, though this would reduce the simplicity.

Using another wind model with more degrees of freedom, such as the radii-CLIPER wind model of Knaff et al. (2007), may also help to alleviate these issues.

The multiplicative bias is defined by $B = \sum_i F_i / \sum_i O_i$, where B is the multiplicative bias, F_i are the forecasted probabilities, and O_i is the observation (0 or 1). B is a measure of whether the average forecast has probabilities that are too large ($B > 1$), or too small ($B < 1$). The average probabilities of FHLO-Super, shown by Figure 2-10, are generally too small for the 34-kt and 50-kt thresholds, and reasonably unbiased for the 64-kt threshold. The underlying reason for $B < 1$ at the 34- and 50-kt thresholds is likely the same reason for the bias in the reliability diagrams; namely, that r_{34} and r_{50} are being underestimated in each quadrant. Regardless, the multiplicative biases at a fixed threshold remain relatively constant in time. This suggests that reducing the bias in the wind model could lead to $B \approx 1$ at all thresholds.

Unfortunately, a large number of grid points across a basin have zero probability and will evaluate to correct nulls, which can strongly influence the bias scores. To remedy this, we use the threat score metric to further evaluate the probabilistic wind forecasts. Correct nulls are not used in the threat score. To calculate the threat score, one defines a threshold probability to determine a categorical forecast (yes or no), and divides the total number of correct forecasts by the sum of the total number of correct forecasts, false positives, and misses. The threat score has a score from 0 (worst) to 1 (best). As a baseline, we perform a homogeneous comparison with NHC's MCP model. NHC only archives the probabilities accumulated over all storms during a particular cycle, which is an issue when combined with the fact that FHLO forecasts only run as far out as the ensemble tracks. Thus, for any forecast, we must discard any samples beyond the lead time at which the FHLO forecast for any existing TC dissipates. This reduces the amount of samples we can use to evaluate FHLO. In the Atlantic (Eastern Pacific), we used 348 (161) cycles at a lead time of 6 hours, to 61 (20) cycles at a lead time of 120 hours, using 00 UTC and 12 UTC forecasts from 2015-2018. We also create a super-ensemble between FHLO-Super and the MCP model, simply by averaging the wind probabilities of each model, and denote this as FHLO-MCP.

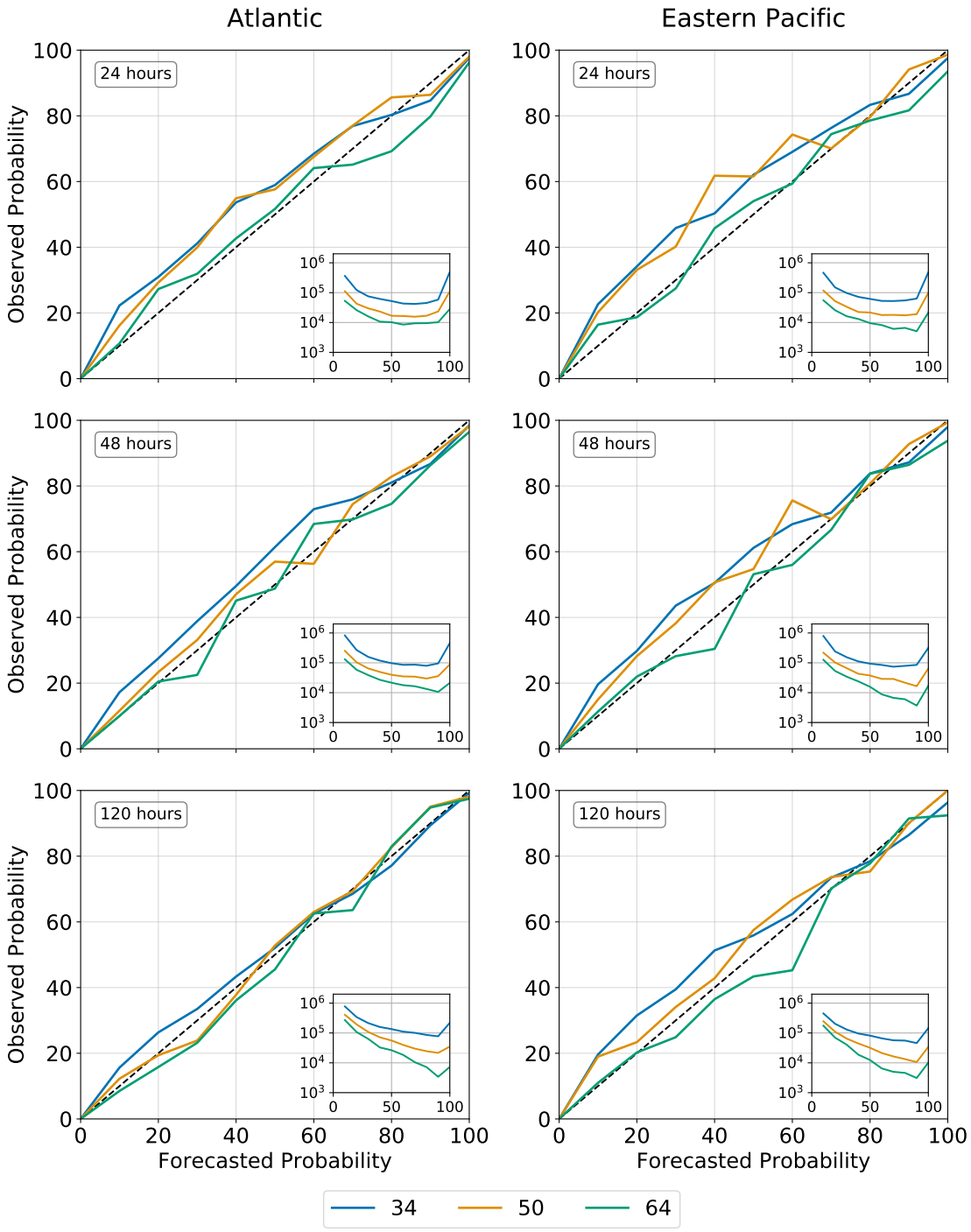

Figure 2-9: Reliability diagram for exceedance wind probabilities, cumulative over (top) 24, (middle) 48, and (bottom) 120 hours, for the 34-, 50-, and 64-kt thresholds, using the probabilities derived from FHLO-Super. Basins are separated into (left column) Atlantic and (right column) Eastern Pacific. Sample set includes only forecasts where the initial position is south of 30°N. Dashed black line indicates perfect reliability. Insets show the sample size, for each threshold, as a function of forecast probability (days).

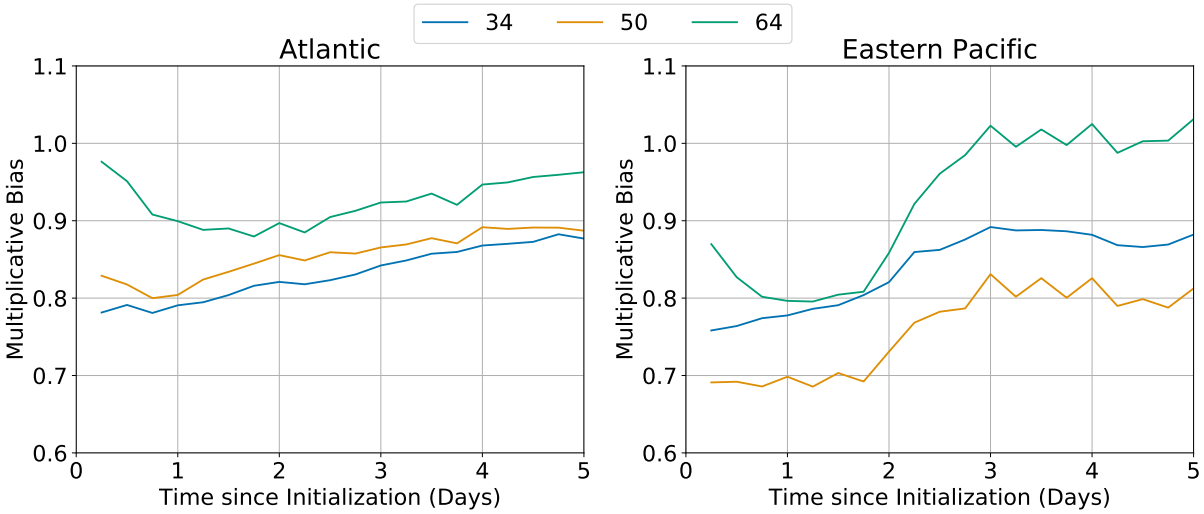

Figure 2-10: Multiplicative bias for the FHLO-Super cumulative exceedance wind probabilities, separated into the 34-, 50-, and 64-kt thresholds, and as a function of the time since initialization. Basins are separated into (left) Atlantic and (right) Eastern Pacific. Sample set includes only forecasts where the initial position is south of 30°N.

Figure 2-11 compares the maximum threat scores of FHLO-Super, the MCP model, and FHLO-MCP. The threat scores generally maximize at a threshold probability of $\approx$ 30% (not shown). In the Atlantic basin, the MCP model is superior at shorter lead times ($\approx$ 0-2 days), especially at the 34- and 50-kt thresholds. One reason this may be is that analyses of the initial position and intensity can be explicitly taken into account in the official forecast. On the other hand, FHLO-Super has higher threat scores at longer lead times ($\approx$ 3 days), regardless of the threshold. In the Eastern Pacific basin, FHLO-Super has larger threat scores at nearly all lead times and thresholds. These results suggest that incorporating state-dependent uncertainties could lead to improvements in long-range, probabilistic, point-wise wind probability forecasts. Taking into account the flow-dependent uncertainty will be extremely important if forecast lead times are extended beyond 5 days. Finally, in the Atlantic basin, the FHLO-MCP super-ensemble has better threat scores compared to both FHLO-Super and the MCP model, at all lead times and thresholds. While the sample size of the homogeneous comparison between FHLO-Super and the MCP model may be a bit limited, this provides more evidence that combining multiple

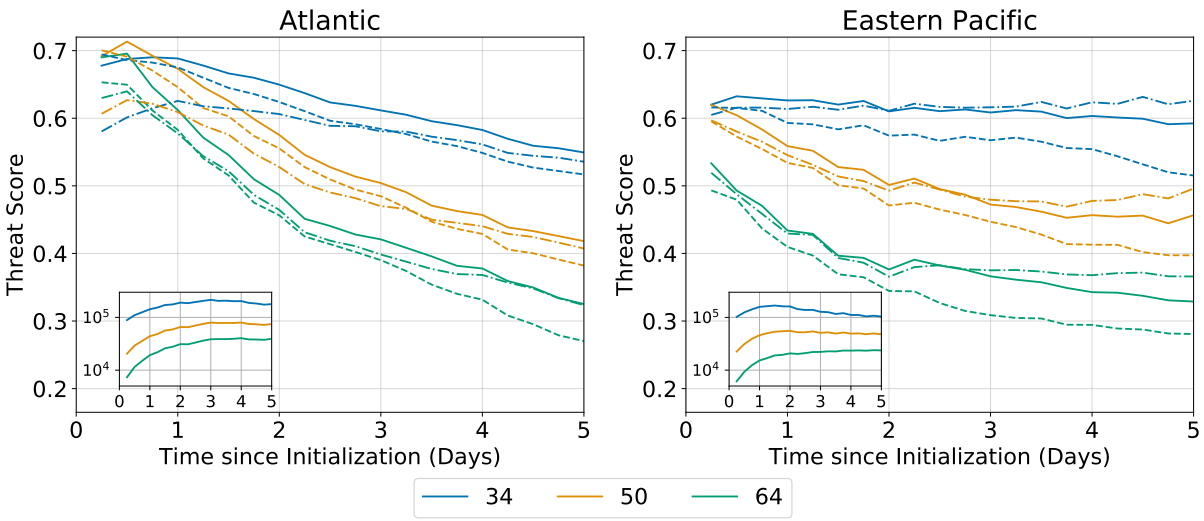

Figure 2-11: The maximum threat scores for the (dot-dashed) FHLO-Super, (dashed) MCP, and (solid) FHLO-MCP cumulative exceedance wind probabilities, separated into the 34-, 50-, and 64-kt thresholds, and as a function of the time since initialization. Basins are separated into (left) Atlantic and (right) Eastern Pacific. Sample set includes only forecasts where the initial position is south of 30°N. Insets show the threat score denominator (hits + misses + false alarms) for each threshold, as a function of time since initialization (days), for samples used to evaluate FHLO-MCP.

models can lead to superior forecasts.

As mentioned previously, ensemble models have the tendency to possess negative biases in the intensity of a TC. This may lead to premature dissipation of a TC, resulting in smaller threat scores from forecast misses. We expect that as the ability to resolve TCs in ensemble models increases, the threat scores associated with the FHLO-based ensembles will also increase. Regardless, these results suggest that there is much value in incorporating state-dependent uncertainty in TC forecasts.

2.5 Conclusions

In this study, we developed FHLO, a probabilistic, large-ensemble [O(1000) members], TC prediction framework that estimates forecast uncertainty by leveraging the internal variability of the large-scale environment simulated by a global NWP ensemble. We described a method to generate synthetic tracks that are statistically similar to those of an ensemble NWP model. We evaluated the intensity forecasts of the

simulated TC along each track using the FAST intensity model, and we then used a physically-based wind model to estimate the full wind field. We evaluated the model using four years (2015-2018) of reforecasts in the Atlantic and Eastern Pacific basins.

We show that the FHLO-based large-ensemble intensity forecasts perform comparably with HWRF, an advanced NWP model. We also evaluate the probability of exceedance for the 34-, 50-, and 64-kt wind speed thresholds using reliability curves, multiplicative bias curves, and threat scores. The results suggest that, notwithstanding some slight biases at low wind-speed thresholds, the FHLO-based wind forecasts are skillful and reliable. Point-wise wind forecasts using the FHLO framework are particularly skillful at lead times longer than 3 days, and a combination of FHLO-Super and NHC's MCP model was shown to have the highest threat scores across all lead times in the Atlantic. These results suggest that it will be important to better characterize the state-dependent uncertainty to continue to improve our long-range forecast skill.

Probabilistic wind speed forecasts combine the uncertainty in both the track and intensity, and provide uncertainty quantification of wind speeds at fixed points. As compared to traditional forecast quantities such as the exact storm center or the maximum wind speed anywhere in the storm, point-wise wind speeds are the more relevant TC hazard metric for assessing wind impacts. The uncertainty of wind-speeds at a point could also be translated to location-specific vulnerabilities, as is the goal of the Hurricane Risk Calculator (Vigh et al., 2020). Thus, while the traditional track-intensity dichotomy is useful for evaluating and improving our models, it is not the most useful and pertinent metric to the public.

It is also important to stress that large-ensembles (O(1000) ensemble members) are necessary to provide accurate forecasts of point-wise wind speed probability distributions. This is one of the key advantages of the large-ensemble framework. Furthermore, unlike the model described in DeMaria et al. (2009), the FHLO framework quantifies forecast uncertainty by incorporating the internal variability in the large-scale environment. This is achieved by including uncertainty in the TC's track, uncertainty in the dynamic and thermodynamic environments, and uncertainty in

the initial conditions. The synthetic tracks of the model are generated by sampling from the dispersion among TC tracks of an ensemble NWP model. The dynamic and thermodynamic fields of the ensemble NWP system are also used to generate realistic perturbations to TC-relevant environmental quantities, such as the saturation entropy deficit and vertical wind shear. Initial condition uncertainty is accounted for by incorporating stochastic perturbations to the initial intensity and inner-core moisture.

There is also uncertainty in the observations that are used to evaluate the model. While we evaluate the wind speed probabilities by assuming that all points within the estimated maximum radial extent of a particular wind speed threshold, this may likely not be the case. A better method to evaluate wind speed probabilities is to only use wind observations over land, which are arguably more objective than best-track estimates of intensity. Undertaking such an evaluation could be an area of future work.

It is worth discussing the various sources of error and limitations of the FHLO framework. First, while we provide evidence that FAST can reasonably model and forecast TCs, the FAST equations are still an imperfect and idealized representation of the evolution of the intensity of a TC. We expect the intensity module to work best for axisymmetric, surface-flux driven, mature TCs, and thus less so for tropical disturbances or cyclones that are undergoing extra-tropical transition. A statistical bias correction could be applied to the intensity component for weak disturbances in light of this issue. Furthermore, in the FAST framework, we consider mid-level ventilation as the only process that dries out the inner core of a TC. The eddy-entropy flux into the eyewall is then approximated to vary linearly with the product of the environmental saturation entropy deficit and the vertical wind shear (Tang and Emanuel, 2012). Any departures from this approximation will affect the intensity model. Uncertainty and error can also arise from the methods developed to calculate environmental quantities. The definition of vertical wind shear that is relevant to the TC is problematic, since errors can be introduced through r^*, as well as the vertical levels by which to calculate shear. In this study, we fixed $r^* = 400$ km and used

the 250-850-hPa vertical wind shear. These are perhaps not the best approximations, and it may be the case that the "optimal" r^* and vertical levels by which to calculate vertical wind shear can vary from storm to storm.

Since TCs are primarily driven by thermodynamic disequilibrium between the sea-surface and boundary layer air (Emanuel, 1986), accurate observations of the ocean are important to properly calculate environmental quantities, such as the potential intensity. For this study, errors in the estimation of these quantities could have been introduced with the smoothing operators, which were necessary to remove the TC's influence on the thermodynamic and dynamic fields. Furthermore, we parameterize ocean mixing from upwelling by using climatological mixed layer depth and sub-mixed layer thermal stratification, which effectively smooths out any high-frequency variability in the ocean. This could lead to large errors in intensity forecasts (Emanuel et al., 2004). Future work will incorporate information from a real-time ocean model.

FHLO can also be used to forecast the probability of rapid intensification (RI). While a full evaluation of the skillfulness of the FHLO-based ensemble forecasts to predict RI is left for future work, preliminary evaluation of probabilistic rapid intensification forecasts, regardless of the intensity of the storm, shows some promise (not shown). The evaluation results of the track and intensity forecasts also suggest that combining many more ensemble models, such as the UK Met Office and Japan Meteorological Agency ensemble systems, could lead to more skillful forecasts, as suggested by Yamaguchi et al. (2012) and Titley et al. (2020). In addition, while we only used one model to predict TC intensity in this study, using a variety of intensity models to generate intensity forecasts may improve the overall model. The only restriction is that the intensity model must be computationally inexpensive. This principle applies equally to the wind field model.

Finally, it is important to note that the skill of the FHLO-based ensemble is derived from the accuracy of the ensemble NWP system. While it is clear that errors in representing the environmental fields will significantly affect the intensity component, errors in representing the TC in the NWP model itself can also affect the FHLO-based ensemble. This can happen when a TC dissipates too early in the

ensemble prediction model, such that the track model will generate tracks that also dissipate too early. Though the skill of FHLO is significantly coupled to the quality of the ensemble system, it is likely that the skill of FHLO will progress along with advancements in ensemble NWP models. This is arguably the most intriguing aspect of FHLO: it can be viewed as a framework for bootstrapping an ensemble NWP model.

Chapter 3

On the Effect of Surface Friction and Upward Radiation of Energy on Equatorial Waves

Abstract

In theoretical models of tropical dynamics, the effects of both surface friction and upward wave radiation through interaction with the stratosphere are oft-ignored, as they greatly complicate mathematical analysis. In this study, we relax the rigid-lid assumption and impose surface drag, which allows the barotropic mode to be excited in equatorial waves. In particular, a previously developed set of linear, strict quasi-equilibrium tropospheric equations is coupled with a dry, passive stratosphere, and surface drag is added to the troposphere momentum equations. Theoretical and numerical model analysis is performed on the model in the limits of an inviscid surface coupled to a stratosphere, as well as a frictional surface under a rigid-lid. This study confirms and extends previous research that shows the presence of a stratosphere strongly shifts the growth rates of fast propagating equatorial waves to larger scales, reddening the equatorial power spectrum. The growth rates of modes that are slowly propagating and highly interactive with cloud-radiation are shown to be negligibly affected by the presence of a stratosphere. Surface friction in this model framework acts as purely a damping mechanism and couples the baroclinic mode to the barotropic mode, increasing the poleward extent of the equatorial waves. Numerical solutions of the coupled troposphere-stratosphere model with surface friction show that the stratosphere stratification controls the extent of tropospheric trapping of the barotropic mode, and thus the poleward extent of the wave. The superposition of phase-shifted barotropic and first baroclinic modes is also shown to lead to an eastward vertical tilt in the dynamical fields of Kelvin-wave like modes.

3.1 Introduction

Reduced models of the tropical atmosphere have found much success in replicating many characteristics of the tropical circulation. Of prominence are theoretical models that reduce the linear, primitive equations to the shallow water equations by use of only the first baroclinic mode (Matsuno, 1966; Gill, 1980). Indeed, remarkable evidence of the linear and neutral equatorial waves that arise from the Matsuno-Gill model have been documented in the tropics (Wheeler and Kiladis, 1999). The first baroclinic mode has also been used extensively in simple models of the tropics, from studies of intraseasonal oscillations (Emanuel, 1987; Sobel et al., 2001) to steady circulations (Neelin and Held, 1987; Emanuel et al., 1994; Neelin and Zeng, 2000; Sobel and Bretherton, 2000), among many others.

While the first baroclinic mode is certainly a prominent feature of the tropical atmosphere (Xu and Emanuel, 1989), observational data and analysis have suggested the existence of another vertical mode, the second (stratiform) baroclinic mode (Mapes and Houze, 1995; Straub and Kiladis, 2002). These observations have lead to a plethora of theoretical studies that analyze how the interaction between the first and second baroclinic modes can lead to instability in equatorial waves (Mapes, 2000; Kuang, 2008b).

Perhaps curiously left behind is the barotropic mode, even though it does indeed survive the strict quasi-equilibrium assumption; in fact strict quasi-equilibrium eliminates all but the barotropic and first baroclinic modes (Emanuel, 1987; Neelin and Zeng, 2000). The barotropic mode can be excited in linear models of equatorial waves through coupling to the first baroclinic mode via surface friction (Wang, 1988; Wang and Rui, 1990; Moskowitz and Bretherton, 2000) or removal of the rigid-lid assumption (Yano and Emanuel, 1991). Note that non-linearity can lead to excitement of the barotropic mode, even under a rigid-lid and no surface friction (Neelin and Zeng, 2000). In this study, we build on the linear, strict quasi-equilibrium model first formulated in Khairoutdinov and Emanuel (2018) (henceforth, KE18) and further analyzed in Emanuel (2020) (henceforth, E20), and investigate how excitation of

the barotropic mode through both surface friction and coupling to the stratosphere affects the growth, structure, and propagation of equatorial waves.

Baked into the modal decomposition of many simple models of the tropics is the rigid lid assumption, since it dramatically simplifies analytic solutions. However, in reality the tropopause does not act as a rigid lid on the troposphere. While it is true the stratosphere has a larger stratification than the troposphere, the stratification in the stratosphere is not infinite. A “leaky lid" analogy is more accurate, as wave energy can radiate to the stratosphere.

A few studies have investigated the impact of a stratification jump at the tropopause on the evolution of a wave in the atmosphere. Yano and Emanuel (1991) extends the tropical intraseasonal model introduced in Emanuel (1987) by imposing a dry, passive stratosphere above the troposphere, and found that adding a stratosphere strongly damps the smallest scale $v = 0$ waves, shifting the growth rates to the larger scales. Note that Yano and Emanuel (1991) did not look at higher order equatorial waves, and only focused on $v = 0$ waves. By imposing wave-radiation boundary conditions, other studies have found similar effects: that the effect of the stratosphere is a dampening one (Moskowitz and Bretherton, 2000; Kuang, 2008a). Chumakova et al. (2013) further investigates the leaky lid effect by deriving a set of vertical, dissipative modes using the 2-D, linear, Boussinesq equations, overlaying a stratosphere with buoyancy frequency N_2 over a troposphere with buoyancy frequency N_1, where $N_2 > N_1$. In their model, a new barotropic-like mode appears with a fast damping time scale. However, the vertical modes of Chumakova et al. (2013) are not orthogonal; they have also been criticized as unphysical, since the energy is unbounded with height, and they also do not admit steady state solutions to steady state heating (Edman and Romps, 2017). Regardless of the exact specifics in applying a leaky-lid above a troposphere, the inclusion of a stratosphere tends to shift growth rates of unstable modes to larger scales and allows the barotropic mode to be excited.

There have also been many studies that have investigated the role surface friction plays in modifying equatorial waves, and more prominently, the Madden-Julian Oscillation (MJO). These theories based on CISK (conditional instability of the second

kind), in which surface friction was postulated to act, through its induced moisture convergence, as a destabilizing mechanism for convectively coupled equatorial waves (Wang, 1988; Wang and Rui, 1990; Moskowitz and Bretherton, 2000). Wang (1988) and Wang and Rui (1990) formulated a 2.5 layer "frictional WAVE-CISK" model (2 tropospheric layers and a thin frictional boundary layer) in which the barotropic mode can be excited through surface friction. The surface friction acts to induce vertical motion at the top of the boundary layer, which can amplify wave-disturbances if correlated with temperature anomalies. CISK theories have received much criticism [see Emanuel et al. (1994) and Neelin and Yu (1994)], since they violate the convective statistical equilibrium hypothesis, where the rate of production of convectively available potential energy (CAPE) by the large-scale environment is very nearly balanced by its consumption via convection (Arakawa and Schubert, 1974). In the context of surface friction, this means that surface convergence is a by-product and not a driver of convection. Indeed, observations in the tropics support the statistical equilibrium model for convection in the tropics (Betts, 1982; Xu and Emanuel, 1989). Further, numerical simulations of large-scale equatorial waves do not support the idea that surface friction acts as a destabilizing mechanism for large-scale equatorial waves (Chao and Chen, 2001).

Surface friction and boundary layer convergence have also been cited as one mechanism for moistening of the lower troposphere by shallow upward motion east of the MJO center (Wang, 1988; Hsu and Li, 2012; Adames and Wallace, 2014). In theoretical models, this mechanism has been shown to influence the propagation speed and growth rates of the MJO through modulation of the gross moist stability (Sobel and Maloney, 2013; Adames and Kim, 2016).

In this study, we will show how surface friction and interaction with the stratosphere through upward wave energy radiation modifies the characteristics of equatorial waves. The rigid-lid assumption is removed by explicitly coupling a passive and dry stratosphere on top of a convecting troposphere, and the energy density of solutions is enforced to decay with height. Surface drag is imposed on a thin boundary layer at the surface. In particular, we will focus on how the two aforementioned

mechanisms can excite the barotropic mode. More uniquely, the barotropic mode in this study does not separate convective heating from large-scale thermodynamics, and thus it does not violate the strict quasi-equilibrium hypothesis. The study will extend on the results of Yano and Emanuel (1991), which only investigated the impact of surface friction and the stratosphere on the growth rates of $v = 0$, WISHE-amplified equatorial waves.

The paper is organized as follows. Section 3.2 describes the linear model. Section 3.3 presents the solutions of the linear model. The paper concludes with a discussion and summary in section 3.4.

3.2 Linear model

In this section, we describe and formulate the governing equations of our linear model. The model formulation is separated into two parts, section 3.2.1 which describes the tropospheric model, and section 3.2.2 which describes the stratospheric model.

3.2.1 Strict quasi-equilibrium troposphere

KE18 and E20 derive and analyze an equation set for a linear system that describes the dynamics and thermodynamics of an atmosphere that maintains a vertically constant saturation moist entropy s^* in the free troposphere. However, in both of those studies, the authors assume a rigid-lid and frictionless surface. Hence, in their model, only the baroclinic mode can be excited, and upward radiation into the stratosphere is absent.

Here we derive nearly equivalent dynamics, but remove the rigid-lid hypothesis and include the barotropic mode. To begin, we first apply a Galerkin decomposition of the vertical modes of the troposphere and truncate all modes except the first two basis functions, V_0 and V_1, which are defined as the barotropic and baroclinic modes,

respectively (Neelin and Zeng, 2000). Mathematically, they are:

$$V_0 = 1 \tag{3.1}$$

$$V_1 = \frac{\overline{T}(p) - [\overline{T}]}{T_b - [\overline{T}]} \tag{3.2}$$

where $\overline{T}$ is the basic state temperature, T_b is the boundary layer temperature, $[\overline{T}]$ is the pressure-weighted vertical average of temperature. The operator $[\bullet] = \frac{1}{\Delta p}\int_{p_t}^{p_s} \bullet \, dp$ is the pressure-weighted vertical average along a moist adiabat, where p_s is the surface pressure, p_t is the tropopause pressure, and $\Delta p = p_s - p_t$. As is standard for vertical modes, the basis functions are orthogonal, or $\int_{p_s}^{p_t} V_0 V_1 dp = 0$. Furthermore, note that $[V_1] = 0$. From this vertical mode decomposition, we assume separable dependencies between the horizontal and vertical modes as follows:

$$\phi(x, y, p, t) = \phi_0(x, y, t) + \phi_1(x, y, t)$$

and likewise for the other prognostic variables.

For a strict quasi-equilibrium troposphere in which the saturation moist entropy s^* is constant with height, linearized geopotential perturbations are directly connected to s^* perturbations (Emanuel, 1987).

$$\frac{\partial \phi'}{\partial p} = -\left(\frac{\partial T}{\partial p}\right)_{s^*} s^{*\prime} \tag{3.3}$$

where prime superscripts indicate perturbation quantities. The above may be directly integrated from the surface upwards to yield:

$$\phi'(p) = \phi'_b + s^{*\prime}(\overline{T}_b - \overline{T}(p)) \tag{3.4}$$

where ϕ'_b is the geopotential in the boundary layer. When non-dimensionalized (see Appendix B for details), Equation (3.4) yields:

$$\phi'(p) = \phi'_b + (1 - V_1)s^{*\prime} \tag{3.5}$$

Note, the geopotential can be separated into its barotropic and baroclinic components:

$$\phi_0(x, y, t) = (\phi_b' + s^{*\prime})V_0 \tag{3.6}$$

$$\phi_1(x, y, p, t) = -s^{*\prime} V_1 \tag{3.7}$$

The pressure-weighted vertical average operator is also applied to Equation (3.4) to give:

$$\phi_b' = [\phi]' + s^{*\prime}([\overline{T}] - \overline{T}_b) \tag{3.8}$$

which in non-dimensional form is:

$$\phi_b' = \phi_0' - s^{*\prime} \tag{3.9}$$

Unlike the purely baroclinic motions described in KE18, the geopotential now contains contributions from the barotropic mode. Note that Equation (3.5) can be evaluated at the tropopause and combined with Equation (3.9) to obtain the tropopause geopotential ϕ_{tp}', which will be required to couple the system to the stratosphere:

$$\phi_{\text{tp}}' = \phi_0' - V_1(\hat{p}_t)s^{*\prime} \tag{3.10}$$

where $\hat{p}_t$ is the non-dimensional tropopause pressure.

Next, we formulate the full equation of motion on an equatorial β-plane, adding in surface friction, which is represented as applying drag on an infinitesimally small boundary layer.

$$\frac{D\boldsymbol{V}}{Dt} = -\nabla\phi - \hat{k} \times \beta y \boldsymbol{V} - \delta(p - p_s)\frac{C_d}{h_b}|\boldsymbol{V}|\boldsymbol{V} \tag{3.11}$$

where $\boldsymbol{V}$ is the vector wind, β is the meridional gradient of the Coriolis force, δ is the Dirac delta function, p is pressure, C_d is the drag coefficient, and h_b is the boundary layer depth. Note the surface stress is parameterized using the bulk aerodynamic drag formula. Linearizing around surface easterlies, non-dimensionalizing according to details in Appendix B, substituting in Equation (3.5), and dropping all primes of

perturbation quantities, we obtain:

$$\frac{\partial u}{\partial t} = -\frac{\partial \phi_b}{\partial x} + (1 - V_1)\frac{\partial s^*}{\partial x} + yv - 2Fu\delta(\hat{p} - \hat{p}_s) \tag{3.12}$$

$$\frac{1}{\delta_x}\frac{\partial v}{\partial t} = -\frac{\partial \phi_b}{\partial y} + (1 - V_1)\frac{\partial s^*}{\partial y} - yu - \frac{F}{\delta_x}v\delta(\hat{p} - \hat{p}_s) \tag{3.13}$$

where F is the non-dimensional surface friction coefficient and δ_x represents the magnitude of zonal geostrophy [corresponding to δ in KE18]. Note that the factor of 2 appears in Equation (3.12) from assuming mean easterly flow in the zonal direction; it is absent from Equation (3.13) from the assumption of no mean meridional flow. Finally, we project the linearized horizontal momentum equations onto the barotropic and baroclinic modes:

$$\frac{\partial u_0}{\partial t} = -\frac{\partial \phi_0}{\partial x} + yv_0 - 2F(u_0 + u_1) \tag{3.14}$$

$$\frac{1}{\delta_x}\frac{\partial v_0}{\partial t} = -\frac{\partial \phi_0}{\partial y} - yu_0 - \frac{F}{\delta_x}(v_0 + v_1) \tag{3.15}$$

$$\frac{\partial u_1}{\partial t} = \frac{\partial s^*}{\partial x} + yv_1 - 2F(u_0 + u_1) \tag{3.16}$$

$$\frac{1}{\delta_x}\frac{\partial v_1}{\partial t} = \frac{\partial s^*}{\partial y} - yu_1 - \frac{F}{\delta_x}(v_0 + v_1) \tag{3.17}$$

Next, we enforce mass continuity through the continuity equation in pressure coordinates:

$$\frac{\partial u}{\partial x} + \frac{\partial v}{\partial y} + \frac{\partial \omega}{\partial p} = 0 \tag{3.18}$$

where ω is the pressure vertical velocity. Integrating the continuity equation from the surface to the tropopause, non-dimensionalizing, and using the fact that $[V_1] = 0$:

$$\int_{\hat{p}_s}^{\hat{p}_t} \nabla_H \cdot \boldsymbol{V}\, d\hat{p} = \frac{\partial u_0}{\partial x} + \frac{\partial v_0}{\partial y} = \omega(\hat{p}_t) \tag{3.19}$$

where we have used zero vertical velocity condition at the lower boundary, and $\omega(\hat{p}_t)$ is the non-dimensional tropopause vertical velocity. Equation (3.19) shows that the tropopause vertical velocity is only a function of the divergence of the barotropic mode, as the baroclinic mode is zero at the tropopause, by definition.

Finally, the thermodynamic equations in the troposphere link the dynamics to the thermodynamics, and are only slightly modified from KE18 and E20 in that horizontal diffusion is removed and $\kappa = 1$:[1]

$$\frac{\partial s^*}{\partial t} = (1 + C)s_m - w - \alpha u_b - \chi s^* \tag{3.20}$$

$$\gamma \frac{\partial s_m}{\partial t} = -Ds^* - \alpha u_b - Gw + Cs_m \tag{3.21}$$

where s_m is a characteristic moist entropy of the free troposphere, $w = -\frac{\partial u_b}{\partial x} - \frac{\partial v_b}{\partial y}$ is a proxy for the mid-level vertical velocity based on the boundary layer zonal velocity, $u_b = u_0 + u_1$, and boundary layer meridional velocity $v_b = v_0 + v_1$. The non-dimensional coefficients C, α, χ, D, G, and γ are described and formulated in detail in KE18. Briefly, C represents the strength of cloud radiative feedback, α is the wind-induced surface heat exchange (WISHE) feedback parameter, χ is boundary layer damping, D is entropy damping, G is the gross moist stability, and γ modifies the time scale of tropospheric entropy. In this model, the effects of moisture are encapsulated into the vertically integrated moist entropy, which is assumed to change through surface enthalpy fluxes, cloud-radiative feedbacks, vertical advection, and entropy damping. Note that many of the thermodynamic variables are also non-dimensionalized by factors that include the bulk precipitation efficiency (Khairoutdinov and Emanuel, 2018).

Equations (3.14) - (3.17), (3.19)- (3.21) formulate the tropospheric system, where u_0, v_0, u_1, v_1, ϕ_0, s^*, s_m are the unknown variables. Note that the linear system is not complete: additional specification of the vertical velocity at the tropopause is required to complete the system. As mentioned previously, studies that assume a rigid-lid set the tropopause velocity to be zero. Other studies parameterize the tropopause dynamics using a wave-radiation upper boundary condition (Moskowitz and Bretherton, 2000; Kuang, 2008a). In this study, we take a different approach and couple the vertical velocity to an explicit stratosphere model, as will be derived in

[1]The second author discovered that κ, an additional non-dimensional coefficient that scales the cloud-radiative feedback and was defined in KE18 and E20, must be equal to 1 for consistency of the non-dimensional scaling.

section 3.2.2.

3.2.2 Coupling to the stratosphere

In this section, we couple a dry, passive stratosphere to the strict quasi-equilibrium troposphere described in section 3.2.1. We choose to represent a dry and passive stratosphere using the linearized, inviscid primitive equations in log-pressure coordinates and in hydrostatic balance [see Chapter 3 of Andrews et al. (1987)]:

$$\frac{\partial u_s'}{\partial t} = -\frac{\partial \phi_s'}{\partial x} + \beta y v_s' \tag{3.22}$$

$$\frac{\partial v_s'}{\partial t} = -\frac{\partial \phi_s'}{\partial y} - \beta y u_s' \tag{3.23}$$

$$\frac{\partial u_s'}{\partial x} + \frac{\partial v_s'}{\partial y} + \frac{1}{\rho_s}\frac{\partial(\rho_s w_s^{*\prime})}{\partial z^*} = 0 \tag{3.24}$$

$$\frac{\partial}{\partial t}\frac{\partial \phi_s'}{\partial z^*} + w_s^{*\prime} N^2 = 0 \tag{3.25}$$

where subscripts of s denote quantities in the stratosphere, w_s^* is the log-pressure vertical velocity, N^2 is the buoyancy frequency, ρ_s is the basic state density, and the log-pressure vertical coordinate $z^* \equiv -H\ln(p/p_t) + 1$ is defined such that $z^* = 1$ is the bottom boundary, or the tropopause. H is the dimensional tropopause height. Equations (3.22)-(3.25) are non-dimensionalized according to notation shown in Appendix B, with the additional specification that the non-dimensional density decays exponentially with a scale height H_s. The resulting, non-dimensional equations are shown in Equations (3.26) - (3.30), with primes removed from perturbation quantities.

$$\frac{\partial u_s}{\partial t} = -\frac{\partial \phi_s}{\partial x} + y v_s \tag{3.26}$$

$$\frac{1}{\delta_x}\frac{\partial v_s}{\partial t} = -\frac{\partial \phi_s}{\partial y} - y u_s \tag{3.27}$$

$$\frac{\partial u_s}{\partial x} + \frac{\partial v_s}{\partial y} + \frac{1}{\rho_s}\frac{\partial(\rho_s w_s^*)}{\partial z^*} = 0 \tag{3.28}$$

$$\frac{\partial}{\partial t}\frac{\partial \phi_s}{\partial z^*} + w_s^* S = 0 \tag{3.29}$$

$$\rho_s = \exp\left(\frac{H}{H_s}(1 - z^*)\right) \tag{3.30}$$

where S is a non-dimensional stratospheric stratification. For Earth-like parameters, the non-dimensional stratification is in the range of $S \approx [25 - 150]$. A discussion on the parameters that control S is included in the discussion section.

It is important to note that these equations form a complete system by themselves. The stratospheric linear system admits neutral equatorial wave solutions under a rigid-lid upper boundary condition. However, under a upward wave radiation boundary condition, all of the solutions decay exponentially in time since there is no forcing in the stratosphere model and wave energy escapes upwards. Growing solutions that satisfy the upward wave radiation boundary condition in the stratosphere are possible, however, if there is mechanical forcing from the troposphere via the tropopause. In order to investigate these kinds of solutions, we must couple the troposphere system with the stratosphere system in a consistent fashion. Classical coupling conditions require continuity of normal stress across the interface, and continuity of normal displacement to the fluid interface. Since the free-troposphere is modeled as inviscid, the first condition simplifies to continuity of pressure:

$$\phi_s(x, y, z^* = 1, t) = \phi(x, y, p = \hat{p}_t, t) \tag{3.31}$$

Since there is no imposed shear across the tropopause, the second condition implies continuity of vertical velocity:

$$w_s^*(x, y, z^* = 1, t) = -B\omega(x, y, p = \hat{p}_t, t) \tag{3.32}$$

where $B = ((p_s - p_t)/p_t)(H_s/H) > 0$ is a conversion coefficient between pressure coordinates and log-pressure coordinates.

3.2.3 Full, linear model

The troposphere system [Equations (3.14) - (3.17), (3.19) - (3.21)] is coupled to the stratosphere system [Equations (3.26) - (3.30)] through the two matching conditions [Equations (3.31) and (3.32)]. Altogether, these formulate a complete linear system,

in which growing solutions whose energy decays to zero as $z^* \to \infty$ represent modes that grow in the troposphere and propagate vertically into the stratosphere.

3.3 Solutions

The full linear model is a complex system that cannot be easily solved theoretically. However, analyzing the model in the limits of (1) an inviscid surface with coupling to the stratosphere, and (2) a frictional surface under a rigid-lid, allows us to isolate the impacts of both mechanisms. Solutions of the full model, with active surface friction and stratosphere coupling, are then analyzed to illuminate their combined effects.

3.3.1 Leaky modes

In this section, we focus first on solutions of the purely leaky modes, with no surface friction ($F = 0$). The solutions are analyzed separately: modes where $v = 0$ and higher order meridional modes where there is non-zero meridional velocity. In what follows, unless otherwise stated, the primes are dropped from the linear perturbation variables.

$v = 0$ modes

Although the full linear model is extremely complex, restricting the solutions to $v = 0$ allows for tractable analytical insight. In the troposphere, we assume solutions of the form:

$$u_0 = \hat{U}_0(y) \exp(ikx + \sigma t) \tag{3.33}$$

where k is the zonal wave number, σ is the complex growth rate, and capitalized variables with hat notations are the meridional structure functions. Equivalent forms are assumed for ϕ_0, u_1, s, s_m. Solutions in the stratosphere are assumed of the form:

$$u_s = \frac{\hat{U}_s(y)}{\sqrt{\rho_0}} \exp(ikx + \sigma t + im(z^* - 1)) \tag{3.34}$$

where m is the complex vertical wavenumber. Equivalent forms are also assumed for ϕ_s, and w_s^*. As in KE18, the meridional structure Y of the $v = 0$ modes in the troposphere can be derived by combining Equations (3.14) - (3.17):

$$\frac{\partial}{\partial y}\Big(\hat{S}^* - \hat{\Phi}_0\Big) = \frac{iky}{\sigma}\Big(\hat{S}^* - \hat{\Phi}_0\Big) \tag{3.35}$$

Next, we combine Equations (3.14), (3.16), (3.20), and (3.21) to eliminate u_0, u_1, and s_m and obtain the relationship between the meridional function of the saturation moist entropy and the barotropic geopotential:

$$\hat{S}^* = \lambda\hat{\Phi}_0 \tag{3.36}$$

where

$$\lambda = \frac{ika_2 + k^2a_3}{\sigma a_1 + ika_2 + a_3k^2} \tag{3.37}$$

$$a_1 \equiv D(1 + C) + (\chi + \sigma)(\gamma\sigma - C) \tag{3.38}$$

$$a_2 \equiv \alpha(\gamma\sigma + 1) \tag{3.39}$$

$$a_3 \equiv \gamma\sigma + (G - 1)C + G \tag{3.40}$$

Combining Equations (3.35) and (3.36) gives us the meridional structure Y of the troposphere portion of the $v = 0$ modes:

$$Y = \exp\Big(\frac{ik}{2\sigma}y^2\Big) \tag{3.41}$$

which is equivalent in form to the meridional structure of the modes in the rigid-lid case. Furthermore, only solutions with an eastward phase speed satisfy the boundary conditions in y.

Next, we move on to solving the portion of the mode that exists in the stratosphere. With the solution form shown in Equation (3.34), Equations (3.26) - (3.29) reduce

to:

$$\sigma \hat{U}_s + ik\hat{\Phi}_s = 0 \tag{3.42}$$

$$y\hat{U}_s + \frac{\partial \hat{\Phi}_s}{\partial y} = 0 \tag{3.43}$$

$$ik\hat{U}_s + \frac{m^2\sigma}{S}\hat{\Phi}_s = 0 \tag{3.44}$$

where $\hat{W}_s(y) = -\frac{im\sigma}{S}\hat{\Phi}_s(y)$, assuming $m^2 >> (H/2H_s)^2$, which is a vertical short-wave approximation. Equations (3.42) and (3.44) combine into the well-known dispersion relation for the Kelvin-wave:

$$\sigma = \pm i\frac{\sqrt{S}k}{m} \tag{3.45}$$

As shown in Yano and Emanuel (1991), the associated group velocity is:

$$c_{g,z} = \frac{k\sqrt{S}}{|m|^4}\Big(\text{Real}(m)^2 - \text{Imag}(m)^2\Big) \tag{3.46}$$

which indicates that the vertical group velocity increases with zonal wavenumber.

Next, Equations (3.42) and (3.43) combine to give a meridional structure Y that is equivalent to that of the troposphere shown in Equation (3.41). For solutions that obey the meridional boundary conditions, or that the mode amplitudes go to zero as $y \to \pm\infty$, we must have that $\text{Imag}(\sigma) < 0$ (equivalent to an eastward phase speed), so we choose the positive root.

We now apply the matching conditions to derive the dispersion relation. The continuity of pressure condition demands that:

$$\phi_s(x, y, z^* = 1, t) = \phi_0 - V_1(\hat{p}_t)s^* \tag{3.47}$$

Equations (3.14) and (3.19) combine to give the vertical velocity at the tropopause in the troposphere, which must be equal to the vertical velocity at the tropopause in the stratosphere:

$$\omega(\hat{p}_t) = \frac{k^2}{\sigma}\phi_0 = -\frac{1}{B}w_s^* = \frac{1}{B}\frac{im\sigma}{S}\hat{\phi}_s \tag{3.48}$$

where we note the equivalence of a rigid-lid ($\omega(\hat{p}_t) = 0$) to the absence of the barotropic mode. Combining with Equations (3.10), (3.36), (3.45), and (3.47), Equation (3.48) reduces to the dispersion relation:

$$\underbrace{\sigma a_1 + a_4}_{\text{rigid lid}} + \underbrace{\sigma(kB\sqrt{S})^{-1}(\sigma a_1 + \nu a_4)}_{\text{correction}} = 0 \tag{3.49}$$

where $\nu = 1 - V_1(\hat{p}_t)$ and $a_4 = ika_2 + a_3k^2$. As shown in the underbraces, Equation (3.49) is written in the form of the rigid-lid dispersion relation, plus a quartic-order correction term whose magnitude is inversely propotional to the square root of the stratosphere stratification, S. It is clear that in the limit of $S \to \infty$, the dispersion relation reduces to that of the rigid-lid case. The quartic dispersion relation is solved numerically and the solutions are checked rigorously to satisfy the governing equations, boundary conditions, and matching conditions.

Before examining the solutions of the leaky $v = 0$ modes, we first briefly derive the functional form of ω in the troposphere, in the case where $v = 0$. We start by taking the time derivative of the non-dimensional continuity equation and substitute the zonal velocity using Equations (3.14) and (3.16):

$$\sigma\frac{\partial\omega}{\partial\hat{p}} = k^2\phi \tag{3.50}$$

Taking a derivative in pressure allows us to substitute in Equation (3.3) and yields:

$$\sigma\frac{\partial^2\omega}{\partial\hat{p}^2} = -k^2\left(\frac{\partial T}{\partial\hat{p}}\right)_{s^*} s^* \tag{3.51}$$

Integrating in pressure once returns:

$$\sigma\frac{\partial\omega}{\partial\hat{p}} = -k^2 s^*\overline{T}(\hat{p})\Big|_{s^*} + C_0 \tag{3.52}$$

where C_0 is an integration constant that must be determined through the boundary

conditions. We integrate from the surface to the tropopause:

$$\sigma(\omega(\hat{p}_t) - \omega(\hat{p}_s)) = (\hat{p}_s - \hat{p}_t)(-k^2 s^*[\overline{T}] + C_0) \tag{3.53}$$

which allows us to determine C_0:

$$C_0 = \sigma \frac{\omega(\hat{p}_t) - \omega(\hat{p}_s)}{\hat{p}_s - \hat{p}_t} + k^2 s^*[\overline{T}] \tag{3.54}$$

Substituting for C_0 into Equation (3.52), setting $\omega(\hat{p}_s) = 0$ as earlier, and integrating once in pressure yields the non-dimensional vertical structure of ω:

$$\omega(\hat{p}) = \underbrace{\frac{\hat{p}_s - \hat{p}}{\hat{p}_s - \hat{p}_t}\omega(\hat{p}_t)}_{\text{barotropic}} - \underbrace{\frac{k^2}{\sigma} s^* \int_{\hat{p}_s}^{\hat{p}} V_1 \, dp}_{\text{baroclinic}} \tag{3.55}$$

As shown in the underbraces, the vertical structure of the pressure vertical velocity is a sum of the barotropic and baroclinic modes. The barotropic component changes linearly with pressure, and the baroclinic mode is zero at the surface/tropopause and peaks in the mid-troposphere. The superposition of the barotropic and baroclinic mode can lead to a vertical tilt in the vertical velocity profile that depends on the phase lag between the two modes. It is worth noting that by definition, the baroclinic mode cannot interact with the stratosphere; in this model, it is only through the excitement of the barotropic mode that waves can radiate energy into the stratosphere.

Figure 3-1 compares the non-dimensional frequency, growth rates, phase speeds, and vertical group velocity of the leaky $v = 0$ modes to those of the rigid-lid modes, with non-dimensional coefficients $\alpha = 1.5$, $\chi = 0.5$, $C = 0$, $\gamma = 2$, $D = 0.5$, $G = 0.1$, $S = 100$. These parameters somewhat reflect Earth-like conditions in the tropics, with the exception of no cloud radiation interaction, and were specifically chosen to examine the branch of solutions that closely resemble the classical Kelvin-wave solutions but are instead amplified through the WISHE feedback. Figure 3-1a shows that the frequencies of the leaky waves are only slightly larger than their rigid-lid counterparts, and as such the phase speeds are slightly faster (Figure 3-1c). The

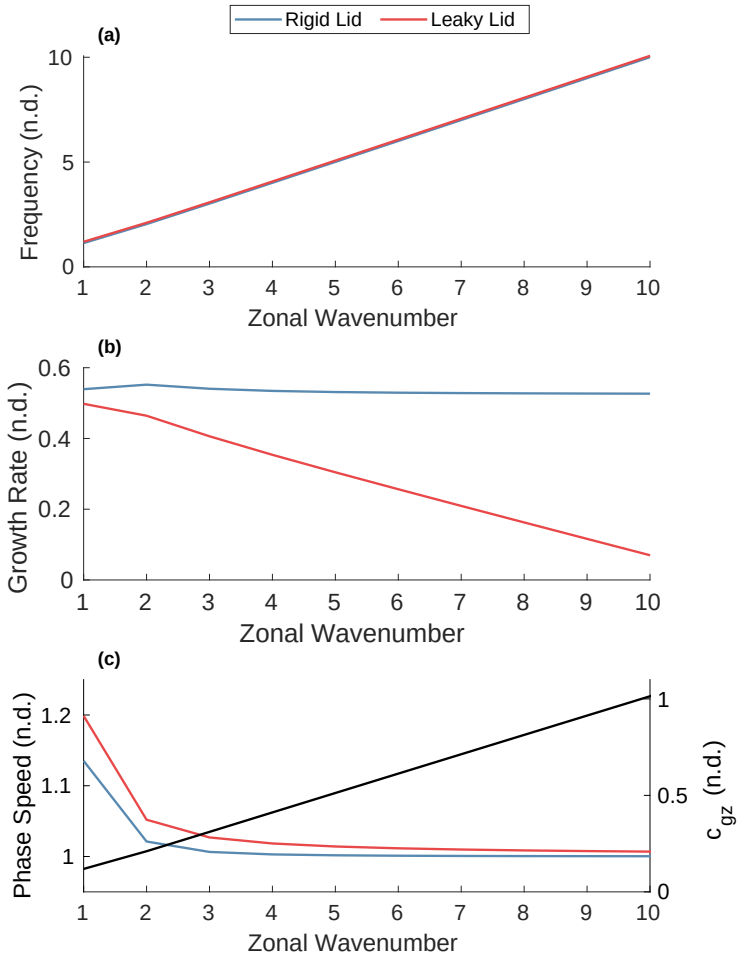

Figure 3-1: Non-dimensional (a) frequency, (b) growth rate, (c) phase speed and for the fastest growing $v = 0$ mode. Vertical group velocity of the leaky mode is shown in black in the bottom panel, while rigid-lid solutions are shown in blue and leaky-lid solutions shown in red. Non-dimensional parameters are $\alpha = 1.5$, $\chi = 0.5$, $C = 0$, $\gamma = 2$, $D = 0.5$, $G = 0.1$, $S = 100$.

modification of the growth rates tell a much different story: Figure 3-1b shows strong damping of the growth rate of smaller-scale waves, shifting the power spectrum towards larger scale waves, which is consistent with the results of Yano and Emanuel (1991). This reddening of the power spectrum can be physically explained through the large vertical group velocities of the smaller scale waves, as shown in Figure 3-1c and indicated in Equation (3.46). The smaller scale waves propagate their energy very quickly into the stratosphere, dampening their growth rate. For instance, the $k = 10$ wave has a vertical group velocity that nearly exceeds its zonal phase speed.

Figure 3-2 shows a summary of the $k = 1$ eigenfunction using identical non-dimensional parameters as detailed in Figure 3-1. The horizontal cross-section at the surface shows a Kelvin-wave pattern with surface easterlies maximizing east of the maximum temperature anomaly. Vertical velocity maximizes west of the peak temperature anomalies, and the WISHE feedback is responsible for wave growth and enhanced eastward propagation. The horizontal structure is not significantly modified from that of the rigid-lid. The vertical structure of the mode exhibits a bit more complexity. Unlike the vertical structure of the rigid-lid model, which is purely baroclinic, the superposition of the barotropic and baroclinic modes leads to an eastward vertical tilt in dynamical fields, as shown in Figure 3-2 and Equation (3.55). Note the temperature anomalies are purely first baroclinic, since the barotropic mode is not associated with temperature perturbations The mode has a downward phase propagating, eastward tilted component in the stratosphere, which is consistent with a Kelvin-wave that has upward vertical energy propagation. As indicated by the dispersion relation, the vertical wavelength in the stratosphere is controlled by the horizontal wavenumber and stratification; a stronger stratification or shorter horizontal wavelength decreases the vertical wavelength.

The tropospheric system also allows for solutions of significantly slower propagating modes when cloud-radiation interaction is turned on, as shown in KE18 and E20. We select the non-dimensional parameters $\alpha = 1$, $\chi = 1$, $C = 2.5$, $\gamma = 2$, $D = 1$, $G = 0.02$, $S = 100$, in order to obtain the slow modes as the fastest growing solutions. Note that these parameters are slightly different from those used in E20, but

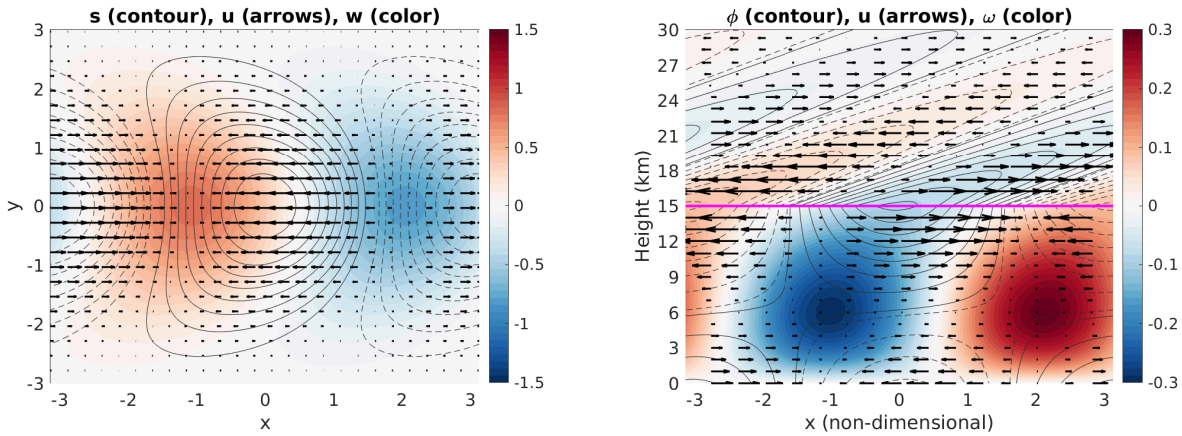

Figure 3-2: Eigenfunction of the $v = 0$, $k = 1$ mode corresponding to the parameters detailed in Figure 3-1, on a (left) horizontal cross-section at the surface, and (right) vertical cross-section centered on the equator. Contours indicate the saturation entropy or geopotential, where solid (dashed) lines indicate positive (negative) perturbations. Arrows indicate zonal velocity perturbations, and color shading indicates vertical velocity or ω perturbations, where indicated. Magenta line outlines the tropopause.

still within Earth-like ranges. The use of slightly different parameters was motivated in part to compensate for the recognition that $\kappa = 1$. We also eliminated horizontal diffusion of moist static energy as compared to the model described in KE18, in order to isolate the effect of the stratosphere on the growth rates. This means that the growth rates no longer peak at low wavenumbers, contrary to what is observed, suggesting that horizontal advection may play an important role in scale-selection for slow-propagating waves. We have confirmed that the different non-dimensional parameters used and the removal of the horizontal diffusion term does not change the general structure and properties of the slow-propagating waves (not shown). Figure 3-3 shows the frequency, growth rate, phase speed, and vertical group velocities for the $v = 0$ slow modes that can interact with the stratosphere. Aside from a small modification of the wave properties at the highest wave numbers, these slow modes are not significantly affected by the presence of a stratosphere. Their vertical group velocities are almost negligibly small, and the corresponding vertical wavelengths in the stratosphere are extremely short. These slow modes are trapped in the troposphere and do not leak much energy into the stratosphere. Thus, these results suggest that

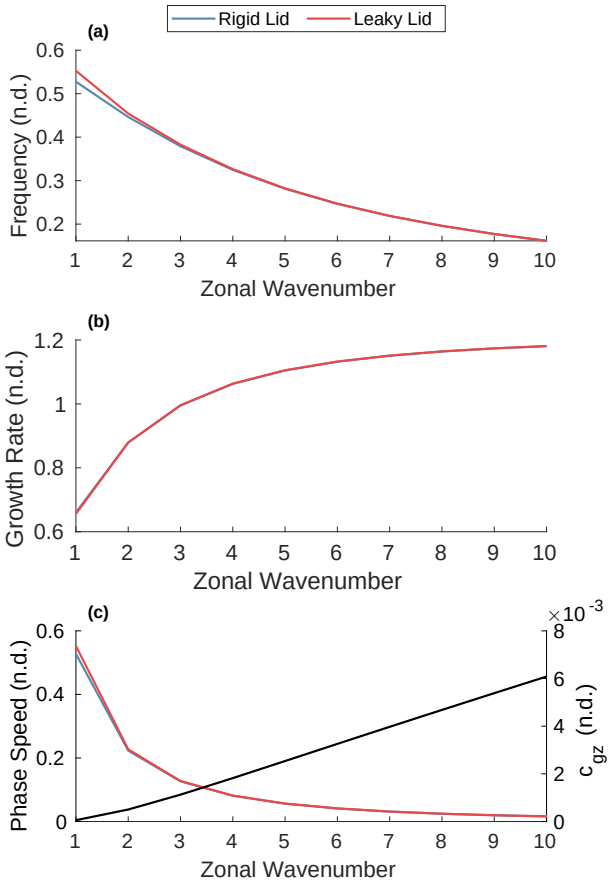

Figure 3-3: Analogous to Figure 3-1, but for the fastest-growing mode with non-dimensional parameters $\alpha = 1$, $\chi = 1$, $C = 2.5$, $\gamma = 2$, $D = 1$, $G = 0.02$, $= 100$.

for slow propagating modes, such as the MJO, a rigid-lid assumption is an accurate approximation with regards to the growth rates.

Next, we investigate the barotropic mode magnitude and phase tilt across a range of non-dimensional parameters. Combining Equations (3.14), (3.16), and (3.36) under $v = F = 0$ yields the relationship between the baroclinic and barotropic zonal velocities:

$$-\lambda u_0 = u_1 \tag{3.56}$$

Here, it is evident that λ controls the phase and amplitude relationship between the barotropic and baroclinic modes. From Equation (3.56), the ratio of the amplitude of the barotropic to that of the baroclinic mode is equivalent to $|-\lambda^{-1}|$, while the phase lead of the barotropic to baroclinic mode is given by $\tan^{-1}(\lambda_i/\lambda_r)$, where λ_i

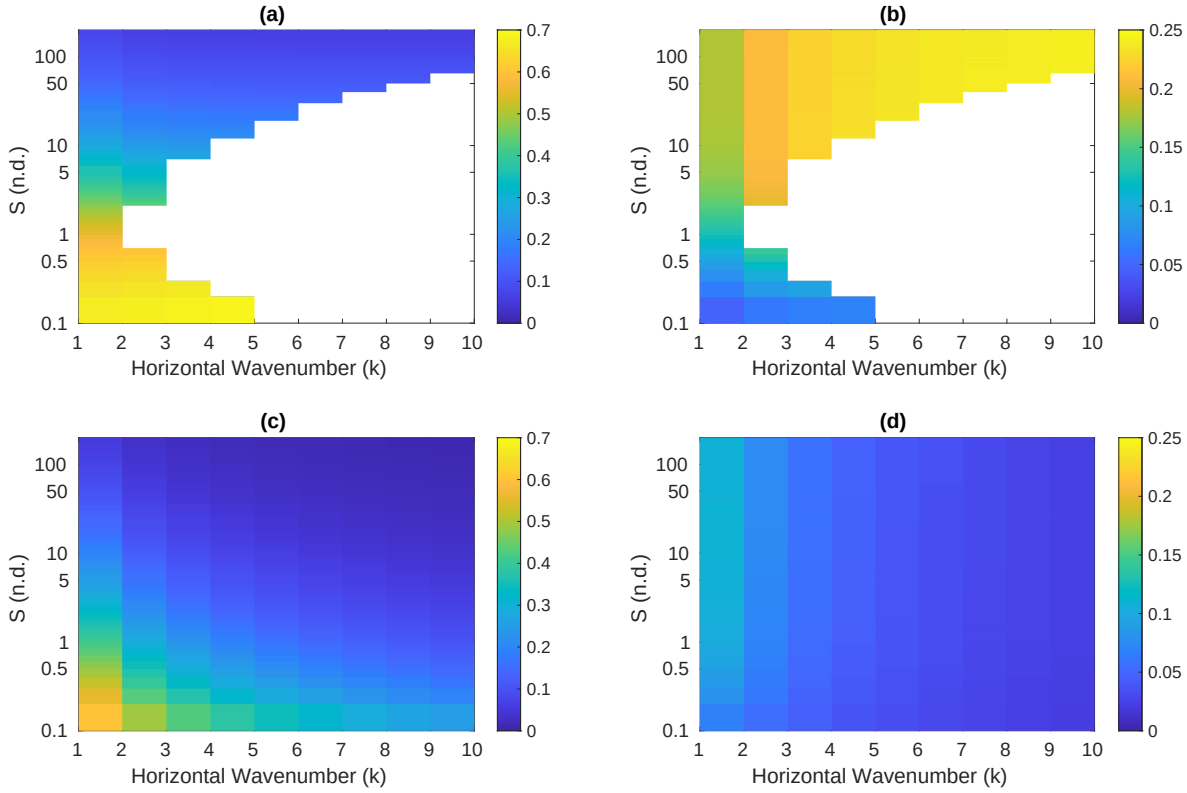

Figure 3-4: (a, c) Barotropic zonal velocity to total zonal velocity ratio $[|u_0 \ / \ (u_0 + u_1)| = |-(\lambda - 1)^{-1}|]$, and (b, d) phase lead of the barotropic mode with respect to the baroclinic mode, $[\tan^{-1}(\lambda_i/\lambda_r)]$, in cycles, as functions of stratosphere stratification, S, and horizontal wavenumber. (a, b) Top row generated using the non-dimensional parameters described in Figure 3-1 (WISHE-modified Kelvin waves), and (c, d) bottom row generated using the non-dimensional parameters described in Figure 3-3 (slow $v = 0$ modes). White area indicates non-growing modes.

and λ_r are the imaginary and real components of λ, respectively. It follows that the barotropic zonal velocity to total zonal velocity ratio is $|u_0/(u_0+u_1)| = |-(\lambda-1)^{-1}|$.

Figure 3-4a and Figure 3-4c show the barotropic zonal velocity to total zonal velocity ratio, as well as the phase lead of the barotropic mode to the baroclinic mode, for a wide range of stratosphere stratification S. In general, we observe decreasing amplitude of the barotropic mode with increasing stratosphere stratification and zonal wavenumber. For both the classical WISHE-driven Kelvin waves (Figure 3-4, top row) and radiatively destabilized slow modes (Figure 3-4, bottom row), the barotropic mode is around an order of magnitude smaller than the baroclinic mode for Earth-like parameters. Furthermore, the barotropic mode leads the baroclinic

mode by approximately 0.1-0.2 cycles (0.25 being a quarter cycle, or $\pi/2$). The phase lead of the barotropic mode is always positive, indicating that the eastward phase tilt in dynamical fields shown in Figure 3-2 is robust across a wide-range of scales and S. In addition, an exploration of the non-dimensional parameter space did not find any solutions where the barotropic mode lagged the baroclinic mode (not shown). This result is consistent with physical intuition. For the WISHE-driven $v = 0$ modes, the baroclinic easterlies peak east of the maximum temperature perturbation. If the barotropic zonal velocities are instead westward of the baroclinic zonal velocities, then the total surface easterlies could peak west of the maximum temperature anomalies, which is inconsistent with an WISHE-driven eastward propagating mode. Note, this is inconsistent with observational analyses of convectively coupled Kelvin waves, in which a westward tilts with height in zonal wind and temperature are typically observed (Straub and Kiladis, 2002). But, an explanation of the westward tilt with height in *temperature* is futile to search for in a strict quasi-equilibrium model, since the barotropic mode is not associated with temperature perturbations. Rather, this analysis shows that the barotropic mode, at least in WISHE-amplified Kelvin waves in which quasi-equilibrium restricts the vertical structure of buoyancy anomalies, is eastward of the first baroclinic mode. Regardless, the observed westward tilt with height in temperature may indeed indicate the importance of the second baroclinic mode over the barotropic mode for Kelvin waves (Mapes, 2000; Kuang, 2008a), though it is also possible to obtain the observed tilt with height in temperature in simple models where a first-baroclinic mode heating rate is imposed and convective inhibition is allowed to modulate precipitation (Raymond and Fuchs, 2007). It is likely true that strict quasi-equilibrium, as employed in this study, is too restrictive an assumption for the fast-moving Kelvin waves, but relaxation of this assumption in a coupled troposphere-stratosphere model is beyond the scope of this study.

Finally, it is worth noting that the u_0 magnitude is larger than the u_1 magnitude for extremely leaky stratospheres (Figure 3-4); though this may not be relevant to Earth's atmosphere, a barotropic mode that exceeds its baroclinic counterpart leads to top-heavy vertical velocity profiles and fast propagation into the stratosphere.

Higher order modes

Without the $v = 0$ approximation, the solution set is extremely complex. In the rigid-lid case, the meridional structure of the eigenmodes of the full equations are parabolic cylinder functions of degree n, where n is the order of the Hermite polynomial. A brief mathematical analysis of the (intractable) leaky-lid solutions suggests that the meridional structure functions of the linear solutions are sums of parabolic cylinder functions. Note that by convention, we denote $n = -1$ solutions as those where $v = 0$.

For these higher order modes, we instead solve the linear problem using numerical code, which is only appropriate for finding growing modes. The troposphere system [Equations (3.14) - (3.17), (3.20) - (3.21)] is discretized in y, while the stratosphere system [Equations (3.26) - (3.29)] are discretized in y and z. Solutions are assumed to have a zonal structure of the form $\exp(ikx)$. In order to integrate the linear system in time, the stratosphere equations need to be transformed to a set of linear prognostic equations. The mass continuity equation [Equation (3.28)] is first integrated from the lower boundary in z^*, to obtain:

$$\rho_s w_s^*(y, z^*) = w_s^*(y, z^* = 1) - \int_{z^*=1}^{z} \Big[\rho_s \Big(iku_s(y, z^*) + \frac{\partial}{\partial y} v_s(y, z^*) \Big) \Big] dz^* \tag{3.57}$$

where the tropopause velocity $w^*(z^* = 1)$ is equal to the vertical velocity at the tropopause in the troposphere equations, as required from the vertical velocity matching condition. Given the vertical velocity, Equation (3.29) can be used to calculate the geopotential:

$$\frac{\partial}{\partial t}\frac{\partial}{\partial z}\phi(y, z^*) = -w^*(y, z)S \tag{3.58}$$

Integrating from the upper boundary downwards gives the prognostic equation for ϕ_s:

$$\frac{\partial}{\partial t}\phi_s(y, z^*) = -\int_{\infty}^{z} w_s^*(y, z^*)S \, dz^* + C_0 \tag{3.59}$$

where C_0 must be determined by the upper boundary condition. An upwards wave-radiation boundary condition could be applied to determine C_0, as in Moskowitz and Bretherton (2000), but such a condition does not exist for the slower modes that

have interactive cloud radiation and no clear analog in the stratosphere. While it is not necessary that $\phi_s = 0$ as $z \to \infty$ (as long as the energy density goes to zero), we have included a Newtonian damping in a sizeable layer extending from the upper boundary, and as such, we set $C_0 = 0$. Another advantage of the Newtonian damping in the upper part of the domain is to eliminate any nonphysical downward propagating modes. For realistic values of S, however, the amplitude of the modes typically decay to zero at the top of the numerical domain. Finally, $\phi_s(y, z^* = 1)$ is connected to the troposphere through the continuity of pressure matching condition [Equation (3.47)].

Spatial derivatives are approximated using fourth-order central differences, and the system is forward time-stepped using fourth order Runge-Kutta. After specifying non-dimensional parameters, the corresponding rigid-lid solution is used to initialize the troposphere domain, while the stratosphere is initialized at rest. Since the unbalanced wave must undergo rapid gravity-wave adjustment, several dampening mechanisms are used to eliminate spurious gravity-wave energy. A spectral filter is applied at each time step to eliminate small-scale noise. A strong sponge-layer is included along the edges and top of the domain to eliminate reflection of gravity waves, downward propagating waves, and spurious noise. For details on the mathematical form of the full numerical system, see Appendix B. The system is integrated for a long period of time, during which the domain is periodically rescaled by a constant to prevent numerical overflow. We then isolate the growing mode of interest and infer both the complex growth rate and meridional/vertical structures. The real component of the growth rate is calculated by the linear slope of the time-varying log of the amplitude of a prognostic variable (after accounting for the rescaling). The imaginary component of the growth rate is calculated by the slope of the time-varying phase of a prognostic variable. Although we initially assume that the damping at the upper boundary does not significantly affect the stratospheric solution, the corresponding growth rate and the meridional structures of all prognostic variables are rigorously checked to satisfy the governing equations, boundary conditions, and matching conditions. As a partial test of correctness of the numerical code, the numerical solutions for the $v = 0$ ($n = -1$) modes were cross-referenced with the $v = 0$ analytic solutions.

The numerical solution is robust for linear solutions that are the fastest growing equatorially symmetric or asymmetric mode. However, for solutions that are not the fastest growing mode, initial unbalanced energy and/or numerical error that projects onto the fastest growing mode symmetric/asymmetric mode will cause the slower growing mode to be overtaken by the fastest growing mode before the domain energy is concentrated solely in the mode of interest. For instance, the second fastest growing equatorially symmetric mode can be overtaken by the fastest growing equatorially symmetric mode. In these cases, the meridional/vertical structure of the fastest growing mode is isolated by integrating for a long period in time. Then, the fastest growing mode is projected onto the domain output, and removed from the fields. If the second fastest growing mode does not have a weak growth rate, the remaining, filtered fields will contain the mode of interest for a long enough period of time to infer the complex growth rate and structure.

WISHE classical modes We first compare the leaky wave solutions to the rigid-lid solutions for the WISHE-destabilized classical modes of the equatorial waveguide. This is done by choosing $\alpha = 3.5$, $\chi = 0.5$, $C = 0$, $\gamma = 1$, $D = 2.5$, $G = 0.25$, $\delta_x = 15$, $S = 75$; note that $C = 0$ eliminates the slower propagating modes observed in KE18 and E20. Figure 3-5 shows the non-dimensional growth rates and phase speeds for select meridional orders $n = -1, 0, 1, 2$ leaky equatorial waves. The growth rates of the Kelvin, westward and eastward mixed Rossby-gravity, and inertia-gravity waves are clearly dampened in relation to their rigid-lid counterparts. The strength of dampening, in a percent relative sense, grows stronger with increasing wavenumber for the eastward modes. This is in contrast to the almost negligible dampening of the westward propagating modes as $|k|$ increases. The growth rates of the westward propagating $n = 0$ and $n = 1$ waves are not strongly affected by the stratosphere. The phase speeds of the leaky-waves are almost negligibly faster than their rigid-lid counterparts, with the largest, though still slight, modifications observed for the $n = -1$ solutions. The growth rates for smaller scale eastward propagating waves are further dampened with reduced stratification in the stratosphere (compare $S = 75$

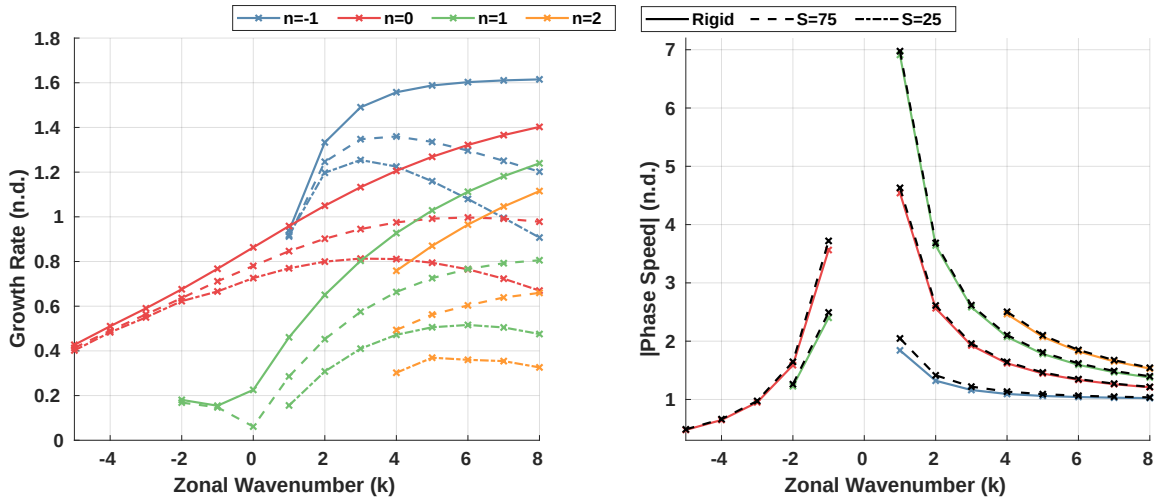

Figure 3-5: (Left) Non-dimensional growth rate for the $n = -1, 0, 1, 2$ modes of the (solid) rigid-lid system, the (dashed) leaky-lid system with $S = 75$, and the (dot-dashed) leaky-lid system with $S = 25$. (Right) Non-dimensional phase speed for the same modes, in the (solid) rigid-lid and (black-dashed) leaky-lid system with $S = 75$. $k <= 3$ for $n = 2$, and $k <= 0$ for $n = 1$ for $S = 25$ solutions are omitted since they do not grow rapidly enough to infer the complex growth rate. Non-dimensional parameters selected for these modes are $\alpha = 3.5$, $\chi = 0.5$, $C = 0$, $\gamma = 1$, $D = 2.5$, $G = 0.25$, $\delta_x = 15$.

to $S = 25$). The effect is quite pronounced; in the case shown in Figure 3-5, the smallest scale rigid-lid modes possess the largest growth rates, but imposing a leaky stratosphere greatly shifts the growth rates towards larger scales. For the $S = 25$ case, the growth rate peaks at $k = 3$ for the $n = -1, 0$ modes, and $k \approx 5$ for the $n = 1, 2$ modes. These results are consistent with the qualitative behavior shown in the mathematical analysis of the leaky $v = 0$ modes. As such, the solutions suggest that the stratosphere acts as a reddener of the equatorial power spectrum, especially for eastward propagating waves.

Slow modes We next switch to a non-dimensional parameter set in which cloud radiative feedbacks are turned on, such that the slow modes analyzed in E20 are the fastest growing modes. In particular, we choose $\alpha = 1$, $\chi = 1$, $C = 2.5$, $\gamma = 2$, $D = 1$, $G = 0.02$, $\delta_x = 30$, $S = 100$. Although the westward propagating slow modes do grow in time under the rigid-lid model, they take too long to reach steady state and are quickly overtaken by the eastward propagating modes. We thus focus on the eastward

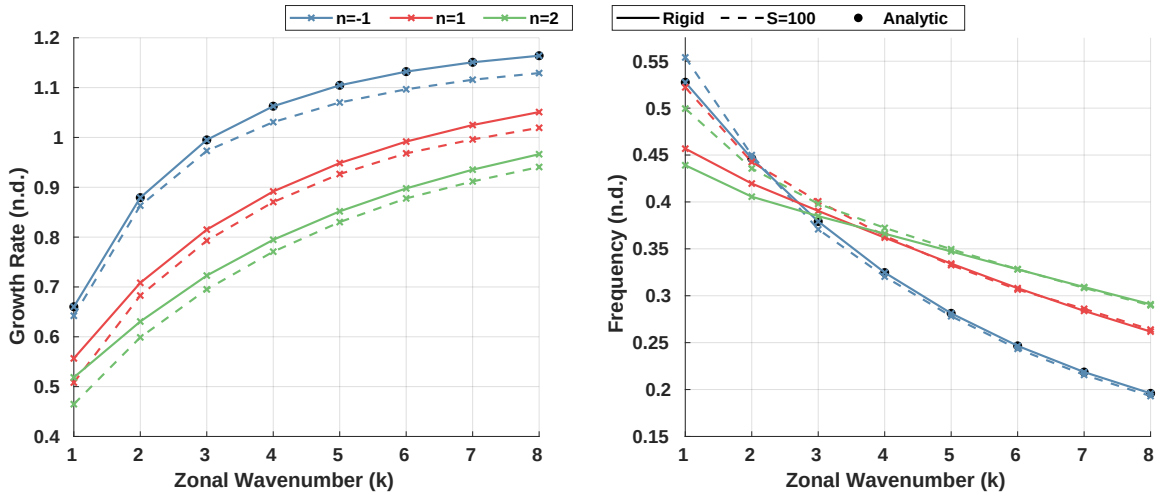

Figure 3-6: (Left) Non-dimensional growth rate for the $n = -1, 1, 2$, eastward propagating slow modes of the (solid) rigid-lid system, and the (dashed) leaky-lid system with $S = 100$ inferred from the numerical solution. (Right) Non-dimensional frequency for the same modes, in the (solid) rigid-lid and (dashed) leaky-lid system with $S = 100$. Black dots indicate the analytic solutions of the growth rate and frequencies of the $n = -1$ slow modes. All $n = 0$ solutions are not growing. Non-dimensional parameters selected for these modes are $\alpha = 1$, $\chi = 1$, $C = 2.5$, $\gamma = 2$, $D = 1$, $G = 0.02$, $\delta_x = 30$.

propagating slow modes, which have a much clearer analog in the real atmosphere (i.e. the MJO).

Figure 3-6 shows the non-dimensional growth rates and frequencies for the eastward propagating $n = -1, 1, 2$ slow modes. We first compare the numerical $n = -1$ solutions to the analytic solutions (Figure 3-6, black dots). We observe that the numerical model slightly dampens the growth rate, and only negligibly modifies the frequencies. This slight damping could be attributed to the spectral filter and/or numerical error. Assuming that the numerical error affects the wave characteristics of the $n = 1, 2$ slow modes the same way, we can infer that like the growth rates and frequencies of the leaky $n = -1$ slow modes, the growth rates and phase speeds of the higher order slow modes are not affected by the presence of the stratosphere.

Perhaps of greater interest is how the slow modes interact with the stratosphere through the barotropic mode. We focus on the eastward propagating $n = 1$, $k = 2$ mode which has a horizontal structure that closely resembles that of the observed MJO (Emanuel, 2020). Figure 3-7 shows the horizontal and vertical structure of the

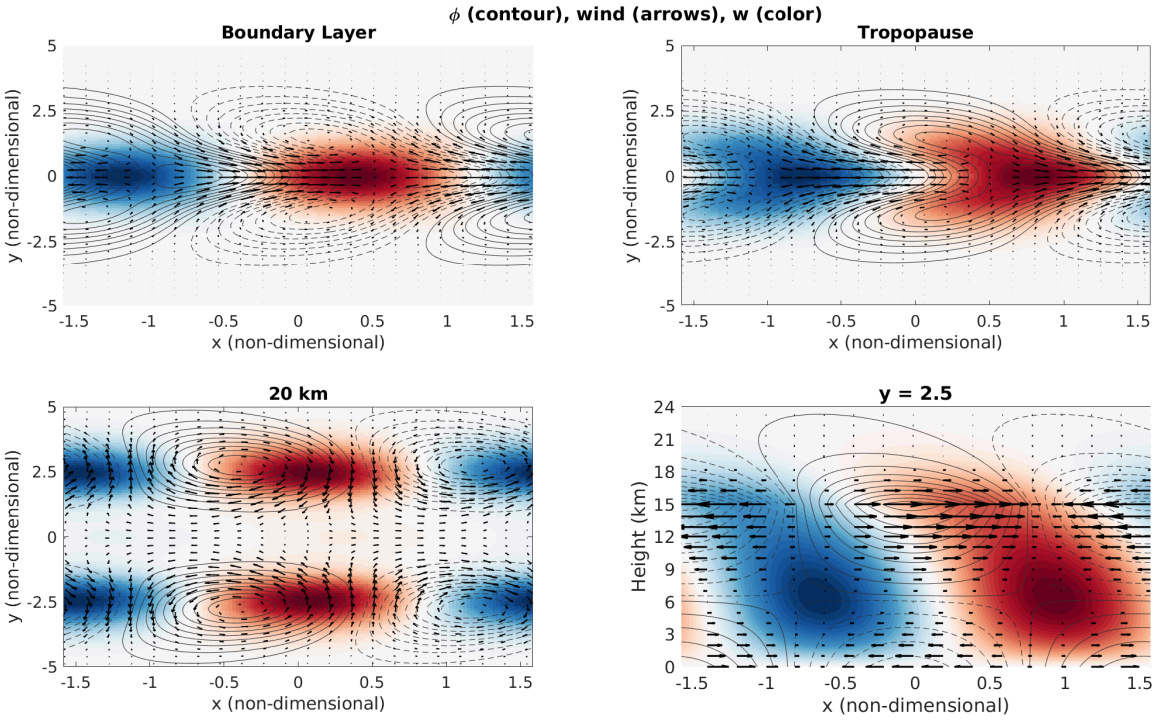

Figure 3-7: Eigenfunction of the $n = 1$, $k = 2$ mode corresponding to the parameters detailed in Figure 3-6, on a horizontal cross-section at the (top left) the surface, (top right) tropopause [15 km], (bottom left) 18 km. Vertical cross section eigenfuction at $y = 2.5$ is shown on the bottom right. Contours indicate the geopotential, where solid (dashed) lines indicate positive (negative) perturbations. Arrows indicate wind perturbations, and color shading indicate vertical velocity perturbations at the level indicated, except for the boundary layer cross-section, where color shading indicates mid-level vertical velocity.

$n = 1$, $k = 2$ mode, where we observe surface cyclonic gyres westward and poleward of the area of maximum ascent. Strong westerlies are also observed westward of the maximum ascent region. The boundary layer horizontal structure very closely resembles that of the rigid-lid solution (not shown). At the tropopause (Figure 3-7, top right), the horizontal structure is almost nearly the opposite of the horizontal structure at the surface, indicating the prominence of the first baroclinic mode. However, the vertical velocity at the tropopause is non-zero, and the pattern extends poleward into the cyclonic/anti-cyclonic gyres, an indication of the presence of the barotropic mode. If we move further up into the stratosphere, at around 20 km (Figure 3-7, bottom left), the signature of the equatorial portion of the tropospheric wave disappears, and the poleward cyclonic/anti-cyclonic gyres become the prominent pattern. These gyres have a westward tilt with height, as indicated in the vertical cross section at $y = 2.5$ (Figure 3-7, bottom right), though their amplitudes decay exponentially with height and are much smaller with respect to the amplitudes of the corresponding gyres in the troposphere. This indicates that the barotropic mode lags the baroclinic mode; in addition, the westward tilt height height observed here is consistent with an upward propagating Rossby wave. At the equator, the $n = 1$, $k = 2$ slow mode has a very weak eastward tilt with height (not shown), since the barotropic mode leads the baroclinic mode. Like the $v = 0$ mode shown in Figure 3-2, in the stratosphere, the slow mode also tilts eastward with height at the equator (not shown). This is consistent with the stratospheric eastward tilt with height of the zonal wind on the equator of observational MJO composites [see fig. 3 of Kiladis et al. (2005)].

3.3.2 Frictionally modified modes

In this section, we consider how surface friction can also excite the barotropic mode. First, we simplify the linear system in the rigid-lid limit, but now with non-zero surface friction. From Equation (3.19), if $\omega(\hat{p}_t) = 0$, it follows that the barotropic mode is non-divergent. However, the solution cannot be solved in terms of a non-divergent stream function ψ_0, since δ_x scales the meridional momentum equation but not the mass continuity equation. Instead, we take the divergence of Equations (3.14)

and (3.15), yielding:

$$\Big(\delta_x \frac{\partial^2}{\partial y^2} - k^2\Big)\phi_0 = y\Big(ikv_0 - \delta_x \frac{\partial u_0}{\partial y}\Big) - \delta_x u_0 - 2Fik(u_0 + u_1) - F\frac{\partial}{\partial y}\Big(v_0 + u_1\Big) \quad (3.60)$$

From Equation (3.60), we see that a barotropic mode at rest cannot be excited if there is no surface friction ($F = 0$). Thus, surface friction acts to couple the barotropic mode with the baroclinic mode; since the forcing is primarily in the first baroclinic mode; it is the first baroclinic mode that excites the barotropic mode.

The barotropic geopotential ϕ_0 is solved by inverting Equation (3.60). Equations (3.14) - (3.17), (3.20), (3.21) form the complete linear system. The system is solved numerically by discretizing in y. Spatial derivatives are again approximated using fourth-order central differences, and the system is forward time-stepped using fourth order Runge-Kutta. As before, the frictionless, rigid-lid solution is used to initialize the domain, after which we integrate the system for a long period of time and then isolate the growing mode of interest.

Before proceeding, it is important to note that the $n = -1$ modes in this section differ from the traditional definition of $v = 0$, in that the meridional wind is allowed to be non-zero but small. This is deliberately chosen, since $v_0 = v_1 = 0$ solutions under zero vertical velocity boundary conditions require the barotropic mode to be divergence free; this is only achievable for non-zero u_0 if there are also nonzero v_0. While solutions of $v_0 = v_1 = 0$ under the aforementioned conditions do exist, they are just classical frictionally damped baroclinic mode solutions. However, we are interested in the solutions in which the barotropic mode can be excited, and as such, allow v to be small for the $n = -1$ modes. We investigate the complex growth rates as a function of the non-dimensional surface friction, F, for which an Earth-like range is $F \approx 0.1 - 0.4$. Figure 3-8 shows the growth rate of the $n = -1$, $n = 0$, and $n = 1$ modes for the same parameter choices as in Figure 3-5, which selects for WISHE-modified Matsuno modes. Figure 3-8 indicates that the surface friction acts as a damping effect on all wavelengths, and the strength of the damping is nearly constant across all wavelength. This is expected as the aerodynamic drag law acts on

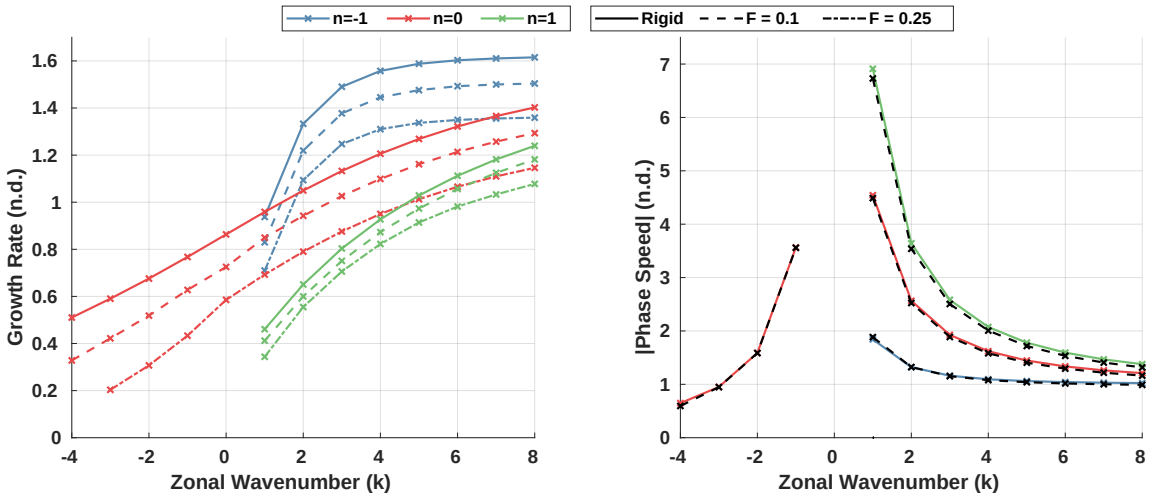

Figure 3-8: (Left) Non-dimensional growth rate for the $n = -1, 0, 1$ modes of the (solid) rigid-lid system, the (dashed) surface friction + rigid-lid system with $F = 0.1$, and the (dot-dashed) surface friction + rigid-lid system $F = 0.25$. $n = -1$ modes differ from the traditional definition of $v = 0$, in that the meridional wind is allowed to be non-zero but small. (Right) Non-dimensional phase speed for the same modes, in the (solid) rigid-lid and (black-dashed) surface friction + rigid-lid system with $F = 0.1$. All $n = 2$, and $n = 1$ for $k <= 0$ solutions are omitted since they do not grow rapidly enough to infer the complex growth rate. Non-dimensional parameters selected for these modes are $\alpha = 3.5$, $\chi = 0.5$, $C = 0$, $\gamma = 1$, $D = 2.5$, $G = 0.25$, $\delta_x = 15$.

a fixed damping time scale. The phase speeds are not significantly changed from the phase speeds of the rigid-lid modes. The results are consistent with our formulation of surface friction, in that surface friction does not “force convection", as convection is assumed to be in a strict, statistical equilibrium.

As illustrated in Equation (3.60), surface friction can lead to an excitation of the barotropic mode, even under a rigid lid. Figure 3-9a and Figure 3-9b show the meridional structure of the $n = -1$, $k = 1$ barotropic zonal and meridional velocities as compared to their baroclinic counterparts. Like the leaky-lid case, the barotropic zonal wind magnitude is around an order of magnitude smaller than the baroclinic mode. However, while the baroclinic mode magnitudes are primarily confined close to the equator (around $y = -5$ to $y = 5$), the barotropic mode wind velocities have long tails that extend far away from the equator. To understand this effect, at least on a high level, we consider neutral barotropic and baroclinic equatorial waves. Since a neutral barotropic wave will have a larger phase speed (and equivalent depth) than a neutral baroclinic wave, it will consequently have a larger meridional length scale and a more polewards turning latitude [see eq. 8.77 in Vallis (2017)]. This qualitatively explains the increased poleward extent of the barotropic mode as compared to the baroclinic mode. The barotropic mode might be an important teleconnection mechanism between the tropics and the extratropics, but further analysis of this effect is out of the scope of this study (Horel and Wallace, 1981). An important caveat to note, however, is that a rigid-lid barotropic mode is completely trapped in the troposphere; the addition of a leaky stratosphere may limit the poleward extent of the barotropic mode, as will be examined in the next section.

Under a rigid lid the non-divergent barotropic mode cannot be associated with vertical velocity perturbations, though a vertical tilt can still exist in the horizontal wind fields from the superposition of the barotropic and baroclinic horizontal winds. Figure 3-9d shows the vertical cross section on the equator of the $n = -1$, $k = 1$ mode. The vertical structure of the vertical velocity is only first baroclinic, despite the zonal wind exhibiting a slight eastward vertical tilt. This eastward vertical tilt in the zonal wind field is consistent with the eastward tilt observed in the purely leaky

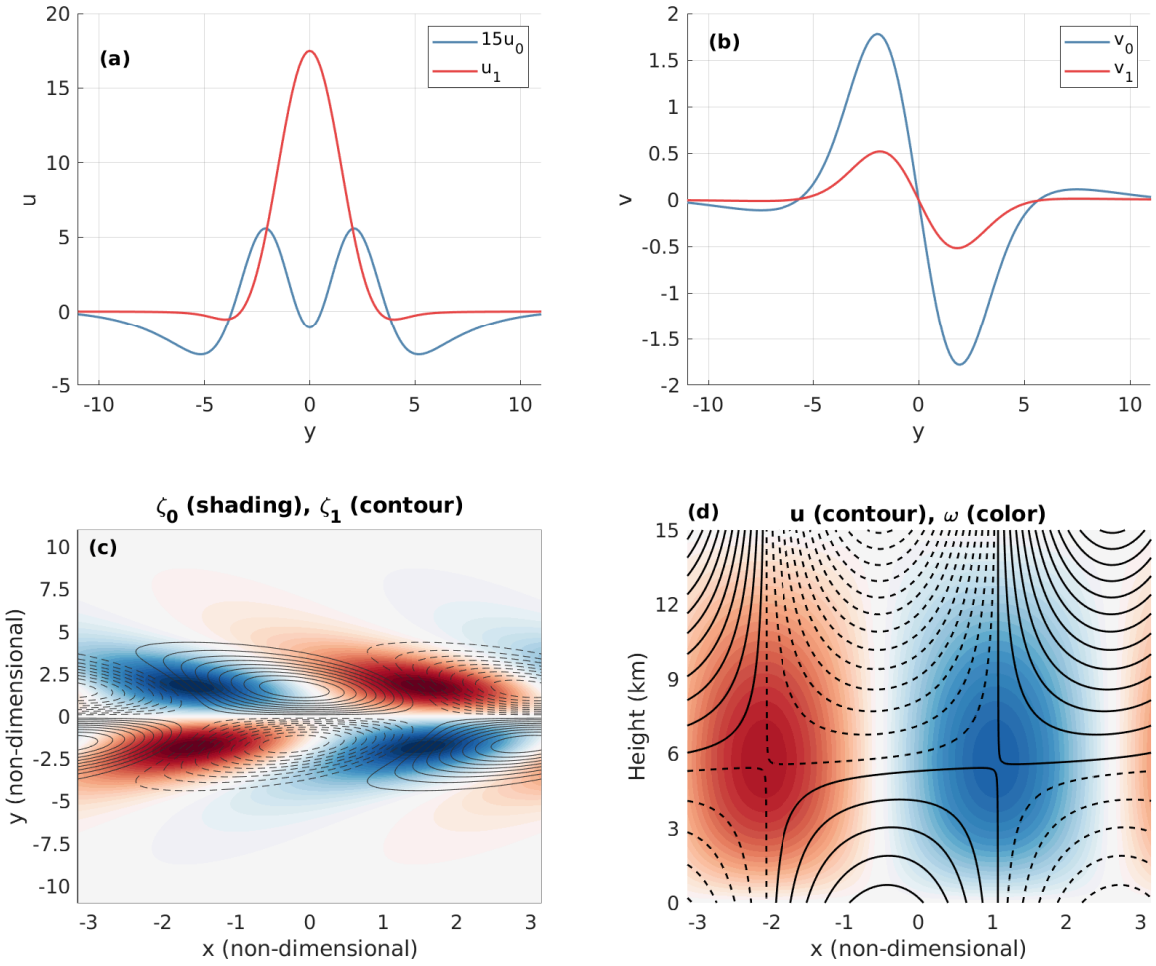

Figure 3-9: (a) Meridional structure of 15 times the barotropic zonal wind and the baroclinic zonal wind for the $n = -1$, $k = 1$ mode with $F = 0.25$ and the parameter set chosen in Figure 3-8. (b) Same as (a) but for the barotropic and baroclinic meridional wind. (c) Horizontal structure of the boundary layer (shading) barotropic vorticity and (contour) baroclinic vorticity. (d) Equatorial vertical cross sections of the (shading) pressure vertical velocity and (contours) zonal wind perturbations for the same mode. Solid (dashed) contours are positive (negative) zonal wind anomalies.

$n = -1$ modes. This is because the barotropic mode leads the baroclinic mode, as can also be seen in the horizontal structure of the boundary layer vorticity decomposition in Figure 3-9c.

Unfortunately the numerical model is quite unstable for the slow modes in the rigid-lid, surface friction limit. Despite strong sponge layers, instabilities unrelated to the slow modes (spurious noise, gravity waves) develop quickly in the numerical domain, precluding inferral of the complex growth rate and horizontal structure. The behavior of the barotropic mode in the slow modes will be discussed in the following section using the fully coupled, surface friction model, albeit with a large stratosphere stratification, instead of a rigid-lid.

These results show that surface friction act strictly as a damping mechanism in our framework, contrary to the results shown in Moskowitz and Bretherton (2000). This is likely because the convective heating associated with frictional convergence cannot “force" the system, as convection must be balanced by adiabatic cooling from large-scale subsidence and downdrafts that import low entropy mid-level air into the boundary layer. Surface friction does, however, act to modify both the horizontal and vertical structure of the equatorial waves, as shown through the long poleward tails of the barotropic mode and vertical tilt in the zonal wind fields.

3.3.3 Leaky, frictionally modified modes

While examining the excitation of the barotropic mode in the limits of surface friction under a rigid lid and a frictionless surface under a leaky lid were both useful exercises to isolate their respective effects on tropical waves, in the real world, both surface friction and leakage of energy to the stratosphere can act simultaneously to modify equatorial waves through excitation of the barotropic mode. In particular, the long-tails of the tropospherically trapped barotropic mode observed in the rigid-lid, surface friction model may behave differently if the barotropic mode can leak energy into the stratosphere.

To understand the extent to which both of these mechanisms can interact, we run the full troposphere-stratosphere numerical model with non-zero surface friction,

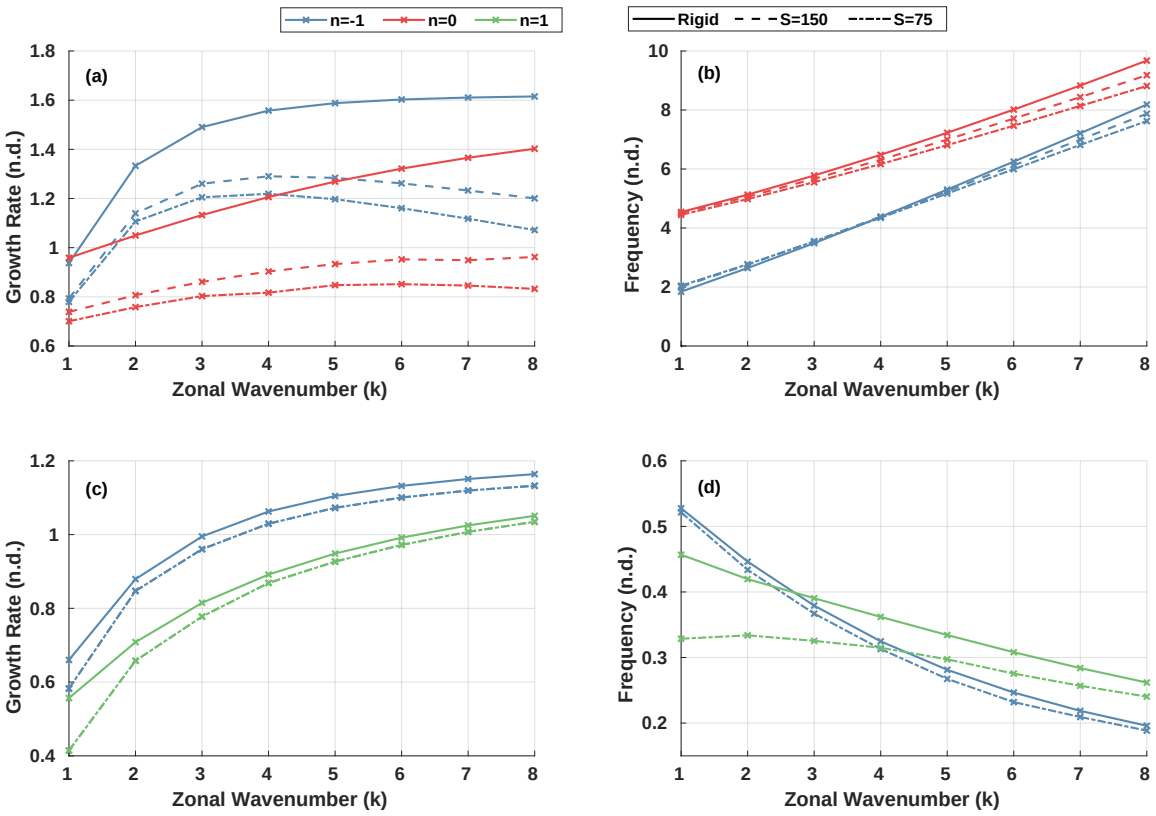

Figure 3-10: (a, c) Non-dimensional growth rate and (b, d) non-dimensional phase speed for the $n = -1, 0, 1$ modes of the (solid) rigid-lid system, the (dashed) surface friction + rigid-lid system with $S = 150$ and $F = 0.1$, and the (dot-dashed) surface friction + rigid-lid system with $S = 75$ and $F = 0.1$. Non-dimensional parameters selected for (a, b) are $\alpha = 3.5$, $\chi = 0.5$, $C = 0$, $\gamma = 1$, $D = 2.5$, $G = 0.25$, $\delta_x = 15$, and for (c, d) are $\alpha = 1$, $\chi = 1$, $C = 2.5$, $\gamma = 2$, $D = 1$, $G = 0.02$, $\delta_x = 30$. Only $S = 75$ case is shown for (c, d).

using the same methods to infer the complex growth rates and eigenmodes. We first examine their combined effect on the WISHE-driven classical Matsuno modes through the same parameter set as used in Figures 3-5 and 3-8. In addition, we focus on the eastward propagating modes since the westward propagating modes were not strongly affected by the presence of the stratosphere.

Figure 3-10a and Figure 3-10b show the non-dimensional growth rate and phase speeds for the WISHE destabilized Matsuno modes, respectively. Since there is both energy leakage into the stratosphere and surface friction, the growth rates are strongly dampened from the equivalent modes in the rigid-lid, inviscid limit. The frequencies of the WISHE Matsuno modes are not greatly modified, though all of the $n = 0$ modes

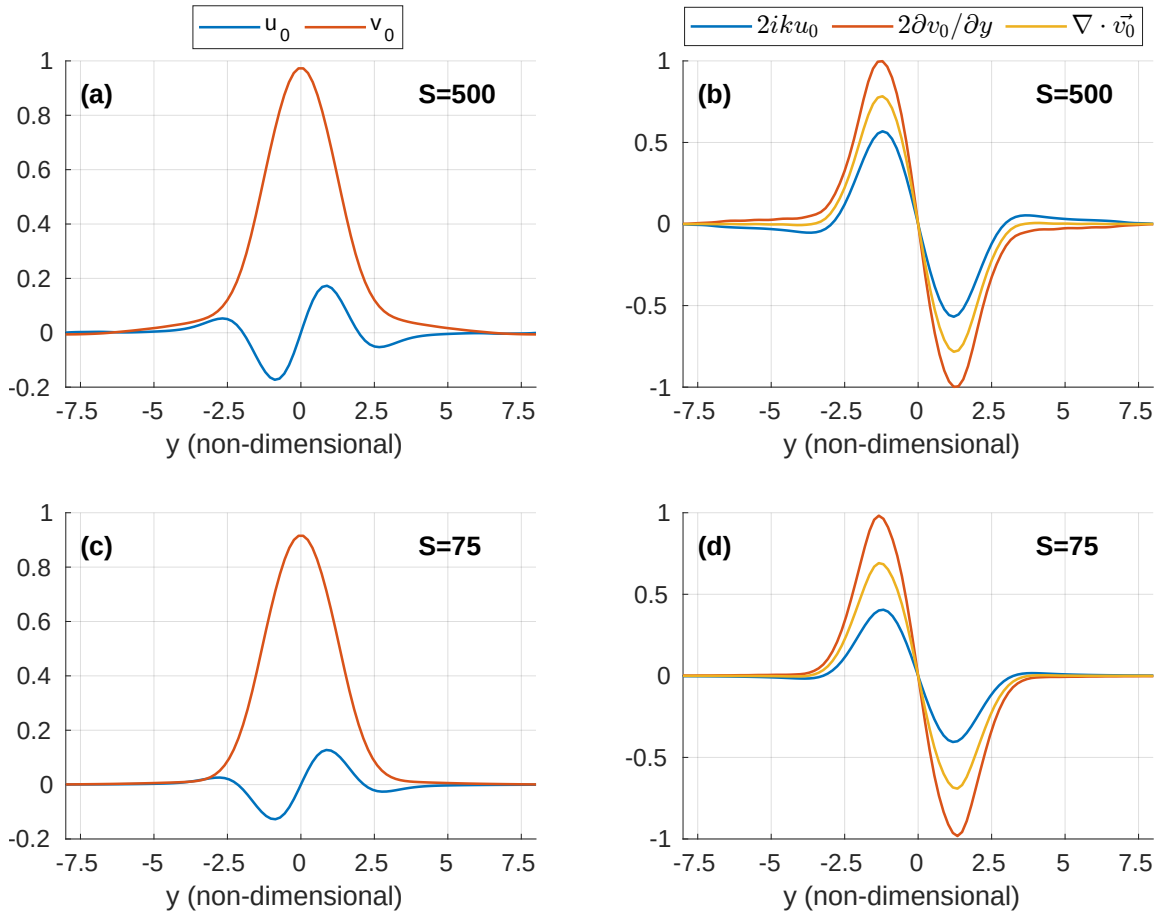

Figure 3-11: (a, c) Barotropic mode zonal and meridional velocities for the WISHE modified Matsuno $n = 0$, $k = 1$ mode using the same parameter set as in Figure 3-8, $\alpha = 3.5$, $\chi = 0.5$, $C = 0$, $\gamma = 1$, $D = 2.5$, $G = 0.25$, $\delta_x = 15$, $F = 0.1$, but with (a) $S = 500$ and (c) $S = 75$. (b, d) $2\frac{\partial u_0}{\partial x}$, $2\frac{\partial v_0}{\partial y}$ (scaled by 2) and $\nabla \cdot \vec{v_0}$ for the same mode but with (b) $S = 500$ and (d) $S = 75$.

and smaller scale $n = -1$ modes ($k \geq 5$) have slower phase speeds than their rigid-lid counterparts. Comparing with the growth rates in the stratosphere-only case shown in Figure 3-5, we can see that the damping effects of the stratosphere and surface friction are approximately additive.

The more interesting question, perhaps, is if the barotropic mode behaves differently when it can be excited by surface friction and also interact with the stratosphere. To examine this, we decompose the horizontal divergence of the barotropic mode into $\frac{\partial u}{\partial x}$, $\frac{\partial v}{\partial y}$, and the sum of both, which is equivalent to the pressure vertical velocity at the tropopause. Figure 3-11 shows the barotropic mode velocities and the barotropic

horizontal divergence decomposition for the $n = 0$, $k = 1$ WISHE Matsuno mode, for a realistic stratosphere stratification ($S = 75$), as well as a highly stratified one ($S = 500$). In the case with a highly stratified stratosphere, we see the long-tail feature of the barotropic mode velocities, as also seen in the surface friction under a rigid-lid model. However, a key differing feature is that the barotropic mode velocities are no longer completely non-divergent, as evidenced in Figure 3-11b. Further, the horizontal divergence of the barotropic mode (or, equivalently, the tropopause vertical velocity) decays to zero very quickly polewards, around $|y| = 3$. This is because near the equator, $\frac{\partial u_0}{\partial x}$ and $\frac{\partial v_0}{\partial y}$ have the same sign, evidence that the barotropic mode is exciting the stratosphere near the equator. In contrast, despite the barotropic velocities being small (though non-zero) polewards of the equator, the horizontal divergence is zero because $\frac{\partial u_0}{\partial x}$ and $\frac{\partial v_0}{\partial y}$ have opposite signs and almost exactly cancel. This is evidence of a tropospherically trapped barotropic mode. When we reduce the stratosphere stratification to $S = 75$, as shown in Figure 3-11c and Figure 3-11d, in effect allowing the tropopause to be more leaky, we see that the polewards extent of the barotropic mode velocities is greatly reduced, and hence the poleward extent of $\frac{\partial u_0}{\partial x}$ and $\frac{\partial v_0}{\partial y}$ is also reduced. The horizontal divergence still decays to zero around $|y| = 3$, as in the case where $S = 500$.

These numerical experiments illustrate the role the S plays in modulating the poleward extent of the barotropic mode. The mechanism can reasoned as the following: under infinite stratification, (the rigid lid), surface friction allows for the excitement of the barotropic mode far away from the equator, as shown earlier. As the stratification of the stratosphere is decreased, more wave energy escapes into the stratosphere, reducing the poleward extent of the barotropic mode. Despite the unrealistically large stratification ($S = 500$) used to emphasize the characteristics of the trapped barotropic mode, the qualitative behavior of the model does not change with intermediate stratifications (not shown). In other words, the poleward extent of the tropospherically trapped barotropic mode increases with S.

Figure 3-10c and Figure 3-10d show the non-dimensional growth rate and phase speeds for the slow modes, for which we obtain by choosing the same parameter set as

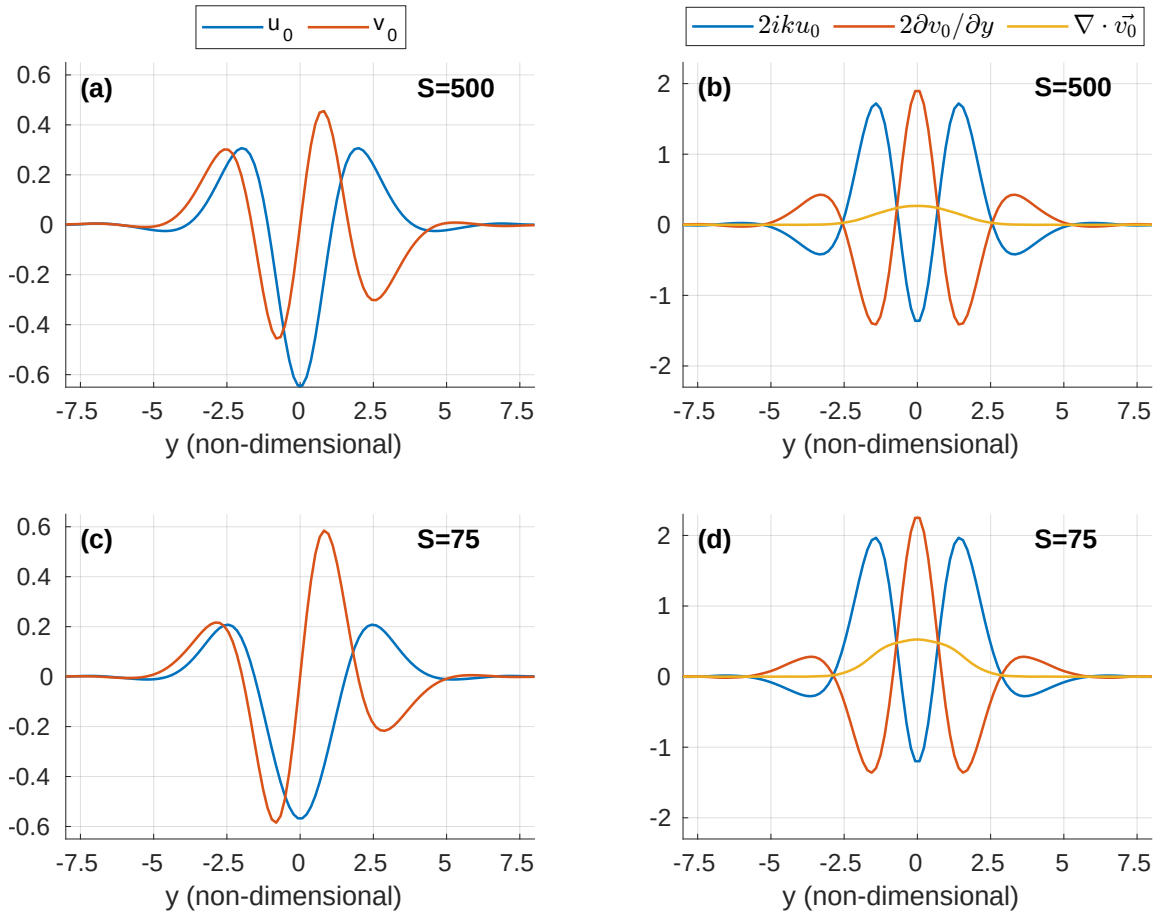

Figure 3-12: Analogous to Figure 3-11 but for the slow propagating $n = 1$, $k = 2$ mode using the parameter set $\alpha = 1$, $\chi = 1$, $C = 2.5$, $\gamma = 2$, $D = 1$, $G = 0.02$, $\delta_x = 30$, $F = 0.1$.

used in Figure 3-3 and 3-6. Note, the $n = 0$ waves do not grow in time. The growth rates are not modified greatly from the rigid lid solutions; surface friction seems to have a weaker damping effect on the slower propagating modes. The damping effect of the stratosphere on the growth rates is small but the greatest at the largest scales, and almost negligible for the smaller scale waves, as before. However, the frequencies/phase speeds for the slow modes are reduced, by as much as 30% for the $k = 1$ wave. The damping of the frequency is much greater for the $n = 1$ slow propagating modes than the $n = -1$ modes, and much stronger for larger scale $n = 1$ waves. It is also worth noting that the $S = 150$ case is not shown for the slow modes since the lines are nearly indistinguishable from the $S = 75$ case.

The behavior of the poleward extent of the barotropic mode for the slow modes is

similar to that for the WISHE-modified Matsuno modes. Figure 3-12 shows that the barotropic mode associated with the $n = 1$, $k = 2$ slow mode becomes non-divergent away from the equator and trapped in the troposphere. However, one key difference is that the slow modes do not leak much energy into the stratosphere to begin with, and thus decreasing the stratosphere stratification does not completely eliminate the long-tailed behavior of the barotropic velocities. This is evidenced by the small magnitude of the horizontal divergence of the barotropic mode (Figure 3-12b, Figure 3-12d), regardless of the stratosphere stratification, as iku_0 and $\frac{\partial v_0}{\partial y}$ nearly cancel close to the equator ($|y| < 3$), and exactly cancel for $|y| > 3$.

What are the physical parameters that control the non-dimensional stratosphere stratification, S, and how can they vary across different equatorial waves? The non-dimensionalization of S [see Appendix B] suggests that the stratosphere buoyancy frequency, N^2 and the meridional length scale, L_y, are quantities that could potentially lead to large variations in S. L_y depends on a multitude of factors that can vary greatly in the tropics, such as the troposphere dry stratification, moist adiabatic lapse rate, and the precipitation efficiency. The largest influencing factor, however, is the precipitation efficiency, ϵ_p: waves with larger ϵ_p experience a much greater stratosphere stratification. For instance, for Earth-like parameters and a $\epsilon_p = 0.5$, $S \approx 20$, while for $\epsilon_p = 0.95$, $S \approx 200$, an order of magnitude difference. While our definition of ϵ_p is an egregiously simple parameterization of cloud microphysics, the impact of ϵ_p on S links cloud microphysical properties to the behavior of the barotropic mode.

3.4 Discussion and summary

In this study, we extended a previously developed linear framework to include two mechanisms that can excite the barotropic mode in equatorial waves, surface friction, and coupling to the stratosphere. We first analyzed the modification of equatorial waves in the two separate limits of (1) coupling to the stratosphere with an inviscid surface, and (2) surface friction under a rigid-lid. Using a combination of theoretical solutions for the $v = 0$ mode and numerical solutions for higher order meridional

modes, we found that the presence of a stratosphere leads to upward wave energy propagation that strongly dampens the growth rate of smaller-scale waves. This effect is consistent across the WISHE-modified Matsuno modes explored in this study, though it does not appreciably affect the slow propagating modes that are destabilized from cloud-radiative feedbacks. The barotropic mode is found to lead the baroclinic mode for the $n = -1$ eastward propagating modes, leading to a slight eastward tilt in the vertical that arises from the superposition of the two modes. The eastward tilt was found to be robust across horizontal scales and stratosphere stratification. In the limit of surface friction under a rigid-lid, we found that surface friction acts only to dampen growth rates by nearly a constant across all waves and zonal wavenumbers, which is reasonable given that surface friction acts on a constant time scale of damping in our framework. We also found that frictional excitation of the barotropic mode leads to long tails of non-divergent barotropic zonal and meridional velocities away from the equator. The barotropic mode is also found to lead the baroclinic mode for the $n = -1$ eastward propagating modes, leading to a vertical tilt in the zonal wind field, but not the vertical velocity field since the barotropic mode is non-divergent under a rigid lid.

The combined effects of surface friction and coupling to the stratosphere were analyzed using numerical solutions of the full linear model. We found that for the growth rates of the waves, the damping effects of surface friction and coupling to the stratosphere were approximately additive. Under a large non-dimensional stratosphere stratification, both the WISHE-modified Matsuno modes and slow modes exhibit tropospherically trapped barotropic modes away from the equator. Thus, the non-divergent barotropic velocities extend far away from the equator and are small but non-zero. When the non-dimensional stratosphere stratification is reduced, the poleward extent of the barotropic mode is greatly reduced. These results indicate that the dimensional variables that influence the non-dimensional stratosphere stratification, such as the buoyancy frequency in the stratosphere and precipitation efficiency, play key roles in modulating the poleward extent of the barotropic mode. While this study was restricted to theoretical analysis of the barotropic mode, future work will

attempt to find evidence of the barotropic mode in both observational and numerical data.

This work models the interaction of equatorial waves with a zero mean flow stratosphere, and is the first basic step to illuminate how a dynamically dry and passive fluid influences the dynamics of a moist and convecting fluid underneath. Extension of the framework developed in this study to a non-zero mean flow in the stratosphere will be the subject of future work, which would allow for an investigation into the extent to which upwards wave radiation can explain the observed relationship between the MJO and Quasi-Biennial Oscillation (QBO) (Yoo and Son, 2016).

Finally, it is worth discussing some of the short-comings of the modeling framework. Our application of surface friction in an infinitesimally small boundary layer with zero vertical velocity is exceptionally crude compared to real-world frictional boundary layers. In addition, the strict-quasi equilibrium approximation may not be as accurate for extremely short or high frequency waves (Ahmed et al., 2021), as evidenced by the presence of what looks like a second baroclinic mode in observations of convectively coupled Kelvin waves (Straub and Kiladis, 2002). Regardless, both surface friction and upward radiation of wave energy are shown to important mechanisms that influence the horizontal structure, vertical structure, and growth rates of equatorial waves, through excitation of the barotropic mode.

Chapter 4

Stratospheric Modulation of the MJO in a Linear Model: Upward Wave Radiation and Cirrus Cloud Feedbacks

Abstract

Recent observations have indicated significant modulation of the Madden Julian Oscillation (MJO) by the phase of the stratospheric Quasi-Biennial Oscillation (QBO) during boreal winter. This study extends the previously developed theoretical linear model of Lin and Emanuel (2022) to investigate how modulation of upward wave propagation and cloud radiative feedbacks allows the phase of the QBO to influence the strength of the MJO. As previous studies using the same theoretical model have shown, a slow, eastward propagating mode that strongly resembles the MJO appears with interactive cloud-radiation. In particular, troposphere-stratosphere interactions in the linear model are modeled by modifying the model to include a mean wind in the stratosphere. A simple prognostic equation for high clouds, in which two processes, (1) zonal advection and (2) dynamical modulation by upward propagating waves, is also included. It is shown that shear in the mean zonal wind across the tropopause controls the phase relationship between the barotropic and baroclinic modes, modulating the surface flux feedback, though questions about realism of the mechanism are discussed. It is also shown that under linear dynamics, the upward energy flux and subsequent damping of the MJO are larger under stratospheric easterlies than westerlies because of increased vertical group velocity of the Kelvin wave mode. While this

result can be qualitatively explained through simple linear theory, it is opposite the observed relationship between MJO strength and the phase of QBO. Conversely, dynamical modulation of high cirrus clouds from upward propagating waves and zonal advection of high clouds are shown to lead to damping of the MJO under QBO westerlies, which is consistent with the observed relationship. Implications, caveats, and limitations of the linear theory are discussed, particularly with respect to the seasonality of the QBO-MJO relationship.

4.1 Introduction

The MJO is a distinct eastward propagating planetary scale oscillation in the tropics that has a period of around 30-90 days, and is the dominant mode of intraseasonal variability in the tropics (Zhang, 2005). Through teleconnections, the MJO also plays a significant role in altering extratropical circulations (Matthews et al., 2004). As such, the MJO has been considered the "holy grail" of tropical dynamics (Raymond, 2001). Though the MJO is the largest source of seasonal and sub seasonal predictability in the atmosphere (Hendon et al., 2000; Vitart et al., 2017), modern MJO prediction skill lags estimates of its predictability (Neena et al., 2014), indicating a gap in our knowledge of the dynamics of the MJO. Much progress has nevertheless been made on understanding the drivers of the MJO ever since the discovery of the MJO during the early 1970s (Madden and Julian, 1971). Most recently, simple theoretical models (Sobel and Maloney, 2013; Adames and Kim, 2016) and idealized modeling studies (Crueger and Stevens, 2015; Khairoutdinov and Emanuel, 2018) have suggested that cloud-radiative feedbacks are essential to destabilizing the MJO.

Recent studies have uncovered a link between the strength of the MJO and the phase of the Quasi Biennial Oscillation (QBO), a stratospheric mode of variability in which the lower stratospheric zonal winds shift between easterlies and westerlies approximately every 28 months (Baldwin et al., 2001), throwing another wrench into the MJO problem. The MJO has been observed to be much stronger during the easterly phase of the QBO than the westerly phase of the QBO, but only during boreal winter (Yoo and Son, 2016; Son et al., 2017). This link has downstream ramifications that are vital; research has shown that the predictability of the MJO is

around a week longer during easterly QBO phases than during westerly QBO phases (Marshall et al., 2017). As a result, sub-seasonal to seasonal forecast models all show enhanced MJO prediction skill during easterly QBO winters (Wang et al., 2019; Lim et al., 2019). Thus, understanding the physical mechanism through which the QBO can modulate the MJO could help extend the predictability of sub-seasonal forecasts in the tropics, advance modeling of teleconnections between the tropics and extratropics, and improve predictions of global climate.

Several mechanisms have been proposed to explain how the mean state of the stratosphere can so strongly influence the strength of a tropospheric phenomenon in the MJO. Since the QBO is associated with vertical wind shear of the zonal wind, thermal wind balance necessitates temperature anomalies in the tropopause transition layer (TTL) (Baldwin et al., 2001; Fueglistaler et al., 2009). One branch of proposed mechanisms contends that during easterly QBO phases, cold anomalies induced by adiabatic cooling destabilize the TTL, invigorating deep convection associated with the MJO (Son et al., 2017; Klotzbach et al., 2019; Abhik and Hendon, 2019). However, tropospheric temperature anomalies associated with the QBO are less than 0.5 K in boreal winter (Martin et al., 2021b), and climate models with realistic QBO temperature signals fail to capture the QBO-MJO relationship (Martin et al., 2021a). Other studies have proposed that the QBO modulates the production of thin cirrus clouds near the tropopause, through mean-state changes in the temperature and stratification in the TTL (Sakaeda et al., 2020).

One relatively untested idea is how the QBO can modulate tropospheric energy loss to the stratosphere via upward wave propagation, since the extent to which tropospheric waves can propagate upwards can be strongly dependent on the sign of the zonal wind in the stratosphere (Charney and Drazin, 1961; Andrews et al., 1987). Since the MJO projects strongly onto both equatorial Kelvin and Rossby waves (Hendon and Salby, 1994), it would be prudent to understand how the loss of wave energy to the stratosphere can dampen certain modes in the troposphere. As Charney and Drazin (1961) showed, the upward propagation of tropospheric extratropical Rossby waves is non-linearly dependent on the sign and strength of zonal flow: under east-

erly or strong westerly flow, Rossby waves are trapped in the troposphere. A similar effect holds in the tropics, where Rossby waves can only propagate upwards in regions of westerly or weak easterly flows (Andrews et al., 1987). Kelvin waves exhibit the opposite, where they can only propagate in regions of easterly or weak westerly winds. Indeed, there is evidence in re-analysis data that Rossby waves are trapped in the troposphere during easterly phases of the QBO, and leak into the stratosphere during westerly phases of the QBO; conversely, Kelvin waves have been found to radiate more energy into the stratosphere during easterly lower stratosphere winds (Yang et al., 2012). It might be plausible, then, that the MJO could be dampened through the loss of wave energy to the stratosphere, if the increased upward wave energy flux from Rossby waves offsets the decreased upward energy flux from Kelvin waves during westerly QBO phases. Significant upward propagation of equatorial Rossby waves is only observed during boreal winter (Yang et al., 2012), which may explain the fact that the QBO-MJO relationship is significant only in boreal winter, though this may also be related to increased equatorward (and upward) propagating extra-tropical Rossby waves at the same time.

There is also some evidence that the production efficiency of high clouds may be modulated by the phase of the QBO, at least on interannual (Davis et al., 2013) and seasonal (Tseng and Fu, 2017) timescales, since easterly QBO phases are associated with cold anomalies near the tropopause. However, analysis of observational data from the polar-orbiting CALIPSO satellite (Winker et al., 2009) suggests only around a 5% difference in near-tropopause cirrus cloud frequency between easterly and westerly phases of the QBO, though the data are generally too sparse in space and time to provide significant evidence (Son et al., 2017). Furthermore, the QBO does not seem to significantly modulate the activity of other convectively coupled equatorial waves (CCEWs), which may suggest that modulation of cirrus clouds by the QBO is not a significant process (Abhik et al., 2019). This, however, could be mitigated by the fact that CCEWs have a much weaker cloud-radiative feedback than the MJO (Sakaeda et al., 2020). More importantly, composites of ice clouds associated with the equatorial component of the MJO show an eastward tilt with height

in cloud fraction near the stratosphere (Virts and Wallace, 2010). This eastward tilt near the stratosphere could be the result of (1) advection of ice clouds by westerly zonal wind, or (2) dynamical upward propagating Kelvin wave portion of the MJO. On the former point, zonal winds associated with the QBO during boreal winter are small but non-zero [1-3 m/s] in the TTL (Son et al., 2017). Differential advection of cirrus clouds by the mean flow could modulate the phase relationship of radiative heating with tropospheric convection, influencing the strength and propagation speed of the MJO. On the latter point, analysis of satellite observations of temperature and cirrus clouds showed that MJO convection was associated with large-scale Kelvin and Rossby wave activity in the TTL, and that the large-scale ascent associated with these waves produced cold anomalies in the TTL and hence greater levels of cirrus clouds (Virts and Wallace, 2014). These results are qualitatively consistent with radiosonde data that show a link between cirrus cloud formation and large-scale vertical motion by upward propagating waves (Boehm and Verlinde, 2000). Hence, the efficiency of cirrus cloud formation could be modulated by the cold phases of upward propagating equatorial waves.

In general, modeling studies on the MJO-QBO link have been particularly limited, since the MJO is notoriously difficult to simulate correctly in a GCM (general circulation model) (Hung et al., 2013). An investigation into the MJO-QBO relationship using a nudged GCM was not successful in replicating the observed relationship between the MJO and QBO (Martin et al., 2021a). Studies on this topic have mostly been confined to analysis on observations, re-analysis, and GCMs, while idealized theoretical models have not yet been used to provide insight into the observed relationship between the MJO and QBO.

The primary purpose of this study is to investigate the relationship between the MJO and QBO by using an idealized, linear model that can represent cloud radiative feedbacks and tropospheric energy loss via upward wave propagation. The model must have some representation of the MJO and also be coupled to a representation of the stratosphere. Khairoutdinov and Emanuel (2018) and Emanuel (2020) developed a strict quasi-equilibrium tropospheric theoretical model and showed that slow, MJO-

like modes appear as solutions when cloud-radiative feedbacks are active. Lin and Emanuel (2022) extended the linear model by coupling a dry, passive stratosphere on top of the quasi-equilibrium troposphere, and evaluated the effect of upward wave radiation on equatorial waves, though in the context of a zero-mean zonal wind in the stratosphere. We further extend the work of Lin and Emanuel (2022) by formulating the model for a non-zero zonal wind in the stratosphere, and include an additional prognostic equation for cirrus clouds, which are allowed to modify the perturbation radiative heating in the troposphere.

The paper is organized as follows. Data used in this study to motivate the linear model is described in section 4.2. Section 4.3 formulates the linear model. Section 4.4 presents the solutions of the linear model under varying cases. The paper concludes with a discussion and summary in section 4.5.

4.2 Data

While this study formulates a theoretical linear model to understand stratospheric influences on the MJO, a few observational data sources are used to facilitate formulation of the linear model. First, monthly data regarding zonal wind climatology is taken from ERA5 re-analysis fields developed by the European Center for Medium-Range Weather Forecasts (ECMWF), from 1979-2020 (Hersbach et al., 2020). These data are used in particular to define the QBO, and examine tropopause transition layer wind anomalies during different QBO phases. In this study, the QBO is defined using the zonal-mean zonal wind at 50-hPa, averaged over the tropics (10°S-10°N); the QBO is said to be in its easterly phase (QBOE) when the zonal-mean zonal wind is smaller than -0.5 standard deviations from the mean, and in its westerly phase (QBOW) when the zonal-mean zonal wind is greater than 0.5 standard deviations from the mean, as in Son et al. (2017). ERA5 re-analysis is publically available through the Climate Data Store of the Copernicus Climate Change Service.

The phase and amplitude of the MJO are defined using the monthly-averaged OLR MJO Index (OMI), as defined in Kiladis et al. (2014). The OMI index is

defined purely based on satellite observations of outgoing longwave radiation (OLR). This is different from the Realtime-Multivariate MJO (RMM) index, which is defined by the two leading principal components (RMM1 and RMM2) of a combination of the equatorially averaged upper (200-hPa) and lower level (850-hPa) zonal winds, and satellite observations of outgoing longwave radiation (OLR). The phase of the MJO is defined in the phase space of RMM1 and RMM2, following the convention of Wheeler and Hendon (2004), with PC2 of OMI being analogous to RMM1, and -PC1 of OMI being analagous to RMM2 Kiladis et al. (2014). The amplitude of the MJO is defined as the magnitude of the monthly-averaged OMI vector, or ($\sqrt{[\text{OMI1}]^2 + [\text{OMI2}]^2}$). The OMI index is available online at `https://psl.noaa.gov/mjo/mjoindex/omi.1x.txt`.

Observations of ice and water cloud fractions are taken from 2007-2017 Level 3 cloud occurrence products made by the CALIOP instrument aboard the polar orbiting CALIPSO satellite. Level 3 products are gridded and aggregated monthly, with a vertical resolution of 60 m. Cloud fraction anomalies are deseasonalized and accumulated over nonoverlapping boxes of width 10° longitude and 5° latitude. THe CALIOP data is available at `https://asdc.larc.nasa.gov/project/CALIPSO/CAL_LID_L3_Cloud_Occurrence-Standard-V1-00_V1-00`.

4.3 Linear model

4.3.1 Tropospheric equations

Here, we summarize the tropospheric equations of the linear model formulated in Lin and Emanuel (2022), except in the case where surface friction is set to zero ($F = 0$). In particular, Lin and Emanuel (2022) removed the rigid-lid in the tropospheric

equations, which allows the barotropic mode to be excited in a linear model:

$$\frac{\partial u_0}{\partial t} = -\frac{\partial \phi_0}{\partial x} + y v_0 \tag{4.1}$$

$$\frac{1}{\delta_x}\frac{\partial v_0}{\partial t} = -\frac{\partial \phi_0}{\partial y} - y u_0 \tag{4.2}$$

$$\frac{\partial u_1}{\partial t} = \frac{\partial s}{\partial x} + y v_1 \tag{4.3}$$

$$\frac{1}{\delta_x}\frac{\partial v_1}{\partial t} = \frac{\partial s^*}{\partial y} - y u_1 \tag{4.4}$$

$$\frac{\partial s}{\partial t} = (1 + C)s_m - w - \alpha u_b - \chi s \tag{4.5}$$

$$\gamma\frac{\partial s_m}{\partial t} = -Ds - \alpha u_b - Gw + Cs_m \tag{4.6}$$

where u_0 and v_0 are the barotropic zonal and meridional winds, u_1 and v_1 are the baroclinic zonal and meridional winds, ϕ_0 is the barotropic geopotential, δ_x is a non-dimensional coefficient representing the magnitude of zonal geostrophy, s is the saturation moist entropy, s_m is the characteristic mid-level moist entropy of the free troposphere, w is the bulk tropospheric vertical velocity, u_b is the boundary layer zonal wind (equal to $u_0 + u_1$), χ is a non-dimensional entropy damping coefficient, γ is a non-dimensional tropospheric entropy time scale, D is a non-dimensional entropy damping coefficient, α is the wind-induced surface heat exchange (WISHE) feedback parameter, and G is the gross moist stability. The equations are completed with mass continuity in the troposphere in pressure coordinates. Note that in these equations, the radiative heating perturbation is parameterized as $Q = Cs_m$, which is evident in Equations (4.5) and (4.6). This is important, since Emanuel (2020) showed that when C is non-zero and large enough, slow propagating modes that are MJO-like appear as fastest growing modes. The reader is referred to Lin and Emanuel (2022) for additional details in derivation and interpretation of Equations (4.1) - (4.6), which are incomplete without governing equations for the stratosphere. Modifications to the stratospheric equations are discussed in the following sections.

4.3.2 Non-zero stratospheric mean wind

To include vertical wind shear across the tropopause, we must modify the stratospheric equations formulated in Lin and Emanuel (2022). The non-dimensional vertical velocity at the tropopause can be inferred by integrating the mass continuity equation upwards from the surface.

$$\omega(y, \hat{p}_t) = \frac{\partial u_0}{\partial x} + \frac{\partial v_0}{\partial y} \tag{4.7}$$

where u_0 and v_0 are the barotropic velocities ω is the pressure vertical velocity, and $\hat{p}_t$ is the non-dimensional tropopause pressure. Note the baroclinic velocities do not enter here since the vertical integral of the first-baroclinic mode is zero.

Next, we assume that the mean wind in the stratosphere is non-zero and varies in the vertical:

$$u_s(x, y, z^*, t) = \overline{U}_s(z^*) + u'_s(x, y, z^*, t) \tag{4.8}$$

where z^* is the log-pressure coordinate. For simplicity, the time scale of the mean stratopheric wind is assumed to be much longer than that of the tropospheric wave, and thus the mean wind is assumed to be constant in time. After dropping primes for perturbation quantities and using the additional non-dimensionalization of the mean zonal wind:

$$\overline{U}_s \to \beta L_y^2 U_s \tag{4.9}$$

the linearized, non-dimensional zonal momentum equations in log-pressure coordinates of the stratosphere are:

$$\frac{\partial u_s}{\partial t} + \overline{U}_s \frac{\partial u_s}{\partial x} = -\frac{\partial \phi_s}{\partial x} + yv \tag{4.10}$$

$$\frac{1}{\delta_x}\Big(\frac{\partial v_s}{\partial t} + \overline{U}_s \frac{\partial v_s}{\partial x}\Big) = -\frac{\partial \phi_s}{\partial y} - yu \tag{4.11}$$

where subscripts of s indicate stratospheric variables, L_y is the meridional length scale defined in Khairoutdinov and Emanuel (2018), and β is the meridional gradient of the Coriolis force. Typical peak zonal wind anomalies at 50-hPa are on the order

of 20 m s^{-1} during QBOE and 15 m s^{-1} during QBOW (Baldwin et al., 2001), which yields an approximate range of the non-dimensional mean wind as $\overline{U}_s \approx [-0.75, 0.5]$.

The mass continuity equation in the stratosphere does not change, though it is provided for completeness:

$$\frac{\partial}{\partial x}u_s + \frac{\partial}{\partial y}v_s + \frac{1}{\rho_0}\frac{\partial}{\partial z}\Big(\rho_0 w_s^*\Big) = 0 \tag{4.12}$$

where w_s^* is the log-pressure vertical velocity, $z^* = 1$ is defined as the tropopause (lower boundary), and $\rho_0(z^*) = \exp(\alpha_H(1 - z^*))$ is a non-dimensional density that decays with a non-dimensional scale height α_H. With the approximation that the vertical wavelength of the mode of interest is much smaller than α_H, Equation (4.12) can be integrated from the lower boundary in z^*, to obtain:

$$w^*(y, z^*) = w^*(y, z^* = 1) - \int_{z=1}^{z} \Big[\Big(iku(y, z^*) + \frac{\partial}{\partial y}v(y, z^*)\Big)\Big]dz \tag{4.13}$$

where $w^*(z^* = 1)$ is coupled to the vertical velocity at the tropopause in the troposphere equations and will be calculated from the matching conditions.

The first matching condition is continuity of normal displacement across the interface (in dimensional notation):

$$w = \frac{D\eta}{Dt} \tag{4.14}$$

where η is the displacement at the tropopause. Since there is now an assumed zonal mean flow, the coupling condition changes from that formulated in Lin and Emanuel (2022). Linearizing under a zonal mean flow $\overline{U}$, we obtain:

$$\frac{\partial \eta}{\partial t} + \overline{U}\frac{\partial \eta}{\partial x} = w \tag{4.15}$$

After non-dimensionalizing with the notation:

$$\eta \rightarrow \frac{aC_k|V|}{\beta L_y^2}\eta \tag{4.16}$$

where a is the radius of the Earth, C_k is the enthalpy flux coefficient, $|V|$ is the magnitude of the surface winds, we obtain the relation between the vertical velocities in the various vertical coordinates:

$$w_s(\hat{p} = \hat{p}_t) = \frac{T_t}{\overline{T}_s} w_s^*(z^* = 1) \tag{4.17}$$

$$w_t(\hat{p} = \hat{p}_t) = -\frac{R_d T_t}{gH} \frac{\hat{p}_s - \hat{p}_t}{\hat{p}_t} \omega(\hat{p} = \hat{p}_t) \tag{4.18}$$

where T_t is the tropopause temperature, $\hat{p}_s$ is the non-dimensional surface pressure, $\overline{T}_s$ is the mean temperature in the stratosphere, R_d is the dry gas constant, g is the acceleration of gravity, and H is the tropopause height. Applying Equations (4.17) and (4.18) to Equation (4.15) yields:

$$\frac{\partial \eta}{\partial t} + ik\eta \overline{U}_s(z^* = 1) = \frac{T_t}{\overline{T}_s} w_s^*(z^* = 1) \tag{4.19}$$

$$\frac{\partial \eta}{\partial t} = -B\Big(iku_0 + \frac{\partial v_0}{\partial y}\Big) \tag{4.20}$$

where $B = \frac{R_d T_t}{gH} \frac{p_s - p_t}{p_t}$ and we assume no mean zonal flow in the troposphere. Note this assumes a jump in mean zonal wind at the tropopause, which also introduces a jump in the velocities of the solutions. Since we do not know the complex growth rate a-priori, we formulate the system in terms of linear, non-dimensional prognostic equations that will be solved by a numerical model:

$$\frac{\partial \eta}{\partial t} = -B\Big(iku_0 + \frac{\partial v_0}{\partial y}\Big) \tag{4.21}$$

$$w^*(z^* = 1) = \frac{\partial \eta}{\partial t} + ik\eta \overline{U}_s(z^* = 1) \tag{4.22}$$

Given the barotropic mode velocities, we can calculate the local interface displacement rate using Equation (4.21). The local interface displacement rate and the interface displacement then can be used to calculate the vertical velocity at the tropopause (in the stratosphere) using Equation (4.22). The tropopause vertical velocity in the stratosphere is then used as the lower boundary condition in Equation (4.13). Note that when $\overline{U}_s = 0$, the conditions simplify to continuity of vertical velocity at the

tropopause, as in Lin and Emanuel (2022).

4.3.3 Thermal wind balance

The stratospheric equation set is not yet complete, as we have yet to formulate the temperature equation in the stratosphere. As is observed in the real-atmosphere, QBO-associated vertical gradients in mean zonal wind must be associated with meridional gradients in temperature, according to thermal wind balance (Baldwin et al., 2001). For an equatorial β-plane, thermal wind balance is expressed as [see equation 8.2.1 in Andrews et al. (1987)]:

$$\frac{\partial u_s}{\partial z} = -\frac{R_d}{\beta H_s y}\frac{\partial T}{\partial y} \tag{4.23}$$

where H_s is the scale height in the stratosphere. Non-dimensionalizing temperature with:

$$T \rightarrow \frac{\beta^2 L_y^4}{R_d} T \tag{4.24}$$

yields:

$$\frac{\partial \overline{U}_s}{\partial z} = -\frac{H}{H_s}\frac{1}{y}\frac{\partial \overline{T}}{\partial y} \tag{4.25}$$

for the mean-state field. Non-dimensionalizing similarly in the hydrostatic equation yields:

$$\frac{\partial \phi_s}{\partial z^*} = \xi T \tag{4.26}$$

where for a scale height of $H_s = 7$ km and $H = 16$ km, $\xi = \frac{H^2 \beta L_y^2}{H_s a C_k |V|} \approx 70$. Note that the vertical shear in the zonal mean wind associated with the QBO can be large on the equator, yielding temperature gradients around 4 K (Baldwin et al., 2001). This may impact the thermodynamics and dynamics equatorial waves in the stratosphere. To incoporate this into the linear model, we start with the dimensional temperature equation (including hydrostatic balance), which is:

$$\left(\frac{\partial}{\partial t} + \vec{V} \cdot \boldsymbol{\nabla}\right)\frac{\partial \phi_s}{\partial z^*} + w_s^* N^2 = 0 \tag{4.27}$$

The squared buoyancy frequency in log-pressure coordinates is:

$$N^2 \equiv \frac{R_d}{H_s}\Big(\frac{\partial T}{\partial z^*} + \kappa\frac{T}{H_s}\Big) \tag{4.28}$$

where $\kappa = R_d/c_p \approx 2/7$. QBO contributions to the mean-state stratification are small: a 3 K perturbation over 5 km yields an perturbation buoyancy frequency of $[N^2]' \approx 3 \times 10^{-5}\ s^{-2}$, which is more than an order of magnitude smaller than the buoyancy frequency of the stratosphere, $N^2 \approx 5 \times 10^{-4}\ s^{-2}$. Thus, we approximate N^2 as constant. Linearizing the temperature equation under non-zero zonal flow in thermal wind balance yields:

$$\frac{\partial}{\partial t}\frac{\partial \phi_s'}{\partial z^*} + \overline{U}_s(y,z)\frac{\partial^2 \phi_s'}{\partial x\,\partial z^*} + v'\frac{\partial^2 \overline{\phi}_s}{\partial y\,\partial z^*} + w_s^{*\prime}N^2 = 0 \tag{4.29}$$

Non-dimensionalizing Equation (4.29) and dropping primes for perturbation quantities yields:

$$\frac{\partial}{\partial t}\frac{\partial \phi_s}{\partial z^*} + \overline{U}_s(y,z)\frac{\partial^2 \phi_s}{\partial x\,\partial z^*} + \frac{\xi}{\gamma_v}\frac{\partial \overline{T}}{\partial y}v + w_s^* S = 0 \tag{4.30}$$

where $\gamma_v = \frac{H\beta L_y^2}{C_k|V|a} \approx 30$, such that $\xi/\gamma_v \approx 2.5$, which will be used for the rest of the study. Although meridional temperature gradients associated with the QBO can be large on the equator (≈ 4 K), the magnitude of the QBO-associated temperature anomalies decay quite quickly away from the equator. The opposite is true for meridional velocities: they can be large off the equator (especially in the Rossby gyres associated with the MJO), but are typically small near the equator. We confirmed in our experiments that for the MJO-like mode that appears in the linear model, the dominant terms in Equation (4.30) are the zonal and vertical advection (the second and fourth terms on the left hand side, respectively.

Next, we implement a wave-radiation condition through Equation (4.30). As in Lin and Emanuel (2022), it is not necessary that w^* goes to zero as $z \to \infty$: as long as the energy density (ρw^{*2}) goes to zero, then wave energy is forced to be propagating upwards from the troposphere. However, we include strong sponge layers at the boundaries of the numerical domain to ensure that the velocities do go to zero at

the edges. Note that this precludes excitation of the stratospheric barotropic mode, which is an important detail that will be discussed later. Integrating Equation (4.30) while ignoring meridional advection, from the upper boundary and assuming a zero upper boundary condition yields:

$$\frac{\partial \phi_s}{\partial t} = -ik \int_{\infty}^{z} \overline{U}_s(y,z) \frac{\partial^2 \phi_s}{\partial x \, \partial z^*} dz^* - \int_{\infty}^{z} w^* S \, dz^* \tag{4.31}$$

Equation (4.31) is the time-stepping equation for the geopotential in the stratosphere. Finally, $\phi_s(y, z^* = 1)$ couples to the troposphere equations through the second matching condition, continuity of pressure across the interface:

$$\phi_s(x, y, z^* = 1, t) = \phi(x, y, \hat{p} = \hat{p}_t, t) \tag{4.32}$$

4.3.4 Cirrus cloud prognostic equation

To incorporate the cloud-radiative effects associated with cirrus clouds, we develop a proxy for cirrus clouds in the linear model:

$$\frac{\partial q_c}{\partial t} = w_s^*(z^* = z_c) - \overline{U}(z^* = z_c) \frac{\partial q_c}{\partial x} \tag{4.33}$$

where q_c is the non-dimensional cirrus cloud concentration, z_c is the vertical level at which cirrus clouds are dominant, and $\overline{U}$ is the mean wind advecting the clouds. The terms on the right hand side represent (1) an increase in cirrus cloud production efficiency through dynamical forcing, (2) a modulation of cirrus cloud concentration through advection by the background wind. The radiative heating in the model is additionally modified to include effects from cirrus clouds:

$$Q = C s_m + C_r q_c \tag{4.34}$$

where $C_r > 0$ is the cirrus cloud feedback parameter. In general, as C_r increases in magnitude in relation to C, more weight is given to the high-cloud parameterization of cloud-radiative feedbacks. Note, the original formulation of cloud-radiative feedbacks

in Khairoutdinov and Emanuel (2018) is obtained by setting $C_r = 0$.

What is the meaning of z_c? It represents the level where the presence of cirrus clouds dominates the radiative heating effect in the troposphere. Of course, this is an oversimplified view of radiative transfer, and an integrated metric of q_c is more appropriate to relate to radiative heating perturbations. Our parameterization will serve the purpose of simplified representation of cirrus clouds, and sensitivity tests to z_c are shown in this study. The sign and magnitude of $\overline{U}_c$, as well as the levels at which to parameterize z_c, will be discussed in the results section.

It is important to note that Equation (4.33) is not derived from first principles. Rather, it is simplistic and extremely crude representation of a couple processes that may modify the behavior of cirrus clouds. While there is evidence in observational data of the modulation of cirrus clouds by upward propagating waves (Boehm and Verlinde, 2000; Virts and Wallace, 2014), the extent to which these processes influence the MJO have yet to be validated with high-resolution numerical modeling. A linear equation such as Equation (4.33) does not do the complexity of cirrus cloud formation justice, and is not at all realistic. Rather, the form of Equation (4.33) is meant to highlight some potential mechanisms that may allow the stratosphere wind to modulate the MJO. It is our intention, in the spirit of simplicity, to understand how each of the modeled processes can affect growth of the MJO.

4.3.5 Numerical solutions

The fully coupled system consists of the tropospheric system [Equations (4.1) - (4.6)], the stratospheric system [Equations (4.10), (4.11), (4.13), (4.31)], the matching conditions [Equations (4.21) (4.22), (4.32)], and the parameterizations for cirrus cloud feedbacks [Equations (4.33), (4.34)]. Note that we have not assumed anything about the meridional or vertical dependence of $\overline{U}_s$. Unless otherwise noted, once $\overline{U}$ is chosen, the associated $\overline{T}$ is calculated through thermal wind balance.

The linear system is complex and cannot be solved analytically. As described in detail in Lin and Emanuel (2022), the system is solved numerically by integrating forward in time, initializing the troposphere with the rigid-lid solution while the

stratosphere is initialized at rest (Emanuel, 2020). The troposphere domain is discretized in y, while the stratosphere domain is discretized in y and z^*. Linear solutions are assumed to have zonal structure of the form $\exp(ikx)$. Spatial derivatives are numerically approximated with fourth order central differencing, and the system is step forward in time using fourth order Runge-Kutta. Since the initial wave is unbalanced, rapid gravity-wave adjustment occurs, requiring the use of dampening mechanisms to eliminate undesirable noise. First, a spectral filter is applied at each time step to eliminate small-scale noise. The spectral filter is described in detail in the appendix of Lin and Emanuel (2022). In addition, a strong sponge-layer is imposed along the edges and top of the domain, removing reflecting and downward propagating waves. The domain is re-scaled by a constant periodically in time to prevent numerical overflow. After a period of time, we isolate the growing mode of interest and infer the complex growth rate and structure of the eigenmode. The inferred eigenmode and growth rates are then rigorously checked to satisfy the governing equations, boundary conditions, and matching conditions.

Before proceeding, it is prudent to discuss some of the features of this model. Since there is a mean zonal wind in the stratosphere, it is possible for a critical layer to develop if the phase speed of the wave equals the mean wind. Linear numerical models are highly unstable in the presence of critical layers. In addition, the behavior of upward propagating waves when encountering critical layers can be highly sensitive to non-linearity and dissipation. Wave-breaking, wave reflection, and a transfer of momentum to the mean flow are quite often associated with critical layers, as is the case for the QBO (Lindzen and Holton, 1968). None of these features are represented in this model. However, there are some qualitative aspects of critical layers that linear models can capture, such as attenuation of the wave through the critical layer (Booker and Bretherton, 1967). It is important to note that the very small amount of meridional diffusion imposed in all of the prognostic equations is required for the linear model to maintain numerical stability. This may be because without explicit dissipation, critical layers would be able to form in the stratospheric domain, though this was not thoroughly investigated.

4.4 Linear solutions

Since the mechanism through which stratospheric wind can modulate MJO growth is the primary focus of the paper, we will focus our analysis on the eigenmode that most resembles the MJO in the linear model. All eigenmodes, unless otherwise stated (for instance, in the cirrus cloud section), are computed using the following selection of non-dimensional coefficients: $\alpha = 1$, $\chi = 1$, $C = 2.25$, $\gamma = 2$, $D = 1$, $G = 0.02$, $\delta_x = 30$, $S = 75$. Since the formulation of the tropospheric and stratospheric models is done in Khairoutdinov and Emanuel (2018) and Lin and Emanuel (2022), respectively, we refer the reader to those texts for details. Regardless, for continuity, we briefly describe the effect of these non-dimensional coefficients: α is the wind-induced surface heat exchange (WISHE) feedback parameter, χ is boundary layer damping, C represents the strength of cloud radiative feedback, γ modifies the time scale of tropospheric entropy, D is entropy damping, G is the gross moist stability, δ_x controls the magnitude of zonal geostrophy, and S represents the magnitude of stratospheric stratification. In all figures, colors shading with blue indicate negative quantities, and red indicate positive quantities.

Figure 5-1 shows horizontal summary eigenfunctions of the $k = 1$, eastward propagating, MJO-like mode, at varying vertical levels, but for zero, mean zonal wind in the stratosphere. The canonical Kelvin-wave signature near the equator, lagged and flanked by equatorial Rossby waves, is captured by the wind and saturation entropy anomalies in the troposphere. Strong westerly anomalies lag the maximum in vertical velocity, which is also preceded by strong easterly anomalies. This pattern somewhat resembles the observed MJO, except that westerly maxima are observed to be in phase with the maximum in vertical velocity, a common criticism of WISHE-based theories for MJO destabiliziation (Lin and Johnson, 1996; Kiladis et al., 2005). At 17-km, or 1-km above the tropopause, the magnitude and poleward extent of the equatorial Rossby wave signature is slightly diminished. Since the vertical structure of the MJO-like mode is dominated by the first baroclinic mode (Adames and Wallace, 2014), the sign of the horizontal winds at a fixed horizontal are nearly opposite

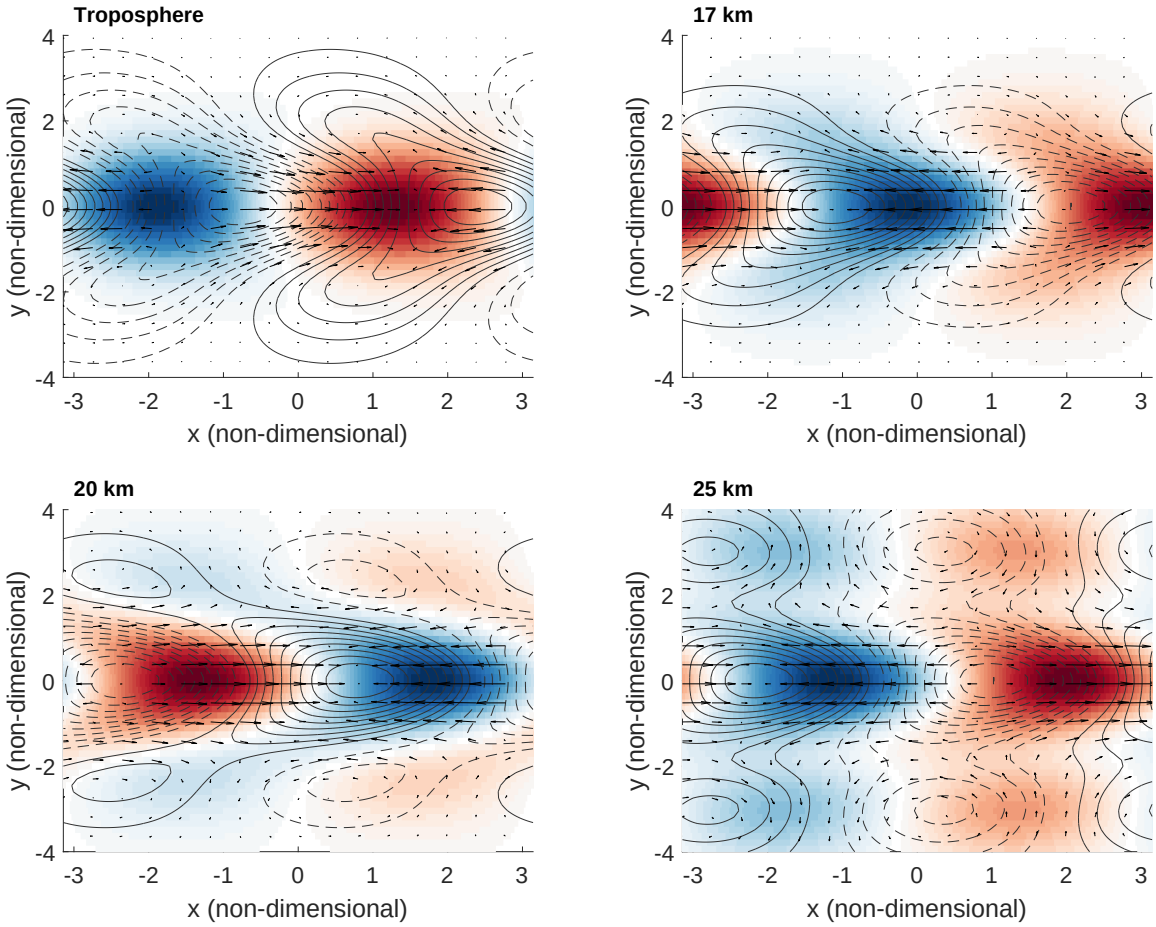

Figure 4-1: Horizontal cross-sections of the $k = 1$, MJO-like eigenmode at the (top-left) boundary layer, (top-right) 18-km, (bottom-right) 20-km, and (bottom-right) 25-km, for a zero-mean zonal wind stratosphere. Tropopause is arbitrarily set to 17-km. Contours indicate the saturation entropy in the troposphere and temperature in the stratosphere, where solid (dashed) lines indicate positive (negative) perturbations. Arrows indicate wind perturbations, and color shadings indicate vertical velocity perturbations at the level indicated (positive for upward), except for the boundary layer cross-section, where color shading indicates mid-level vertical velocity. Non-dimensional parameters selected are $\alpha = 1$, $\chi = 1$, $C = 2.25$, $\gamma = 2$, $D = 1$, $G = 0.02$, $\delta_x = 30$, $S = 75$.

those in the boundary layer, except for a slight eastward tilt with height in the stratosphere (not shown). At 20-km and 25-km, there becomes a much clearer separation between the components of the eigenmode that represent equatorial Rossby or Kelvin waves. Figure 5-2 shows a vertical cross section at the equator and at $y = 2$ (around 20° latitude). A strong first baroclinic mode structure is shown, with a smaller in magnitude barotropic mode. An eastward tilt with height exists on the equator, due to the presence of the upward propagating Kelvin wave. A weaker eastward tilt with height exists at $y = 2$, since the Kelvin wave signal at this latitude is weaker and the Rossby wave signal is stronger. In this control case, the stratospheric penetrative depth of the MJO-like eigenmode is around 4-5 km.

The MJO-like eigenmode in the linear model resembles the observed MJO, and, at-least in the linear framework, is able to excite both equatorial Kelvin and Rossby waves in the stratosphere. This zero, mean zonal wind stratosphere case will be referred to as the control case throughout this study. Our analysis will center on how the stratospheric wind modifies the linear growth rates and frequencies of the MJO-like modes. To quantify the extent to which upward wave radiation modifies these quantities, we will calculate the vertical energy flux associated with the MJO-like eigenmode. This is done by integrating $\overline{w'\phi'}$ over the stratosphere domain in the numerical model (Eliassen and Palm, 1960). Prior to vertical energy flux calculations, all eigenmodes are normalized according to the magnitude of the baroclinic zonal winds in the troposphere.

4.4.1 Upward wave radiation

In this section, we will analyze how MJO-associated upward wave radiation is modified by the stratospheric wind, by varying the sign, magnitude, and pattern of the imposed stratospheric wind, under no cirrus cloud feedbacks ($C_r = 0$). We analyze three particular cases: (1) constant zonal-mean wind, with a jump in mean wind across the tropopause, (2) linear shear in zonal-mean wind capped to a maximum value, and (3) realistic, oscillating zonal-mean winds (as is observed in the QBO).

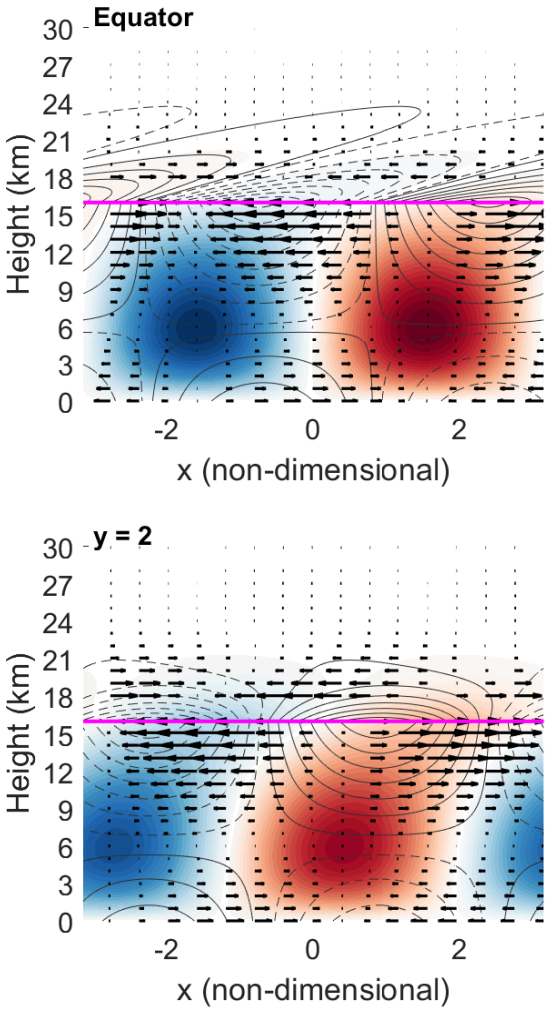

Figure 4-2: Vertical cross-sections of the $k = 1$, MJO-like eigenmode, for the control case of no mean wind in the stratosphere, $\overline{U}_s = 0$, on the (top) equator, and at (bottom) $y = 2$. As in Figure 5-1, the tropopause is arbitrarily set to 17-km, indicated by the magenta line. Contours indicate the geopotential perturbations, where solid (dashed) lines indicate positive (negative) perturbations. Arrows indicate wind perturbations, and color shadings indicate vertical velocity perturbations (positive for upward) at the level indicated in the label. Non-dimensional parameters selected are $\alpha = 1$, $\chi = 1$, $C = 2.25$, $\gamma = 2$, $D = 1$, $G = 0.02$, $\delta_x = 30$, $S = 75$, as in Figure 5-1.

Constant mean zonal wind

We first analyze the solutions with shear across the tropopause in the simplest limit of constant mean zonal wind in the stratosphere, allowing for a jump in mean wind across the tropopause (from the zero mean-wind in the troposphere to non-zero mean wind in the stratosphere). Though simple, this scenario is highly unrealistic, since under thermal wind balance, the discontinuity in zonal wind across the tropopause must be associated with a discontinuity in temperature across the tropopause, which could be a highly reflective interface. Instead, for simplicity, we opt to ignore the temperature anomalies associated with the jump in zonal wind on the tropopause. The advantage of this set-up is to understand, in the simplest way possible, the core dynamics of how the stratospheric wind can modulate upward wave radiation associated with the MJO. It is important to note that the infinite shear at the tropopause is highly unstable to Kelvin-Helmholtz instabilities, but the spectral filter is highly selective for the mode of interest.

Figure 5-3 shows horizontal cross-sections of the summary eigenfunctions, but for a constant easterly mean zonal wind in the stratosphere, $\overline{U}_s = -0.5$. While the boundary-layer eigenfunction is not significantly modified from the control case (c.f. Figure 5-1), the stratospheric wave patterns are. In particular, the Rossby wave component of the stratospheric solution is strongly confined to the lower stratosphere, and the Kelvin wave component of the stratospheric solution dominates. Above 25-km, there is very little qualitative evidence of upward Rossby wave propagation, suggesting strong damping of the Rossby wave in the stratosphere. This is consistent with linear theory of equatorial Rossby wave propagation under mean easterly flow [see equation 4.7.21 in Andrews et al. (1987)].

Figure 4-4 shows horizontal cross-sections of the summary eigenfunctions, but now for a constant westerly mean zonal wind in the stratosphere, $\overline{U}_s = 0.5$. Again, while the boundary-layer eigenmode is unchanged, the stratospheric wave patterns are significantly different from the control case. Now, the Kelvin-wave component of the solution is strongly damped in the vertical, and a clear signature of an upward

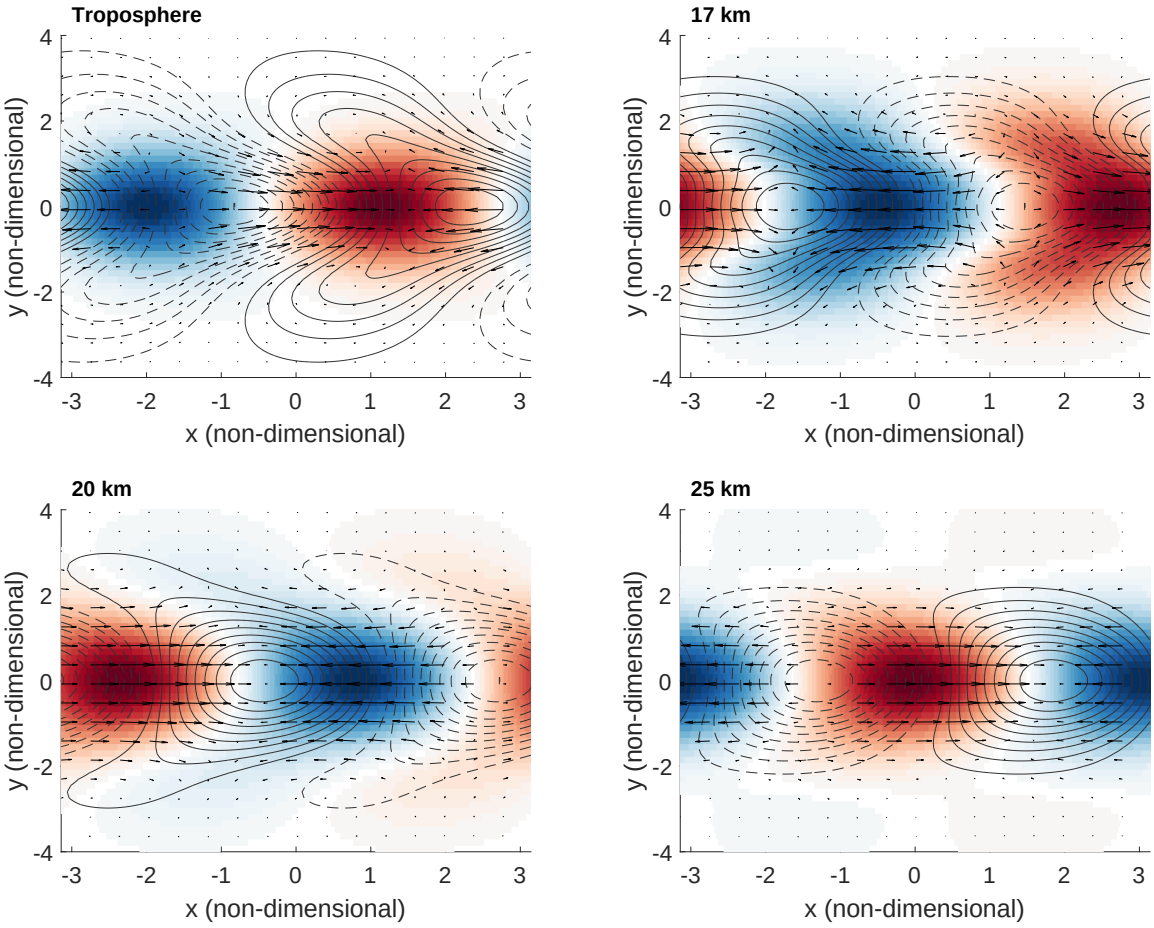

Figure 4-3: Similar to Figure 5-1 but for an constant easterly mean wind in the stratosphere, $\overline{U}_s = -0.5$.

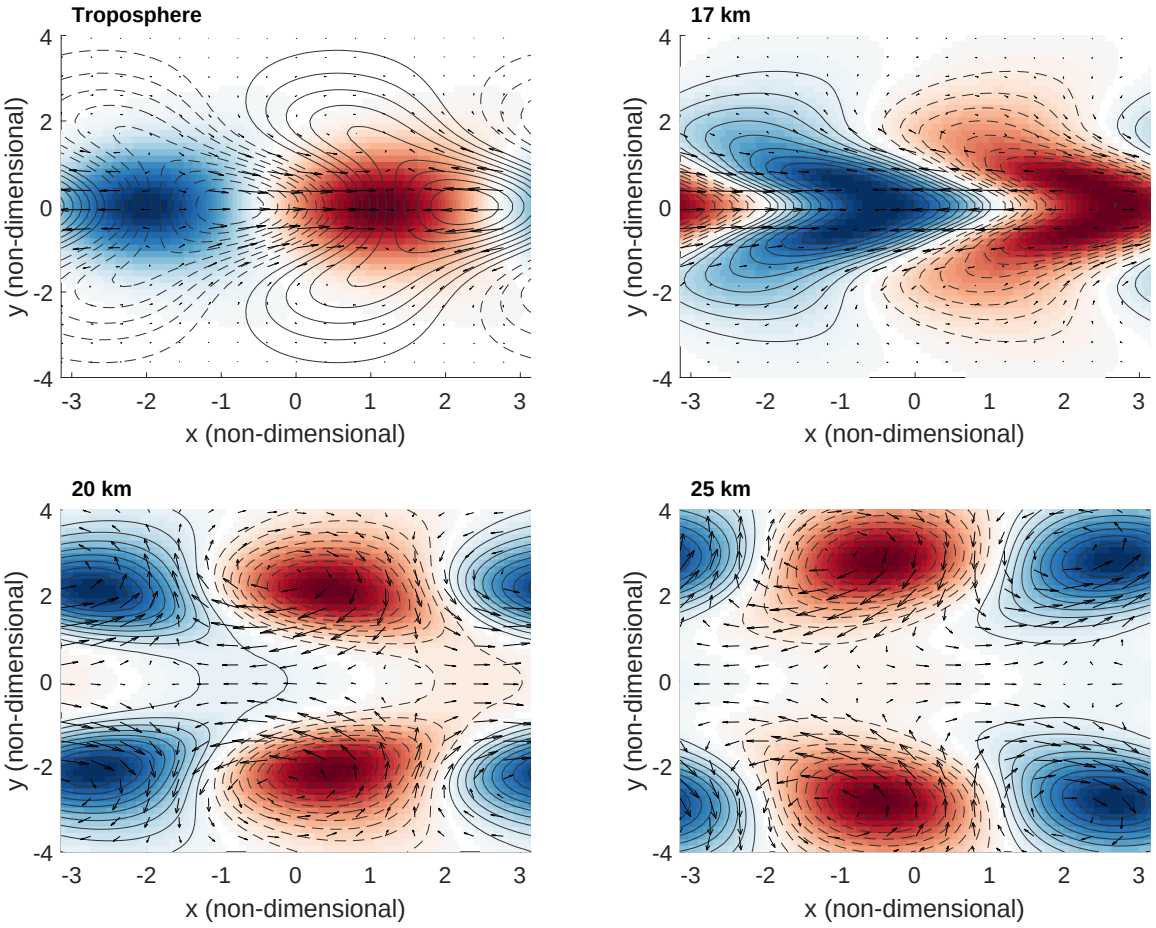

Figure 4-4: Similar to Figure 5-1 but for an constant westerly mean wind in the stratosphere, $\overline{U}_s = 0.5$.

propagating equatorial Rossby wave is evident. This is also consistent with linear theory of Kelvin wave propagation under mean westerly flow, in that the Doppler-shifted phase speed of the Kelvin-wave must be eastward [see equation 4.7.10 in Andrews et al. (1987)].

Figures 5-3 and 4-4 indicate that the kinds waves associated with the MJO that can propagate into the stratosphere are dependent on the sign of the mean zonal wind, but it is not as immediately obvious how that would affect the linear growth rate of the MJO. Figure 4-5 shows the growth rate, frequency, and vertical energy flux of the $k = 1$, MJO-like mode, for varying magnitudes and signs of constant stratospheric mean wind. Interestingly, the growth rate minimizes at a mean wind of $\overline{U}_s = 0.5$, or moderate westerlies in the stratosphere. On the other hand, the growth rate increases with increasing easterlies, as compared to the control case. The frequencies (or phase speeds) are slightly modified as well: the MJO-like mode seems to propagate slightly slower under a constant mean westerly wind. As an aside, it is important to note that the absolute magnitude of the growth rate in this case is somewhat arbitrary, since small perturbations to the magnitude of the non-dimensional cloud-radiative feedback in the linear model strongly modify the growth rate, but do not strongly modify the horizontal structure of the eigenmodes (not shown). The vertical energy flux associated with the MJO-like mode is largest for strong easterly mean winds, and decreases monotonically until a mean wind of $\overline{U}_s = 0.5$, after which it increases slightly with increasing westerlies.

How can we explain the relationship of the vertical energy flux with mean wind speed? To start, in a linear model, the phase speed of the MJO-like mode in the troposphere must be equal to the Doppler-shifted phase speed of the stratospheric wave:

$$c_{\text{mjo}} = \overline{U}_s + c_{\text{wave}} \tag{4.35}$$

Suppose that c_{mjo} is more or less fixed by tropospheric dynamics. Then, under mean easterly flow, c_{wave} must increase to match c_{mjo}. The dispersion relation for upward propagating Kelvin waves states that faster propagating Kelvin-waves have larger

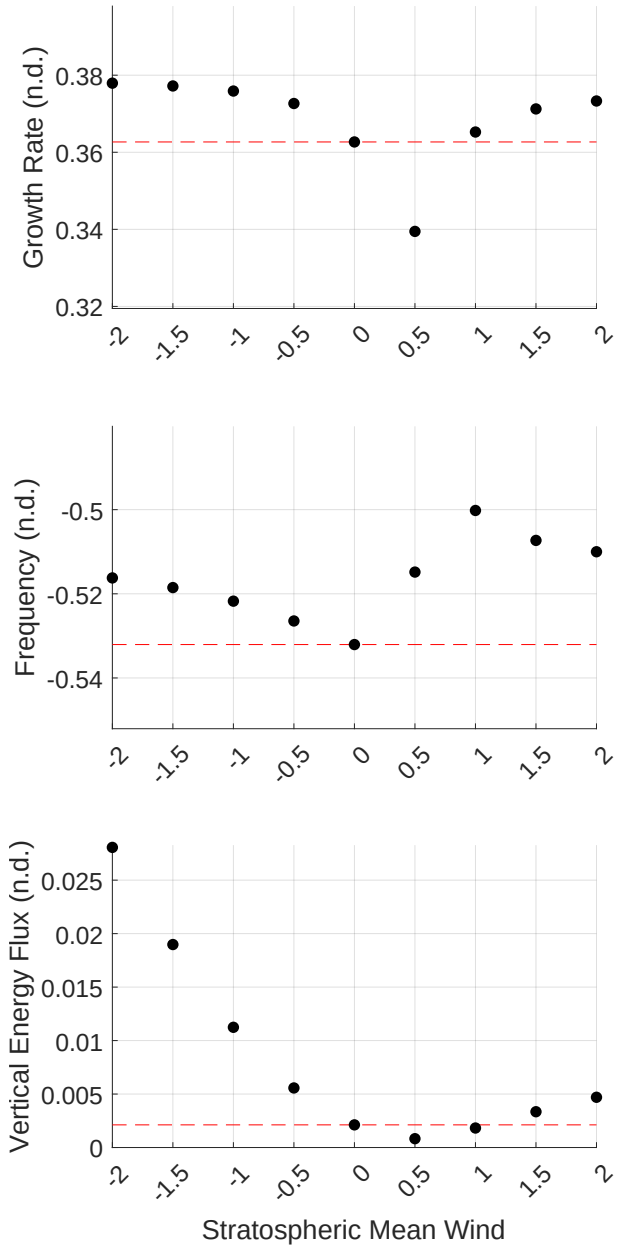

Figure 4-5: (Top) Growth rate, (middle) frequency, and (bottom) vertical energy flux of the $k = 1$, slow propagating mode, for varying magnitudes of constant stratospheric mean wind. Dashed red-lines indicate the same quantities but for the zero-mean wind control case. Non-dimensional parameters selected are $\alpha = 1$, $\chi = 1$, $C = 2.25$, $\gamma = 2$, $D = 1$, $G = 0.02$, $\delta_x = 30$, $S = 75$.

vertical group velocities (Andrews et al., 1987; Lin and Emanuel, 2022). In other words, more wave-energy radiates upward for faster moving Kelvin waves. This is presumably what is occurring in the model: under strong easterlies, the Kelvin-wave component of the stratospheric mode must propagate faster to match the phase speed of the tropospheric mode. A signature of this effect is a shift to larger vertical wavelengths of the Kelvin-wave, which has an eastward phase tilt with height if it is propagating energy upward. This is quite evident from the left column of Figure 4-6, which shows the vertical cross-sections of the MJO-like eigenmode under mean easterly flow, as the vertical wavelength of the Kelvin-wave mode near the equator increases compared to the control case (see Figure 5-2). Indeed, a strong eastward tilt in temperature fields with height is observed in the stratosphere, from composites of the MJO during easterly phases of the QBO (Hendon and Abhik, 2018). Note, the horizontal winds and vertical velocity perturbations can be discontinuous across the tropopause, but the geopotential perturbations cannot, as enforced by the matching conditions.

On the other hand, Figure 4-6, right column, shows the vertical cross-sections of the MJO-like eigenmode under westerly mean flow. On the equator, the equatorial Kelvin wave is trapped in the troposphere and cannot propagate upwards. Polewards of the equator, at $y = 2$, the vertical tilt with height becomes westward, indicating the presence of upward propagating Rossby waves. This explains the stratospheric westward tilt in height observed by Hendon and Abhik (2018) in their composites of the MJO during westerly phases of the QBO. The gravest Rossby wave cannot make up for the lost vertical energy flux due to suppressed Kelvin wave, and, is natural to expect, since the phase speed of the $n = 1$ Rossby wave is a third of that of the Kelvin wave. Thus, the vertical energy flux maximizes when the linear Kelvin waves have the fastest phase speed, or under increasing easterlies.

Why, then, are the growth rates smallest when $\overline{U}_s = 0.5$, and not when the vertical energy flux maximizes (i.e when mean easterlies are the strongest)? The answer seems to lie in the phase displacement of the barotropic mode by the stratospheric winds. Figure 4-7 (top-left) shows the budget of the time dependent saturation moist entropy

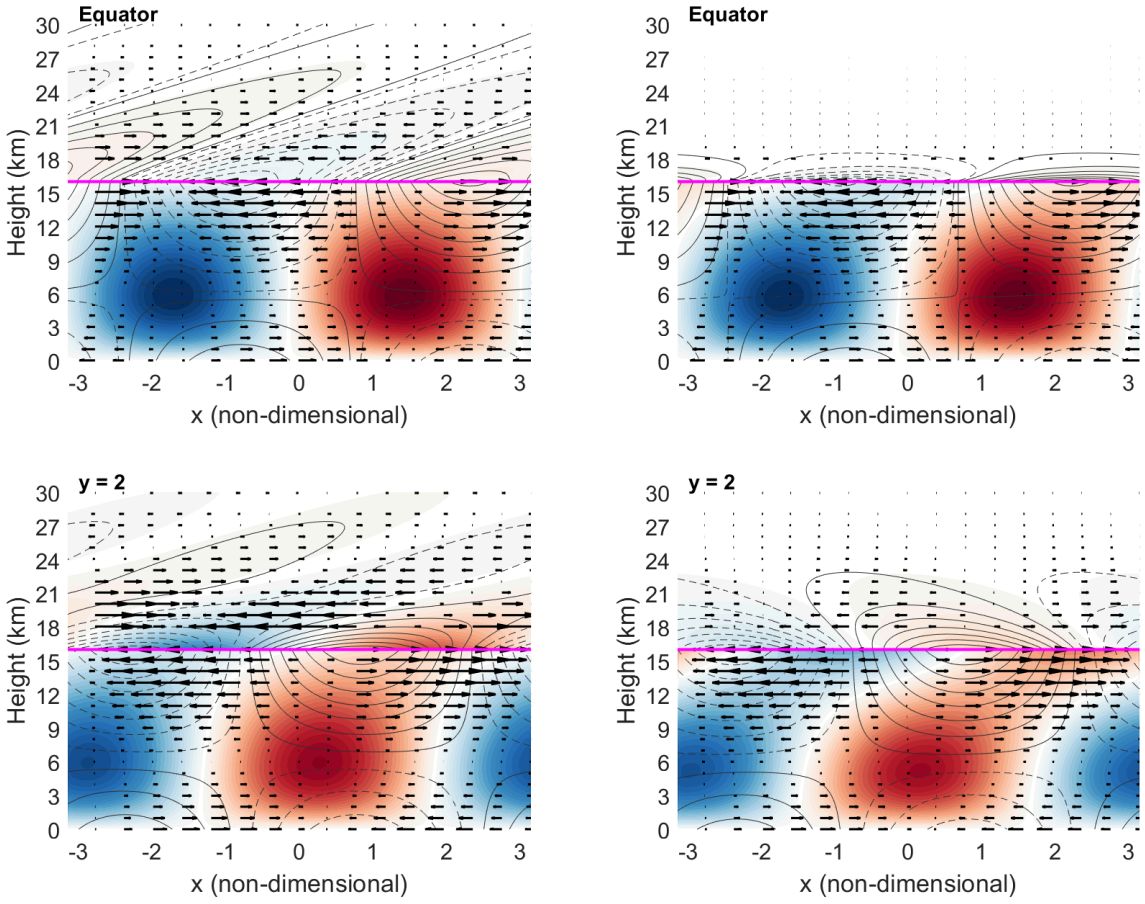

Figure 4-6: Similar to Figure 5-2 but for (left column) $\overline{U}_s = -0.5$ and (right column) $\overline{U}_s = 0.5$, on the (top row) equator, and on (bottom row) $y = 2$.

equation on the equator, and in particular, shows the amplitude and phase offset of each term from σs. The term that shifts the most between the easterly and westerly cases is the WISHE term involving the barotropic winds. During westerlies, the barotropic winds are further offset from the baroclinic winds. The phase shift is also consistent across all latitudes. Figure 4-7 (top-right), shows the phase offset of the boundary layer baroclinic zonal winds from the boundary layer barotropic zonal winds, for all y. For the control case, the baroclinic winds lag the barotropic winds by around an eighth of a cycle. Increasing the magnitude of the easterly wind in the stratosphere decreases the phase lag between the baroclinic and barotropic wind, through westward “advection" of the barotropic mode. Conversely, westerly winds in the stratosphere show the opposite effect, “advecting" the barotropic mode eastward and increasing the phase lag between the barotropic and baroclinic mode. The phase shift can be significant, since out of phase barotropic and baroclinic modes can make the barotropic mode winds opposite signed from the baroclinic winds. For this effect to be significant, the magnitude of the barotropic mode must not be small. Figure 4-7, bottom-right, shows the ratio of the barotropic zonal wind to the total zonal wind. In general, the barotropic mode is around an order of magnitude smaller than the baroclinic mode (Lin and Emanuel, 2022), but the barotropic mode zonal wind ratio maximizes at $\overline{U}_s = 0.5$. This explains why the growth rate minimizes at $\overline{U}_s = 0.5$, as shown in Figure 4-5. In general, this means that the superposition of the barotropic and baroclinic modes can lead to an increase or decrease in the magnitude of the boundary layer winds, which then modifies the enthalpy flux in the boundary layer through WISHE.

This then begs the question, is this a realistic mechanism by which the stratospheric winds can modify the tropospheric barotropic mode? While it is clear that stratospheric winds can modify upward propagating waves from the troposphere, it is still unclear how stratospheric winds can affect the tropospheric barotropic mode. After all, the imposed jump in mean wind across the tropopause is not realistic and highly unstable to Kelvin-Helmholtz instabilities, owing to the infinite shear at the tropopause. In the linear model, the first baroclinic mode in the troposphere ter-

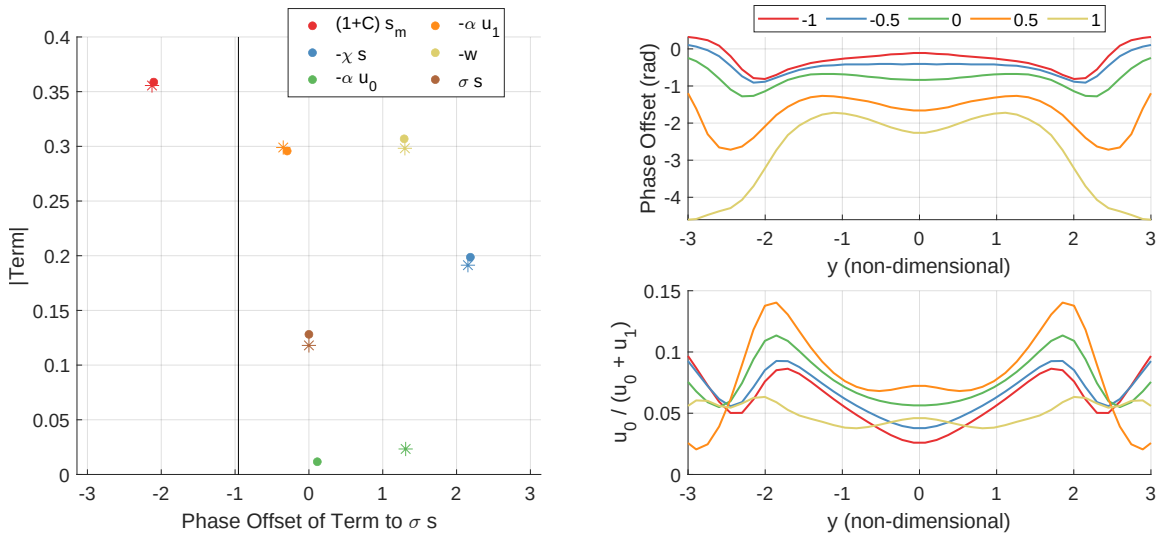

Figure 4-7: (Left) Budget decomposition of the time dependent saturation moist entropy s equation for the $k = 1$ MJO-like mode, where the sum of $(1 + C)s_m$, $-\chi s$, $-\alpha u_b$, and $-w$, equals σs. Solid (dashed) lines are the budget for $\overline{U}_s = -0.5$ ($\overline{U}_s = 0.5$). (Top right) Phase lag of the boundary layer baroclinic zonal winds with respect to the boundary layer barotropic zonal winds, under (line colors) varying constant stratospheric mean zonal wind, $\overline{U}_s$. (Bottom right) Similar to top right but for the real part of the ratio of the barotropic zonal wind to the total zonal wind.

minates abruptly at the tropopause, since the assumption of strict quasi-equilibrium is only valid in the troposphere. As such, the troposphere communicates with the stratosphere through the tropospheric barotropic mode, via the matching conditions. It is not surprising, then, that the tropospheric modes respond strongly to non-zero mean wind at the tropopause. However, a barotropic mode can also exist in the stratosphere, though it is presumably highly sensitive to the boundary conditions used at the upper boundary. In the linear model, the barotropic mode in the stratosphere cannot be excited, since an unrealistic sponge layer exists at the top of the domain to eliminate spurious noise and gravity wave reflection. The extent to which the barotropic mode in the troposphere and that in the stratosphere can be considered separate is not clear. It seems reasonable that stratospheric winds can modify the stratospheric barotropic mode, which in turn will modify the tropospheric barotropic mode. However, at least in the way the linear model is currently formulated, unrealistic “tropopause forcing" is required to strongly modify the tropospheric barotropic mode. And, as we shall discuss in the next section, the phase shifting behavior of

the barotropic mode seems to be, rather unsurprisingly, a singular limit of the linear model. This does not necessarily mean that the tropospheric barotropic mode is independent of the stratospheric winds, and more work is required to uncover that relationship.

Constant shear mean zonal wind

To remove the unrealistic jump in mean zonal wind at the tropopause, we formulate another set of simple experiments, in which the mean zonal wind increases linearly until it reaches $\overline{U}$, after which it becomes constant. Mathematically, this is:

$$\overline{U}_s(z^*) = \min\left(\Gamma(z^* - 1), \overline{U}\right) \tag{4.36}$$

where the reader is reminded that the tropopause is defined at $z^* = 1$. Γ, which controls the depth of the linear shear layer, is initially set such that $\overline{U}$ is 3-km above the tropopause.

Figure 4-8, black circles, shows the growth rates and frequencies of the $k = 1$, MJO-like mode under varying values of $\overline{U}$. When the zonal mean wind no longer jumps at the tropopause, but instead increases linearly up until $\overline{U}$, the growth rates are weakest under easterly flow, and strongest under westerly flow. The vertical energy flux is largest under easterly flow, for the reasons cited in the previous section. Figure 4-9 shows the baroclinic zonal wind phase lag from the barotropic zonal wind, where we observe that the phase lag near the equator is not dramatically shifted for different $\overline{U}$. The magnitude of the barotropic mode is greatest with easterlies in the stratosphere, and weakest for westerlies in the stratosphere. Thus, there is no phase shifting of the barotropic mode by the stratospheric winds, contrary to when a jump in mean zonal wind was imposed across the tropopause.

How does the depth of the shear layer (the magnitude of Γ) affect the results? We experimented by taking the constant shear case to the limit of the constant zonal wind in the stratosphere, by trying decreasing depths of the shear layer. The smallest linear shear layer we tried was 100-m. In order to accommodate this, the vertical resolution

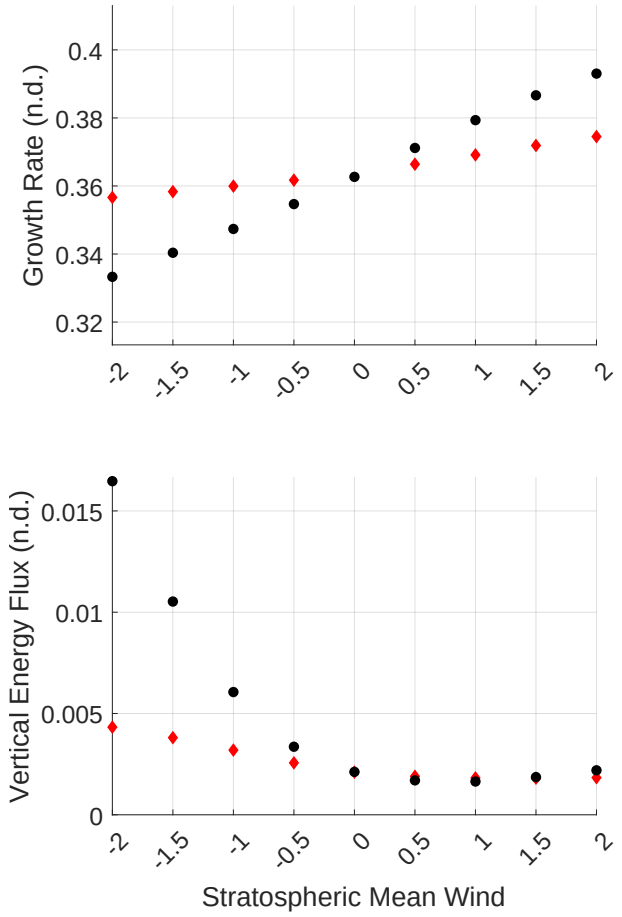

Figure 4-8: Same as Figure 4-5, but for (black circles) constant linear shear in lower stratospheric wind, capped at the indicated value, and (red diamonds) QBO-like oscillations in stratospheric mean zonal wind, where the magnitude of the indicated value represents the peak value in mean wind, and the sign represents the phase of the wind that the wind first oscillates toward. Frequency is not shown since it is not modified.

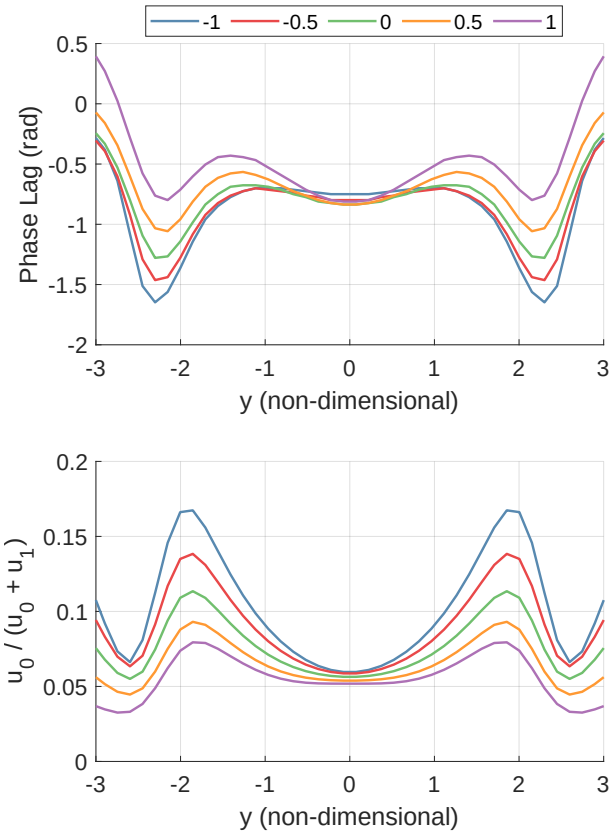

Figure 4-9: Same as the right column of Figure 4-6, but for the case of constant linear shear in lower stratospheric wind, capped at the indicated value.

of the linear model was increased to $\Delta z^* = 10$ m. In all of the cases we tried, the growth rates were largest under westerly mean flow, and weakest under easterly mean flow, owing to increase vertical energy flux (not shown). It is only when a jump in mean wind at the tropopause that the growth rates are largest under easterly flow. As hinted at earlier, this means that the behavior of the MJO-like mode under a jump in mean zonal wind across the tropopause is a singular limit of the linear model. The case of constant shear in the mean zonal wind is certainly more realistic than the case of a jump in mean zonal wind, which certainly casts some doubt over the realism of the barotropic mode phase shifting mechanism, as discussed in the previous section.

QBO-like mean zonal wind

Finally, we can graduate to a realistic, QBO-like oscillation in mean zonal wind. The mathematical form of the mean wind we impose is:

$$\overline{U}_s(y, z^*) = \overline{U}\, R\, \sin\big(b_1(z^* - 1)\big) \exp\big(-b_2 y^2\big) \tag{4.37}$$

where b_1, b_2, and b_3 are non-dimensional constants that control the vertical wavelength of the oscillation, meridional extent of the mean wind, and vertical extent of the damping factor, respectively. R is a non-dimensional damping factor that is only active in the lower stratosphere and ensures that there is no temperature jump across the tropopause:

$$R(z^*) = 1 - \exp\left(\frac{-(z^* - 1)^2}{b_3}\right) \tag{4.38}$$

We found that $b_1 = 5$, $b_2 = 0.5$, $b_3 = 0.01$ lead to a reasonable representation of the QBO and it's associated temperature anomalies (see Figure 4-10, right column). For instance, the meridional extent of the idealized QBO in the linear model corresponds well to the meridional extent of the real QBO, at least when compared to zonal winds estimates by ERA5 re-analysis from 1979-2020. While the vertical structure of the QBO is not exactly sinusoidal, the above parameters reasonably estimate the vertical wavelength of the observed QBO. Figure 4-10, left column, shows an example of the imposed QBO-like mean state in the stratosphere, using the above parameters and

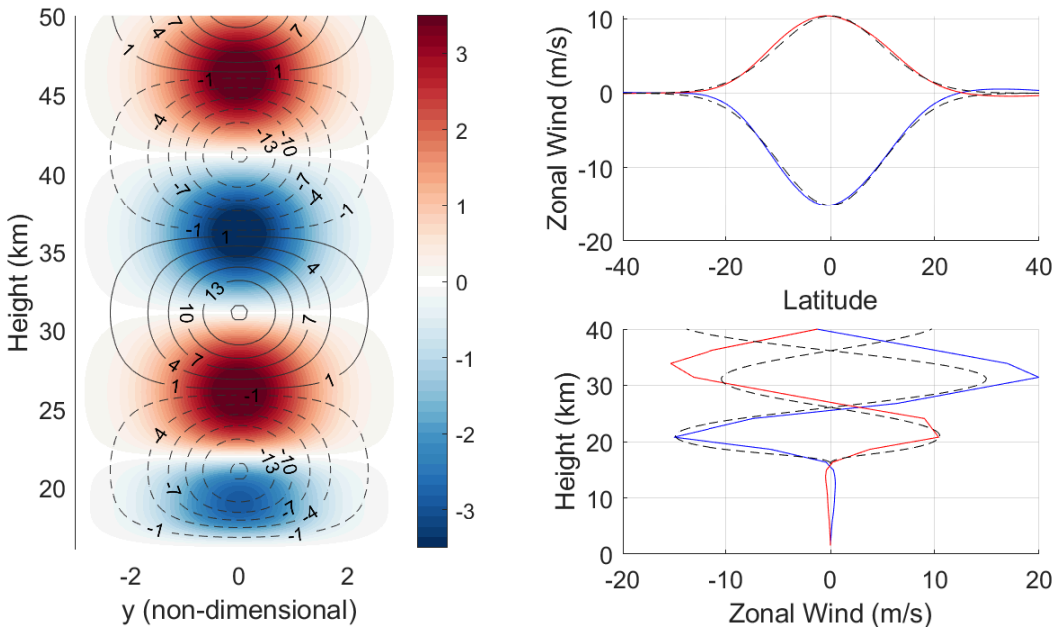

Figure 4-10: (Left) Example of imposed QBO-easterly mean-state in the stratosphere, with contours indicating dimensional zonal wind speed ($m\ s^{-1}$), and shading indicating associated dimensional temperature anomalies (K). Contour intervals are in spacing of 3 $m\ s^{-1}$, starting at $\pm 1\ m\ s^{-1}$. Non-dimensional parameters are $\overline{U} = -0.5$, $b_1 = 5$, $b_2 = 0.5$, $b_3 = 0.01$, and the tropopause is arbitrarily set to 16 km. (Top right) Meridional dependence of the zonally averaged, anomalous zonal wind during (blue) QBOE and (red) QBOW phases from ERA5 re-analysis 1979-2020, with dashed black lines indicating the dimensional, meridional dependence of the zonal wind in the linear model, arbitrarily scaled for zonal wind magnitude. (Bottom right) Same as top right but for the vertical structure of the anomalous zonal wind during (blue) QBOE and (red) QBOW, with height.

for $\overline{U} = -0.5$.

Does the imposition of a realistic stratospheric mean wind change the behavior of the linear model? Figure 4-8, red diamonds, shows the growth rates and frequencies of the $k = 1$, MJO-like mode under varying values of $\overline{U}$. Again, the growth rates are largest under westerly mean winds and smallest under easterly mean winds, due to increased vertical energy flux under easterlies, though the magnitude of the differences among the westerly and easterly growth rates is slightly diminished as compared to the differences in the constant shear experiments. The baroclinic mode phase lag and barotropic wind ratio are nearly identical across all of the experiments (not shown). Thus, the behavior of the MJO-like mode under varying stratospheric winds

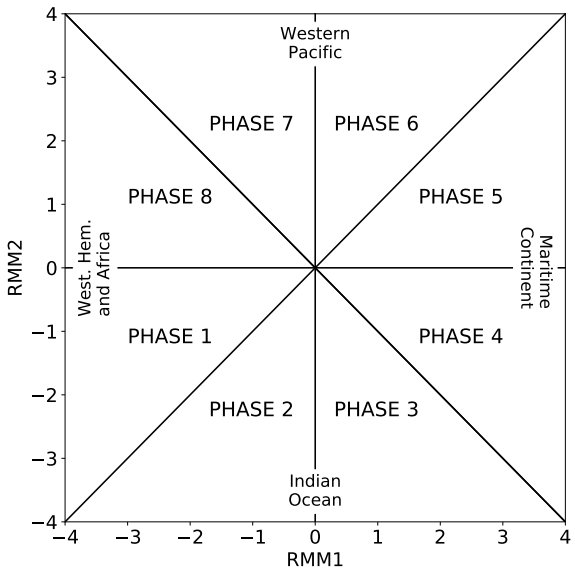

Figure 4-11: MJO phase space defined by two components of the Real-time Multivariate MJO (RMM) index, as defined in Wheeler and Hendon (2004). MJO progression is split into eight phases, with labeled regions indicating where maximal MJO convection occurs.

is qualitatively similar to the case of linear shear, owing to the increased vertical energy flux during stratospheric easterlies.

4.4.2 Cloud-radiative feedbacks

If there is actually increased wave-energy loss to the stratosphere under easterlies than westerlies (and the phase shift of the barotropic-mode mechanism is unrealistic), then it remains perplexing why the MJO is observed to be weaker under QBO westerlies in boreal winter. In this section, we will use the linear model to attempt to understand how stratospheric winds can modulate cirrus cloud feedbacks.

First, it is instructive to look at the relationship between cirrus clouds with convection. Figure 4-12 shows tropical averaged (5°S-5°N) ice and water cloud fraction anomalies (deseasonalized) from 10 years of satellite-based CALIOP measurements (2007-2017), aggregated over combined phases of the MJO, following Virts and Wallace (2010). The phases of the MJO are defined following the convention of Wheeler and Hendon (2004), as summarized in Figure 4-11. A label of “Phase 1/-Phase 5"

aggregates normal anomalies from Phase 1 with anomalies multiplied by -1 from Phase 5, increasing sample size for the mean composites, which are weighted by MJO amplitude. In this case, water cloud anomalies are used as a proxy for anomalous convection; note that the water cloud fractions are quite small and noisy. The eastward progression of the MJO is quite evident as one moves downward from the top to bottom panels of Figure 4-12. There are also significant ice cloud anomalies (nearly 7%) present near or at the climatological tropopause (15-16 km), as well as in the upper portion of the TTL ($\approx$ 17 km). While the ice clouds are more or less collocated with lower tropospheric convection until around 13 km, especially during Phase 2/-Phase 6 and Phase 3/-Phase 7, it can be argued that there is substantial eastward tilt with height past $\approx$ 14 km. For instance, in Phase 2, precipitation is centered around 70° W, but significant positive cirrus cloud anomalies extend eastward by nearly 30° longitude, and as high up as 17 km. However, the cloud data are quite noisy. Since CALIPSO is polar-orbiting, the data are generally sparse in space and time, even when accumulated monthly. Splitting the analysis into combined phases of the MJO provides useful insight, but any further decompositions by QBO phase or season lead to too small sample sizes that preclude meaningful analysis.

Despite the sparsity of the observations, there is some evidence that cirrus clouds associated with MJO-convection exhibit a strong eastward tilt with height in the TTL. Modulation of these high cirrus clouds by the stratosphere can influence radiative heating in the troposphere. If the eastward tilt with height is significant, what remains is to understand how the eastward tilt arises. We propose two mechanisms through which this could occur: (1) dynamical modulation of cirrus clouds by upward propagating waves, and (2) advection of cirrus clouds by the background wind. On the first mechanism, anomalous vertical motion from upward propagating Kelvin waves, which have eastward tilts with height, could be responsible for near-equator TTL cirrus cloud anomalies. In regards to the second mechanism, it is also possible for cirrus clouds to be advected westward by upper tropospheric westerlies. The effect of these two mechanisms are crudely parameterized in the linear model [see Equation (4.33)].

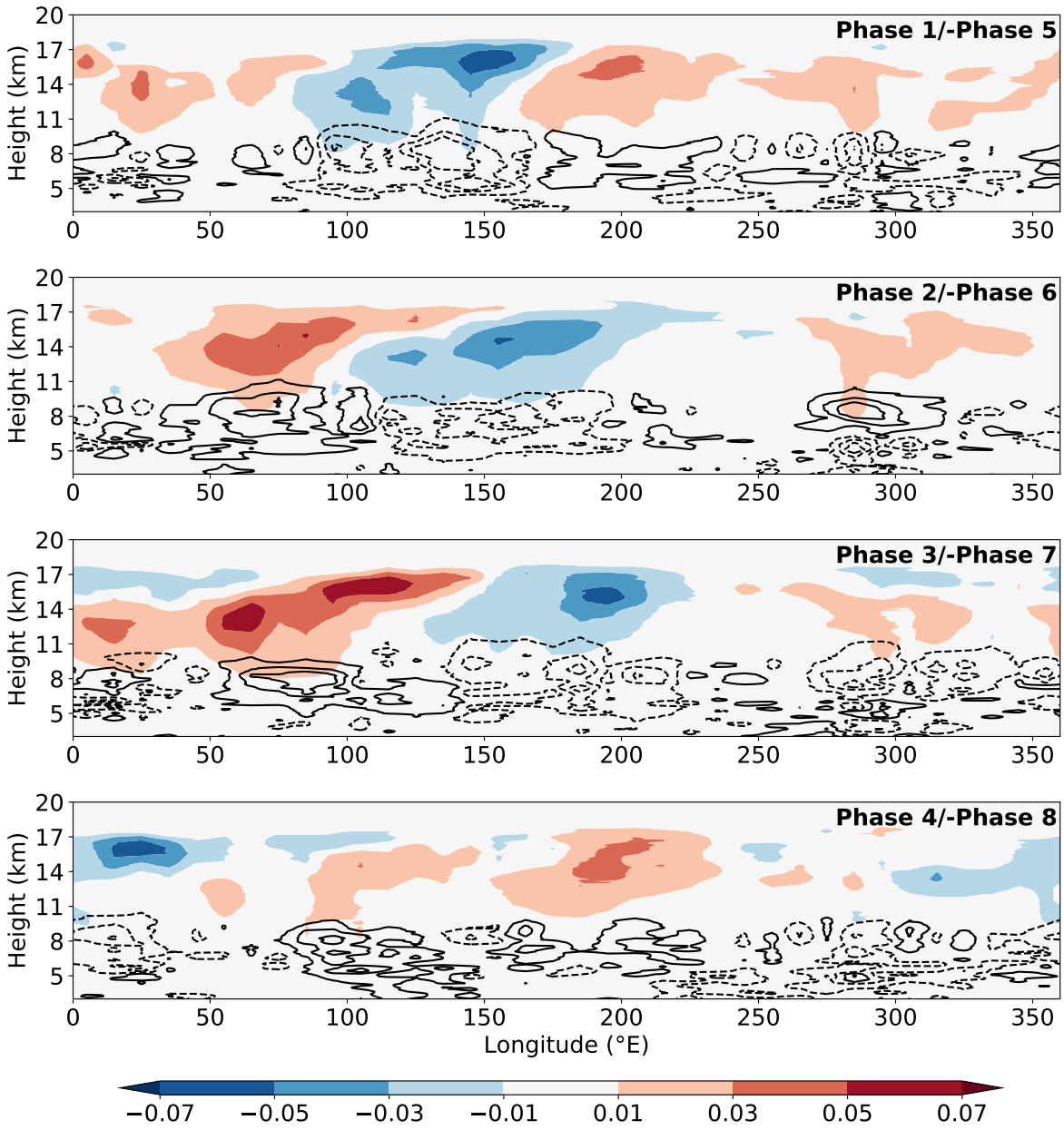

Figure 4-12: Horizontal cross-sections of the tropical averaged (5°S-5°N), monthly anomalies of (colors) ice cloud fraction and (contours) water cloud fraction associated with aggregate phases of the MJO, from 10 years (2007-2017) of level 3 CALIOP cloud occurrence profiles. Ice and water cloud samples are deseasonalized and accumulated over boxes of width 10° longitude. Phases are determined using monthly RMM index, as defined in Figure 4-11. Cloud fraction anomalies are averaged over the indicated phases, but weighted according to MJO amplitude. Contours are solid (dashed) for positive (negative) anomalies. Contour levels start at -0.005 with spacings of 0.002.

Dynamical modulation of cirrus clouds

The first term on the RHS of Equation (4.33) represents the dynamical contribution of upward propagating waves to cirrus cloud formation. It is not clear at first glance, however, if Equation (4.33) reproduces the observed phase relationship between cirrus clouds and convection in the linear model. Further, although we know the constant z_c should be confined to the upper troposphere/lower stratosphere in the linear model, the behavior of the MJO-like mode under varying stratospheric winds can also be modulated by the level at which we set z_c.

In order to verify if the cirrus-cloud parameterization qualitatively reproduces the phase relationship of cirrus clouds with convection, we run a "control" experiment under the simplest stratospheric conditions: no mean wind ($\overline{U}_s = 0$) and no advection of cirrus clouds ($\overline{U}_c = 0$), but with cirrus-cloud radiative feedbacks active. We set $C_r = 0.5$, and decrease C by the same amount ($C = 1.75$) to obtain modes that have a similar magnitude of cloud-radiative feedbacks. This choice was motivated by the fact that the bulk of the cloud-radiative forcing can be represented by the original cloud-radiative parameterization (C) in Khairoutdinov and Emanuel (2018), which relates perturbation radiative heating to vertically integrated entropy. These clouds are more or less collocated with MJO-associated convection [Figure 4-12], and around 10-14 km in height. C_r tries to represent the radiative forcing of clouds above those levels, since they exhibit an eastward tilt with height that is not collocated with convection. These clouds are optically thinner, but can still have significant radiative forcings since they are higher up in the atmosphere. We also set $z_c = 17$ km, or 1 km above the tropopause. All other non-dimensional parameters of the MJO-like mode are kept the same. Despite the change in the way the cloud-radiative feedback is parameterized as compared to Khairoutdinov and Emanuel (2018), we have confirmed that the tropospheric eigenmodes are qualitatively similar to the MJO-like mode shown in the control case.

Figure 4-13 shows the zonal phase relationship between s, s_m, q_c, w_{trop}, $w_s^*(z_c)$ on the equator. The peak saturation moist entropy (s, or temperature) leads the peak

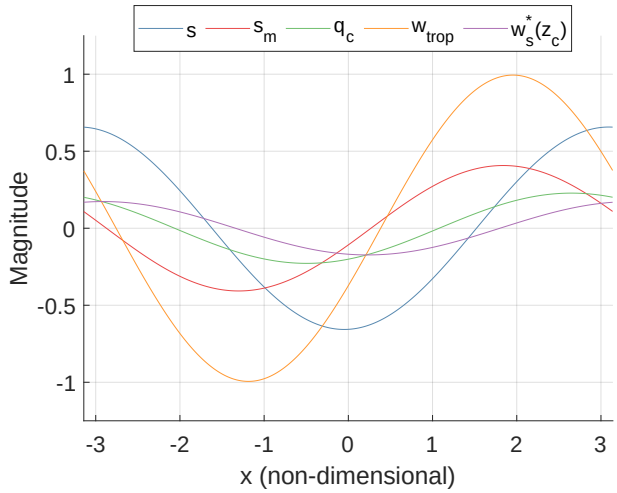

Figure 4-13: Longitudinal phase relationship of s, s_m, q_c, w_{trop}, and $w_s^*(z_c = 17\,\text{km})$ along the equator, for the $k = 1$, MJO-like mode with a tropopause height of $H = 16$ km, no advection, and no stratospheric wind. Non-dimensional parameters selected are $\alpha = 1$, $\chi = 1$, $C = 1.75$, $C_r r = 1.75$ $\gamma = 2$, $D = 1$, $G = 0.02$, $\delta_x = 30$, $S = 75$, $C_r = 0.5$, $\overline{U}_c = 0$, and $\overline{U}_s = 0$.

tropospheric vertical velocity, which is itself in phase with mid-level moist entropy (s_m). The maximum in vertical velocity at 17 km is eastward of the maximum in tropospheric vertical velocity; as discussed previously, the eastward tilt with height coincides with the upward propagating Kelvin-wave near the equator. The maximum in the proxy for cirrus clouds, q_c is eastward of w_{trop} and s_m, which is consistent with the eastward tilt in height for high cirrus clouds shown in Figure 4-12. Note that the maximum of q_c is still westward of the maximum of s. Thus, at least in the "control" case, the phase relationship between and cirrus clouds and convection is qualitatively consistent with that shown in aggregated satellite observations of clouds.

Next, we impose the previously formulated QBO-like wind [Equation (4.37)] in the stratosphere, to understand how modification of upward propagating waves and their associated vertical velocity anomalies can influence cirrus cloud formation. We run a set of experiments varying $\overline{U}_s$ and z_c, but still do not include any advection of cirrus clouds ($\overline{U}_c = 0$). Figure 4-14 shows the growth rate, frequency, and vertical energy flux of the MJO-like mode under varying stratospheric winds, and $z_c = 16.5, 17, 17.5$ km. The growth rates are higher for easterly phases of the QBO than westerly phases, with the largest differences in growth rates between the two occurring when $z_c = 17.5$

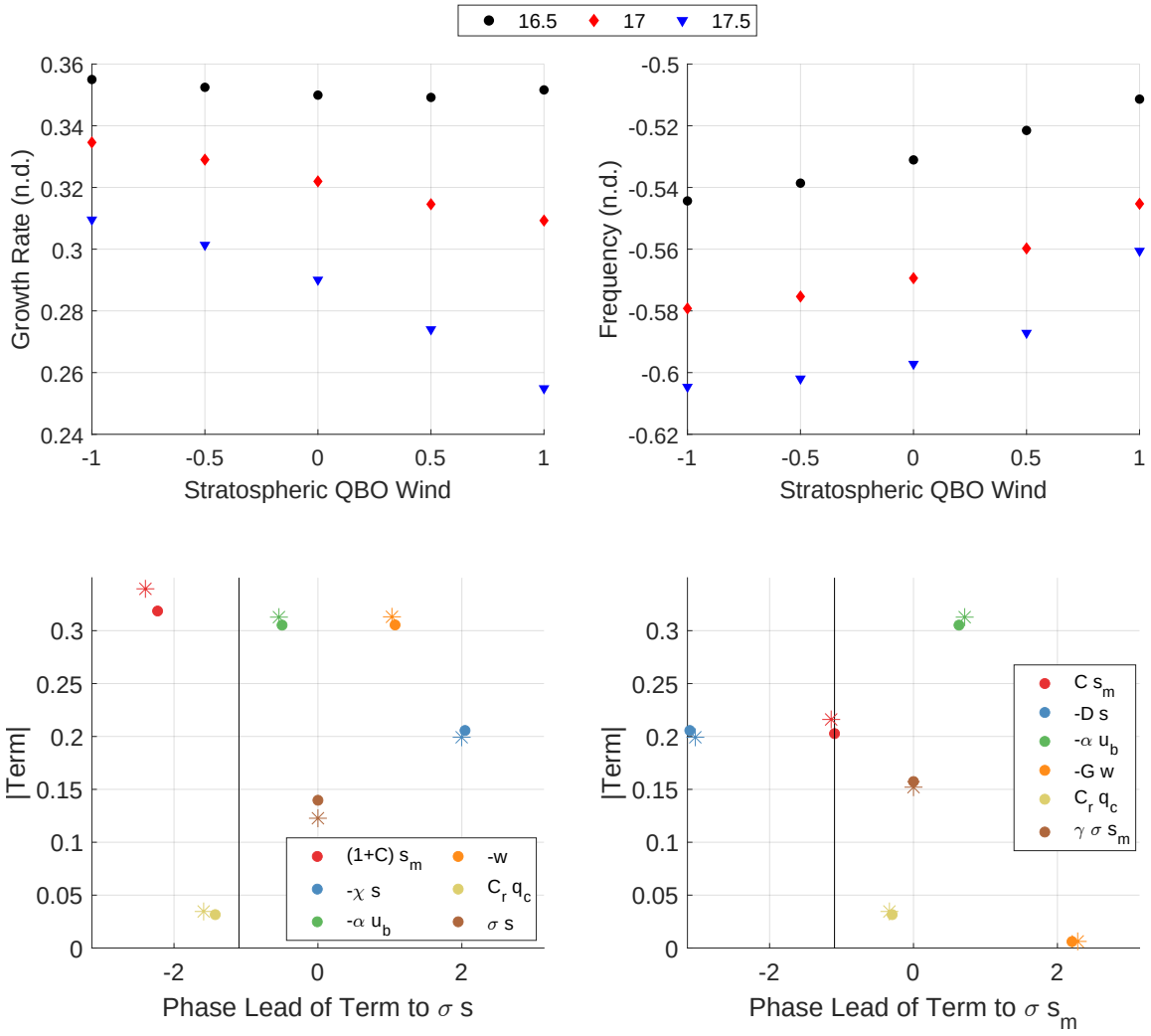

Figure 4-14: (Top-left) Growth rate, (top-right) frequency, and (bottom-left) vertical energy flux of the $k = 1$, slow propagating mode, for varying values of stratospheric QBO wind and z_c, which are (black circles) $z_c = 16.5$ km, (red diamonds) $z_c = 17$ km, and (blue triangles) $z_c = 18$ km. (Bottom-right) Meridional dependence of the phase lag of q_c from s, for $z_c = 17$ km and varying stratospheric QBO winds. Non-dimensional parameters selected are $\alpha = 1$, $\chi = 1$, $C = 1.75$, $\gamma = 2$, $D = 1$, $G = 0.02$, $\delta_x = 30$, $S = 75$, $C_r = 0.5$, and $\overline{U}_c = 0$.

km, and the smallest when $z_c = 16.5$ km. This is consistent with the observation that the MJO is stronger during QBO easterlies than westerlies. The phase speeds of the MJO-like mode are faster for higher z_c, and slower under QBO westerlies than easterlies. Note that this is inconsistent with observations, which seem to indicate that the MJO propagates faster under QBOW than QBOE (Nishimoto and Yoden, 2017), though, as noted by Son et al. (2017), stronger MJO events propagate more slowly across the Maritime Continent than weaker ones. The vertical energy flux is more or less equivalent across all z_c, but with largest magnitude of vertical energy flux for QBO easterlies than westerlies (not shown). Lower values of z_c do not lead to significant differences in growth rates, since the structure of the tropospheric mode is largely the same regardless of stratospheric mean wind. Higher values of z_c have lead to larger differences in growth rates across stratospheric westerlies and easterlies, but are not justifiable given the lack of ice concentration at those levels.

To understand why the growth rates are stronger under QBO easterlies than westerlies, we look at the phase relationship between s, s_m and q_c. Figure 4-14, bottom-left, shows the decomposition budget of the saturation entropy time-tendency equation on the equator, with $z_c = 17$ km. The terms that have the greatest change in phase relationship between easterly or westerly QBO winds are the cloud-radiative feedback terms, Cs_m and $C_r q_c$. In particular, during easterly QBO stratospheric winds, Cs_m and $C_r q_c$ are shifted to be more in phase with s (black line). This is significant since the more radiative heating anomalies are in phase with s, the larger the growth rate of the saturation entropy anomalies, and the faster the MJO-like propagates eastward. Note how q_c is eastward of s_m, which is equivalent to an eastward tilt with height in cloud fraction.

There are a few outstanding questions on whether modulation of cirrus clouds is a significant component in the apparent modulation of the MJO by the QBO. An important question to ask is if this mechanism generalizes to other equatorial waves? As shown by (Abhik et al., 2019), only the MJO, and perhaps the convectively coupled Kelvin wave, is modulated by the QBO. The convectively coupled Kelvin wave has a much weaker cloud-radiative feedback than the MJO, which could explain this

contradiction (Sakaeda et al., 2020). Furthermore, as alluded to in this study and easily shown from linear theory, equatorial Rossby waves flux very little energy into the stratosphere. As a result, dynamical forcing of cirrus clouds would be much smaller in equatorial Rossby waves. However, the seasonality of the MJO-QBO relationship cannot be explained by this mechanism. This casts a shadow of doubt over the importance of dynamical modulation of cirrus clouds by upward propagating equatorial waves.

Advection by the background wind

The second term on the RHS of Equation (4.33) represents the bulk zonal advection by a background wind of the cirrus clouds. To understand how to represent $\overline{U}_c$, we turn to re-analysis data. Figure 4-15 shows the tropical averaged (10°S-10°N), mean and anomalous zonal wind, separated into different seasons and easterly and westerly phases of the QBO. During boreal winter, there are upper tropospheric mean westerlies in the tropics, regardless of the QBO phase. The presence of upper tropospheric westerlies may advect cirrus clouds associated with MJO-convection eastward, leading to an eastward tilt with height. However, the strength of the tropical-averaged TTL westerlies are slightly weaker (around 1-1.5 m s^{-1}) during QBOW than QBOE. This is most evident in the deseasonalized zonal wind anomalies shown in Figure 4-15, right. During lower stratospheric westerlies (QBOW), easterly anomalies exist in the upper troposphere, while the opposite is true during lower stratospheric easterlies (QBOE). Differential advection of upper tropospheric cirrus clouds between QBO phases may play a role in modulating the strength of the MJO.

While it may be hard to believe that differences of 1 m s^{-1} can make large differences in MJO strength, the anomalies are not negligible with respect to the magnitude of the mean winds (which themselves are tropical averages). However, it is important to note that there are still upper tropospheric westerlies during MAM, and that the difference in the magnitude of the westerlies between QBOE and QBOW is larger than that during DJF ($\approx$ 1.5 m s^{-1}). This is at odds with the fact that the MJO-QBO relationship is only observed during boreal winter (Yoo and Son, 2016), though

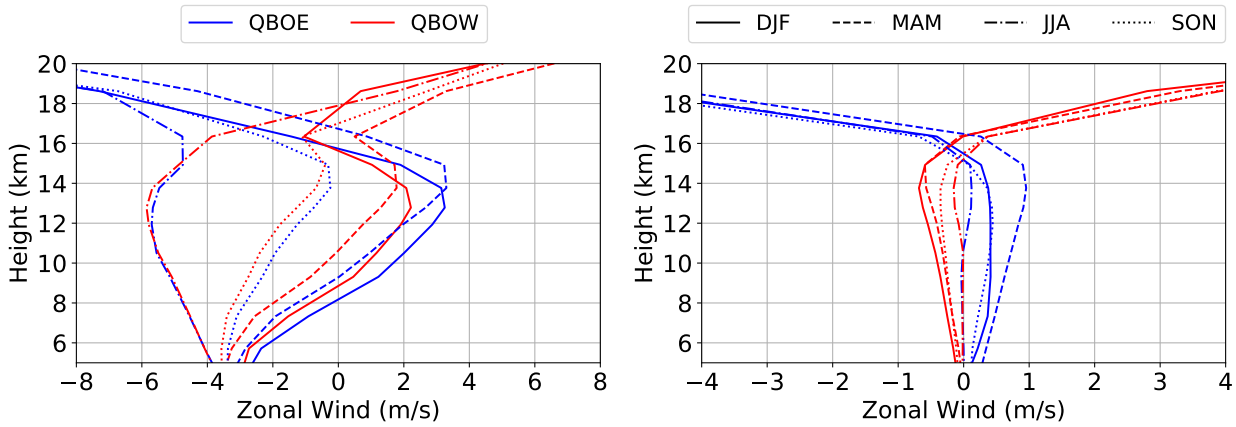

Figure 4-15: (Left) Tropical averaged (10°S-10°N) zonal wind, separated into (blue) easterly and (red) westerly phases of the QBO, as well (solid) DJF, (dashed) MAM, (dot-dashed) JJA, and (dotted) SON. (Right) Same as left but for deseasonalized, zonal wind anomalies. Zonal winds are calculated using 1979-2020 ERA5 re-analysis fields.

the seasonality of the strength of the MJO (the MJO being strongest in boreal winter) may also play a role (Zhang and Dong, 2004). During JJA and SON, there are pronounced upper tropospheric easterlies in the tropics; much of the easterly signal in the tropics is due to the presence of the upper tropospheric anticyclone associated with the South Asian monsoon.

The zonal wind profile in boreal winter leads us to parameterize $\overline{U}_c$ as follows:

$$\overline{U}_c = 0.1 - \overline{U}_s/10 \tag{4.39}$$

These choices are motivated by the fact that mean upper tropospheric winds are weak westerlies, but QBO-associated zonal wind anomalies are opposite signed of the QBO phase, albeit at a much smaller magnitude. Since the zonal winds that are opposite signed from the phase of the QBO occur right below the stratosphere ($14 - 16$ km), we will choose z_c from this range of values. Sensitivity tests to the exact form of the parameterization of zonal wind and z_c will be discussed.

Figure 4-16 shows the growth rate, frequency, and vertical energy flux associated with the $k = 1$ MJO-like mode, but now with the inclusion of weak zonal advection of cirrus clouds, according to Equation (4.39). Note that the dynamical modulation

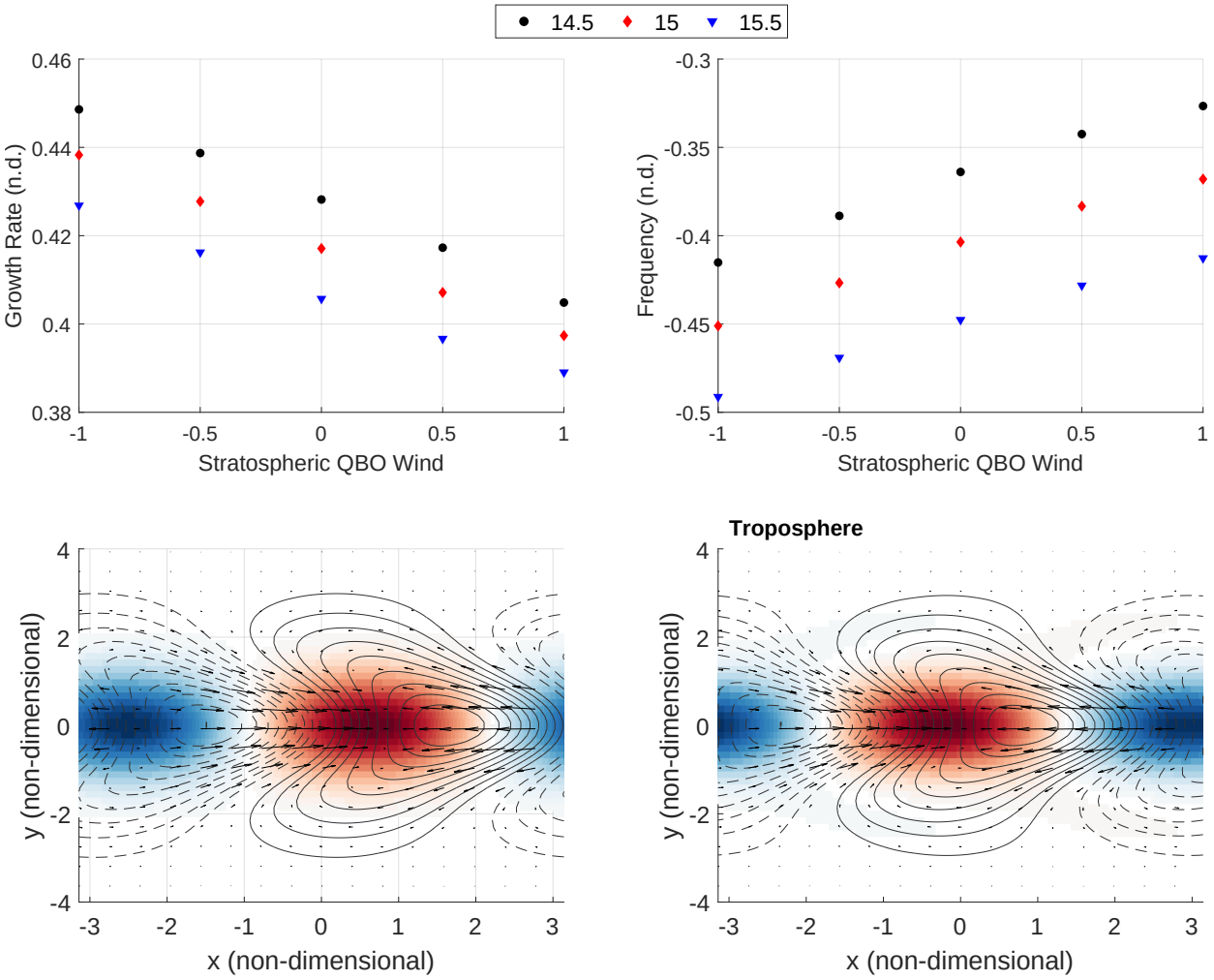

Figure 4-16: Same as Figure 4-14 but now including advection of cirrus clouds, using $\overline{U}_c = 0.1 - \overline{U}_s/10$.

of cirrus clouds must be retained to force q_c. In the linear model, $H = 16$ km, so we vary z_c from 14.5-15.5 km. In general, we see that growth rates are higher with upper tropospheric easterly advection (westerly QBO) as compared to westerly advection (easterly QBO). The differences in growth rates increase with the strength of advection, and the magnitude of these differences are largely the same across the range of z_c. Figure 4-16 also shows the tropospheric eigenmode of the cirrus-cloud modified MJO-like mode. Both modes still retain the familiar shape of an equatorial Kelvin wave lagged and flanked by a Rossby wave, though the polewards extent of the Rossby gyres is smaller than that in the control case (c.f. Figure 5-1). Anomalous westward advection of the cirrus cloud parameter shifts the phase offset of radiative heating perturbations to be more in-phase with s, similar to the effects described in the previous section (not shown). As a result, the mode grows faster and propagates faster under anomalous westward cirrus cloud advection. The opposite is true of eastward advection.

Sensitivity tests setting upper-tropospheric zonal advection to be same-signed as the QBO-phase show the same qualitative relationship of MJO strength with sign of the zonal advection: anomalous easterly advection in the upper troposphere leads to larger growth rates (not shown). Since the background wind at levels above 16 km are the same-sign as the QBO-phase, anomalous zonal advection above $z_c = 16$ km would lead to a stronger MJO under westerly QBO, contrary to what is observed. We also performed experiments changing the relative magnitude of C and C_r. We found that increasing C_r (and compensating with decreases to C) slows down the phase speed of the MJO-like mode and changes the horizontal structure of the MJO-like mode (mostly by modifying the structure of the Rossby gyres), but does not qualitatively change the results discussed in this section.

4.5 Summary and discussion

In order to better understand the effect of the stratosphere on the MJO, the linear model of Lin and Emanuel (2022) was extended in this study to include a non-

zero mean wind in the stratosphere and a prognostic equation for cirrus clouds. We specifically focus on how an MJO-like mode in the linear system interacts with the stratosphere, through wave propagation into the stratosphere or modulation of cirrus clouds, which are forced dynamically and allowed to be advected by the background zonal wind. Radiative heating associated with cirrus clouds modifies the MJO-like mode. The behavior of the MJO-like mode was analyzed under a variety of zonal wind profiles in the stratosphere, from simple forms of constant winds, to more realistic, QBO-like oscillations in zonal wind. As in Lin and Emanuel (2022), a numerical model is used to solve for growth rate and phase speed of the MJO-like mode by integrating the equations forward in time. The main findings of the study are summarized below:

- The MJO-like mode systematically has a higher vertical energy flux during stratospheric easterlies than stratospheric westerlies (regardless of the pattern). This is because the Kelvin-wave-like component of the mode fluxes more energy into the stratosphere under easterlies, and is suppressed under westerlies. While the Rossby-wave component of the MJO mode fluxes more energy upwards under westerlies, it does not make up for lost energy flux from the suppressed Kelvin wave. These results are qualitatively consistent with linear wave theory.

- Under constant mean zonal wind in the stratosphere and zero zonal wind in the troposphere, the MJO-like mode is weaker under statospheric westerlies than easterlies, consistent with the observed relationship. This is not due to differences in upward wave radiation, but rather phase-shifting of the barotropic mode with respect to the baroclinic mode. When the barotropic mode is more in-phase with the baroclinic mode, the surface wind speed is larger and enhances the WISHE feedback. Limits on the realism of this mechanism are discussed at length. When phase shifting of the barotropic mode is removed, the MJO-like mode has larger growth rates under stratospheric easterlies than westerlies.

- MJO-associated westward (eastward) tilts with height under westerlies (easterlies), as shown by Hendon and Abhik (2018), can be explained by upward propagating Rossby (Kelvin) waves associated with the MJO.

- Eastward tilts with height in MJO-associated ice cloud fraction are observed above ≈ 14 km, near the equator, from CALIP cloud occurrence profiles. The eastward tilt with height could be explained through dynamical forcing via upward propagation of the Kelvin wave, or eastward advection by the mean zonal flow in the upper troposphere.

- A cirrus-cloud prognostic equation that parameterizes the anomalous radiative heating effect of cirrus clouds on the troposphere was developed. In particular, it is shown that dynamical modulation of cirrus clouds by upward propagating waves in the lower stratosphere can modify radiative heating anomalies to be more in-phase with tropospheric saturation entropy anomalies under stratospheric easterlies, enhancing the growth rate of the MJO-like mode. This mechanism, however, cannot explain the seasonality of the MJO-QBO relationship.

- Tropical-averaged upper-tropospheric zonal winds are shown to be mean westerly during boreal winter, but anomalously westerly (easterly) under QBOE (QBOW). The influence of anomalous advection of cirrus clouds by the background flow is investigated by including zonal advection in the cirrus-cloud prognostic equation. It is shown that QBOE-associated anomalous westerly zonal advection in the upper troposphere also enhances the growth rate of the MJO-like mode, by shifting the phase of radiative heating to be more in phase with saturation entropy anomalies.

While this study focused on the $k = 1$ MJO-like mode, we also investigated the aforementioned mechanisms in the $k = 2$ (and higher) MJO-like modes, and the results are worth mentioning here. In general, the MJO-like modes propagate more slowly as the horizontal wavenumber increases, and hence the magnitude of both the barotropic mode and wave energy loss to the stratosphere decreases with zonal wavenumber (Lin and Emanuel, 2022). This means that the differences in growth rates between stratospheric easterlies or westerlies are diminished when only considering changes to the vertical energy flux. We also performed experiments looking at differences in growth rates from modulation of the cirrus-cloud feedback. Dynamical

modulation of cirrus is reduced for the smaller scale MJO-like modes, since the dynamical forcing (w) is smaller in magnitude than the dynamical forcing for the $k = 1$ mode. On the other hand, modulation of the growth rates of the MJO-like mode through zonal advection in the upper troposphere is still significant for the smaller scale MJO-like modes.

The linear model formulated in this study serves as a step towards better understanding tropospheric-stratospheric coupling in the tropics. One may rightfully question the extent to which linear models can capture the true relationship between the MJO and QBO. Non-linear wave dynamics and wave-breaking at critical layers, which our linear model fails to resolve, might be important components of the MJO-QBO relationship. After all, the QBO owes its existence to momentum transfer to the mean flow from breaking upward propagating waves (Lindzen and Holton, 1968). There is also some evidence that upward propagating waves in the lower stratosphere often become disconnected from the space-time forcing of the troposphere, which would invalidate assumptions of linearity (Yang et al., 2012).

One may also hesitate at our simple parameterization of cirrus clouds, which only considers a single level z_c to be of importance for cirrus cloud radiative feedbacks. In reality, the net radiative forcing by high-clouds is a complex, non-linear function of optical depth and cloud-top height (Fu et al., 2002). As such, radiative heating perturbations are better represented using depth-integrated quantities, which we neglected in the spirit of simplicity. The results in this study may be sensitive to this behavior.

When modeling complex phenomena in the atmosphere, it is often necessary to make simplifying assumptions to make tractable progress on understanding the underlying dynamics. Thus, the results of this theoretical study should be viewed through a lens of skepticism. But, the interpretations could prove to be a useful guide for high-resolution modeling experiments. This will be the subject of future work.

Chapter 5

Conclusion

5.1 Summary

While this thesis compiles my contributions to scientific knowledge, it also represents my growth as a scientist throughout my time in graduate school. While Chapter 2 represents applied work in tropical meteorology, I later transitioned to more theoretical atmospheric science, by using simple linear models to understand tropospheric-stratospheric interactions in Chapters 3 and 4.

In Chapter 2, I created a large-ensemble probabilistic tropical cyclone forecast model, called Forecasts of Hurricane using Large-ensemble Outputs (FHLO). The primary novel aspect of this model was to incorporate state-dependent uncertainty into a tropical cyclone forecast by sampling the internal variability of ensemble NWP models. FHLO acts as an ensemble model bootstrapper, generating a potentially infinite number of tracks that are statistically indistinguishable from ensemble NWP forecasts of tropical cyclone tracks, and then determining the intensity of the tropical cyclone along that track through a zero-dimensional intensity model (Emanuel, 2017). An axisymmetric wind profile with an asymmetric correction are fit along the track to determine the full radial wind speed profile of the tropical cyclone (Chavas et al., 2015). In our study, FHLO was validated using tropical cyclones in the Atlantic and Eastern Pacific, from the 2015-2018 seasons, using a 1000-member ensemble. At lead-times greater than three days, point-wise wind forecasts using the FHLO

framework were shown to generally have higher threat scores than point-wise wind forecasts derived from the National Hurricane Model. More importantly, a simple average between FHLO and the NHC's point-wise wind speed forecast model outperformed both individual models, at all lead times and all wind speed thresholds in the Atlantic basin. These efforts show that incorporating state-dependent uncertainty is important to improve probabilistic tropical cyclone forecasts at lead-times greater than 3 days (whereas improving initial conditions are important to improve forecasts with shorter lead-times). FHLO runs semi-operationally, in real-time at the National Center for Atmospheric Research (NCAR), and the results are disseminated to the public at https://tcs.mit.edu/.

In Chapter 3, I formulated a linear model to understand how surface friction and interaction with the stratosphere modifies equatorial waves. The study was motivated particularly by how the barotropic can be excited (and coupled to) the baroclinic mode through either stratospheric coupling and/or surface friction. I coupled a strict quasi-equilibrium troposphere with a dry, passive stratosphere, and analyzed the eigenmodes of the coupled system. I extended the results of Yano and Emanuel (1991) and found that in addition to Kelvin-waves, east-ward propagating Yanai waves and inertia-gravity waves are strongly modified by the stratosphere: these waves grow in the troposphere and propagate wave-energy upwards, but the vertical group velocity becomes exceedingly large for smaller scale waves, leading to dampening of growth rates at smaller scales. Waves that propagate slower, such as Rossby waves and MJO-like disturbances, do not interact with the stratosphere much, and their growth rates are not significantly modified from their rigid-lid counterparts. In addition, I found that as the stratosphere stratification decreases, more energy is lost to the stratosphere, further dampening small scale tropospheric waves. I also showed that surface friction acts purely as a dampening mechanism, acting equally across all spatial scales. Interestingly, I also show that when the barotropic mode is excited through surface friction, it exhibits non-zero values far away from the equator. The long-tail behavior of the barotropic mode is modulated by the stratospheric stratification. Under a highly stratified stratosphere, the barotropic mode becomes trapped

in the troposphere, and has a significant poleward extent. As the stratosphere stratification is reduced, the poleward extent of the barotropic mode reduces, as more energy leaks into the stratosphere. I hypothesized that this might be a mechanism through which teleconnections between the tropics and extratropics are established.

In Chapter 4, I extended the linear model of Chapter 3 to non-zero stratospheric winds, in order to investigate how stratospheric circulations (like the QBO) can affect the MJO. I looked at two specific hypothesis: (1) how the stratosphere modulates the amount of energy that is lost to the stratosphere via upward wave radiation, and (2) how the stratosphere modulates cloud-radiative feedbacks. Under linear dynamics, I found that when there is a jump in zonal wind across the tropopause, the barotropic mode becomes phase-shifted with respect to the baroclinic mode. This phase-shifting leads to a stronger WISHE effect under easterly flow than westerly flow, leading to a stronger MJO under easterly than westerly stratospheric flow, consistent with the MJO-QBO relationship. When the barotropic-mode phase shifting is removed by gradually varying the stratospheric wind speed, the effect of energy loss via upward wave radiation takes over. Wave-energy loss to the stratosphere is strongest under easterly flow, since the Kelvin wave (which propagates upwards under easterly flow) radiates more strongly than the Rossby wave (which propagates upwards under westerly flow). I also investigated how the stratosphere modulates thin cirrus clouds. Observations of ice cloud concentration in the upper troposphere/lower stratosphere indicate an eastward tilt with height with respect to tropospheric convection. The eastward tilt with height is hypothesized to be a function of either the upward propagating Kelvin wave, or westerly zonal advection. These two processes are incorporated in the linear model, by including a prognostic equation for ice concentration. Cirrus clouds are allowed to be dynamically modulated by upward propagating waves (which are influenced by the stratospheric wind), and advected by the background zonal flow. Advection is assumed to occur in the upper troposphere, where zonal wind anomalies are opposite signed of the QBO phase (for instance, there are weak easterly anomalies in the tropics associated with westerly phase of the QBO). I showed that both processes lead to a stronger MJO under easterly QBO flow. Under easterly QBO

flow, ice clouds (and hence cloud-radiative heating) are shifted to be more in-phase with entropy anomalies in the troposphere, leading to a stronger MJO. I also discuss caveats of the linear framework, especially with regards to the seasonality of the MJO-QBO relationship.

5.2 Future Work

While a Ph.D. must be finite in time, one's quest to understand and discover the natural world is not. While I have learned a great deal working on the contents of this thesis, I have also entered with more questions than answers. Therefore, I will close with a few follow-up thoughts to the results that I have presented throughout this thesis.

5.2.1 Follow up to Chapter 2

There are a couple of natural follow up questions to the work described in Chapter 2. In particular, we ask, **what is the predictability limit of tropical cyclone wind speeds at a fixed point in space? Moreover, what are the dynamics that control the uncertainty in point-wise wind speed forecasts?** These questions may be able to be answered using FHLO in an idealized, perfect-model approach, to which we introduce below.

Let $V_i(\lambda, \phi)$ be the forecasted maximum wind speed from ensemble member i, at a longitude of λ and latitude of ϕ. We define the ensemble mean energy, $E(\lambda, \phi)$ as:

$$E(\lambda, \phi) = \frac{1}{N} \sum_{i}^{N} [V_i(\lambda, \phi)]^2 \tag{5.1}$$

and the ensemble error energy, $e(\lambda, \phi)$, as:

$$e(\lambda, \phi) = \frac{1}{N} \sum_{\Omega} [V_i(\lambda, \phi) - V_j(\lambda, \phi)]^2 \tag{5.2}$$

where N is the total number of ensemble members, $1 \leq i \leq N$, $1 \leq j \leq N$, and Ω is

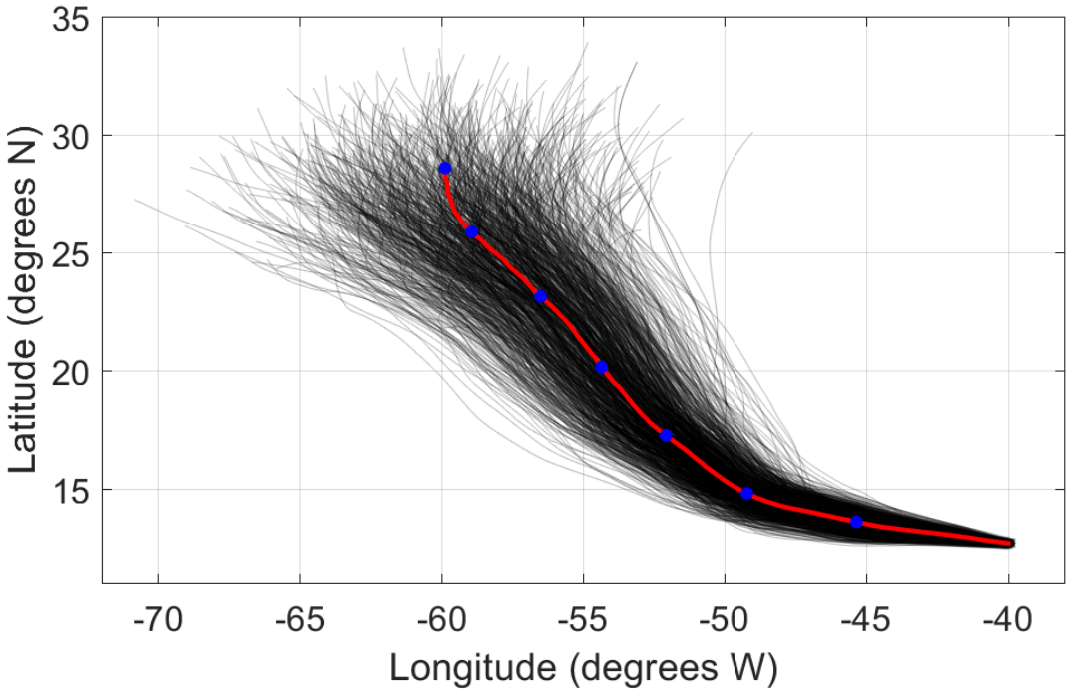

Figure 5-1: Example of selection of points in a large ensemble of tropical cyclone tracks. Black lines are 1000 synthetic tracks generated from FHLO. Red line is the median (in time) of all of the tracks. Blue points show the median forecasted position from days 1-7, in 1-day increments.

the set that includes all pairs $\{i, j\}$ where $i \neq j$. The ensemble error energy ratio is defined as:

$$R(\lambda, \phi) = \frac{e(\lambda, \phi)}{E(\lambda, \phi)} \tag{5.3}$$

In classical studies of predictability, loss of predictability is generally defined as when the ensemble error energy ratio is equal to 1, or when differences in a quantity between ensemble members are greater than the amplitude of the same quantity averaged across the ensemble members (Judt et al., 2016).

FHLO outputs point-wise maximum wind speeds from 1000 ensemble members. The wind speeds are a vector combination of forecasted winds from a tropical cyclone, as well as the forecasted winds from the large-scale environment. This allows the total energy to grow in time (and hence the error energy ratio to be well defined), since the background environmental winds become less predictable with increasing lead time. We can calculate the error energy ratio of the maximum wind speed at fixed points

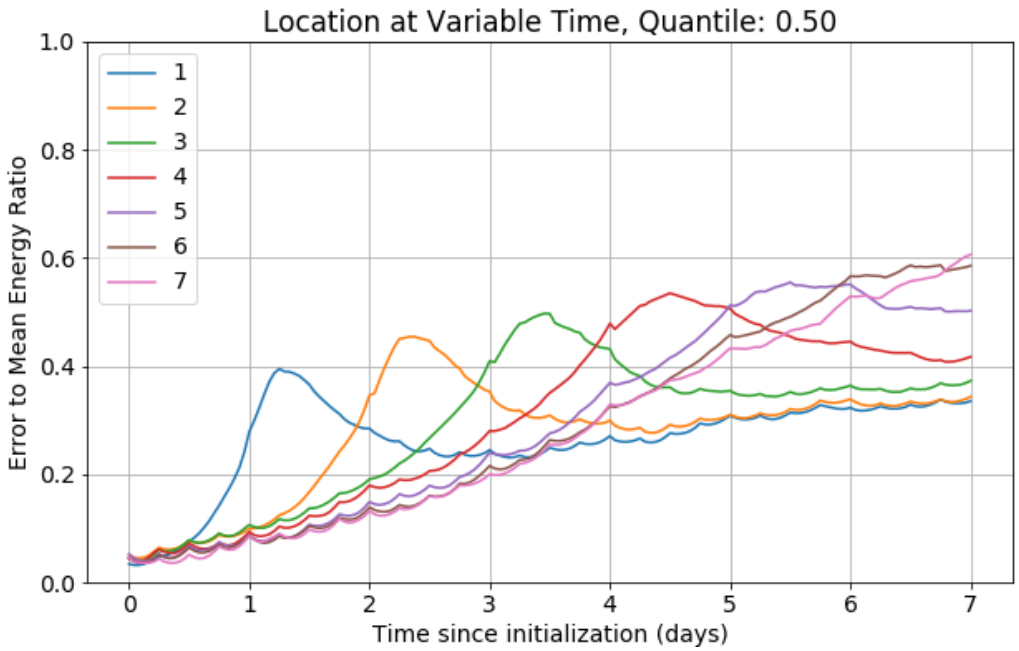

Figure 5-2: Ensemble error energy ratio, for points that are 1- to 7-days along the median forecasted track. Samples include 2015-2018 Atlantic and Eastern Pacific tropical cyclone forecasts.

in space, as a function of time. To investigate the predictability of point-wise wind speeds from tropical cyclones, we must first define points along the tropical cyclone path. As a first pass, we select points that are along the median of the ensemble tracks. The points are selected based on lead-time from the forecast initialization [see Figure 5-1]. Figure 5-2 shows the error to mean energy ratio, as a function of lead-time, for points along the median of the ensemble tracks. It is evident that the the error to mean energy ratio locally peaks around the time each point was selected along the median of the tracks. In addition, we also see a slow increase in the error to mean energy ratio in time, due to natural loss of predictability of the environmental winds. The error to mean energy ratio, however, does not saturate in the 7-day forecast time period, and appears to slow in growth in days 5-7. These results seem to suggest that for locations at the center of a forecast cone, there is predictability beyond 7-days, though these preliminary results should not be considered conclusive: it is quite possible that the model is underdispersive at long time scales, under-representing the uncertainty. As of now, 7-day forecasts of tropical cyclones are not yet routinely

available, and it is still unclear whether there is any practical predictability at those time scales.

There is still much more work to be done. How does the predictability limit change for points that are further away from the center, or near the edges? In addition, extending the forecasts to 10-day lead times could provide insight into whether the error to mean energy ratio continues to grow past 7 days. In addition, since FHLO is modular, it is possible to diagnose what component of the model is leading to uncertainty (and/or loss of predictability). For instance, we will run experiments completely removing (1) track spread, (2) internal variability, (3) initial conditions, and combinations there-in, to investigate the effect each of these has on the forecast uncertainty. The results of these experiments may be able to provide guidance on what modelers should focus on improving in order to reduce tropical cyclone uncertainty, if it is at all practical.

5.2.2 Follow up to Chapter 3 and 4

While idealized linear models serve as useful hypothesis testers, they, by definition, cannot resolve complex, non-linear interactions. **Do the results of the linear model hold up in more complex numerical models?** To this end, we have planned idealized, numerical modeling experiments on global aquaplanet configurations to validate the results of the linear model.

We will validate and interpret the results of the linear model using the System for Atmospheric Modeling (SAM), a non-hydrostatic cloud-resolving model (CRM). Idealized CRM simulations and mechanism-denial experiments will allow us to represent a more complex system without obscuring key mechanisms by attempting to emulate the real world. Using SAM, Khairoutdinov and Emanuel (2018) conducted simulations initialized from a radiative-convective equilibrium (RCE) state on a rotating sphere with walls around 46° latitude and constant SST, and found that a wide-variety of equatorial waves developed, as well as a planetary scale, slowly eastward-propagating, MJO-like disturbance, despite a coarse horizontal grid (20-km) and the absence of a convective parameterization. Shorter experiments with 4-km horizontal

resolution did not find significant differences from the 20-km experiments (Khairoutdinov and Emanuel, 2018). The relatively simplistic conditions under which equatorial waves and the MJO-like disturbance form make this aqua-planet RCE configuration ideal for understanding the mechanisms through which the equatorial disturbances might interact with the stratosphere.

We plan to carry out 300-day experiments using the same configuration. However, we will run experiments in which (1) the stratification in the stratosphere is nudged towards a pre-determined value, and the (2) mean wind in the tropical stratosphere is nudged towards a pre-determined profile. The first set of experiments will vary the target value of stratospheric stratification, to confirm if the stratosphere indeed has a role in selecting for certain scales in the troposphere. The second set of experiments will follow the nudging methodology performed in Martin et al. (2021b). We first plan to nudge the zonal-mean zonal winds in the upper troposphere and stratosphere towards a state of mean easterly, or mean westerly winds in the stratosphere. Nudging should interfere minimally with model dynamics. We will then gradually vary the strength of nudging from the upper troposphere into the stratosphere.

In the experiments ran by Khairoutdinov and Emanuel (2018), a Newtonian damping layer was placed in the upper third of the domain (starting around 23 km), which, for our purposes, is too close to the model's cold-point tropopause (15 km). In order to better resolve tropospheric-stratospheric interaction, we will increase the top of the domain to 45 km, which will increase the level of the damping layer to 30 km. This will increase the computational cost of experiments, but estimations of computational requirements are within reasonable bounds ($\approx$30,000 core hours). However, since SAM compensates for high vertical resolution in the boundary layer ($\approx$100 m) with lower vertical resolution ($\approx$1.5 km) in the stratosphere, we will perform sensitivity tests by running shorter experiments with increased stratospheric vertical resolution. These experiments will help determine the sensitivity of the results to model vertical resolution.

To estimate the magnitude of upward wave radiation and subsequent energy loss to the stratosphere in our different experiments, we will perform calculations of Eliassen-

Palm-fluxes associated with various equatorial waves and the MJO, by filtering dynamical fields to contain only the desired waves (Eliassen and Palm, 1960). Other metrics, such as the vertical energy flux, will also be computed to estimate the amount of wave energy lost to the stratosphere (Matsuno, 1970; Andrews et al., 1987). To estimate modulation of cloud-radiative effects by the stratosphere, through either zonal advection or dynamical modulation via upward propagating waves, we will use moist-static energy budget analyses (Sobel et al., 2014). Vertical composites of the wavenumber 1 disturbance will also be constructed to compare how the vertical tilt in ice cloud concentration in the upper troposphere/lower stratosphere is modified by the stratosphere.

5.2.3 Steady solutions in the tropics

The time-dependent problems of Chapters 3 and 4 admit zonally propagating, growing/decaying, wave-like solutions, for which there are strong analogies in the real tropical atmosphere. But what about the steady, geostrophic adjustment problem in the tropics?

Suppose there is a steady, meridionally decaying SST anomaly, centered on the equator (in fact, quite a common occurrence in the tropics). Geostrophic adjustment will occur, and on long enough time scales, a thermal-wind response will be induced, leading to upper tropospheric anticyclonic potential vorticity anomalies where the SST gradients are the largest. The anticyclonic PV anomalies must have a signature in the stratosphere. In fact, classical PV inversion tells us that cold anomalies will exist above the anticyclone. In the stratosphere, these cold anomalies are balanced by radiative heating and upwelling. To what extent can this process explain upwelling in the shallow, tropical branch of the Brewer Dobson circulation?

Figure 5-3 shows the linear, steady response to a steady, meridionally decaying, sea surface temperature anomaly centered on the equator, in a modified form of the linear model described in Chapters 3 and 4. There is a modest amount of surface friction and a small amount of meridional diffusion, but neither radiative relaxation nor wave-drag in the stratosphere. There is a thermal wind response, as mentioned earlier, and

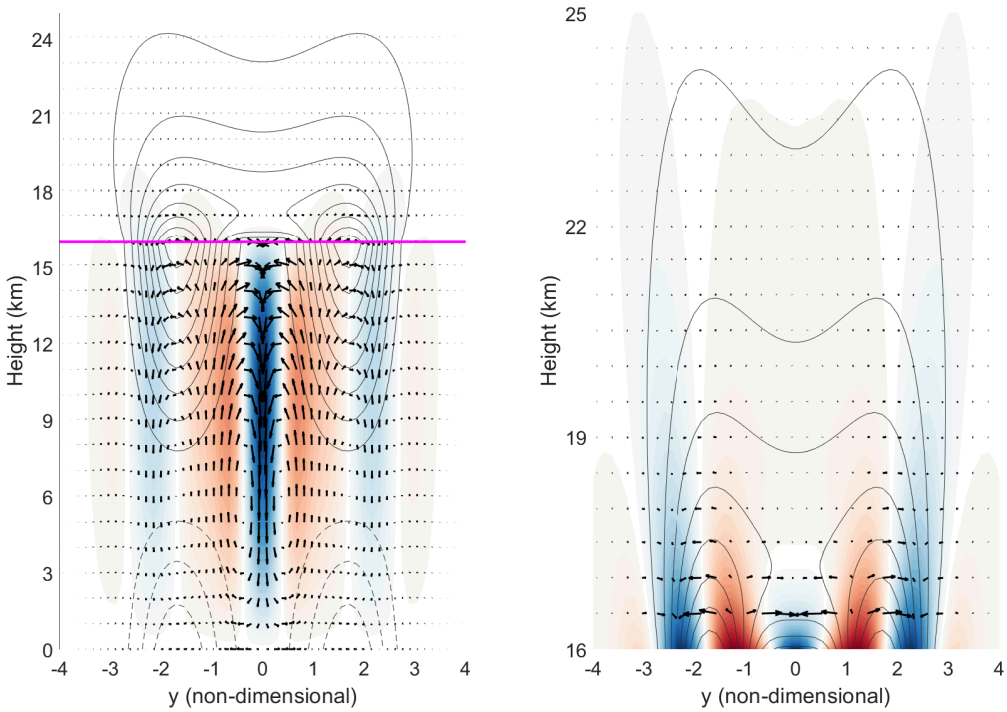

Figure 5-3: (Left) Linear, steady response to a steady, meridionally decaying, sea surface temperature anomaly centered on the equator. Contours are zonal wind anomalies (solid for westerlies, negative for easterlies), shadings are vertical velocity anomalies, and arrows show the meridional-vertical circulation. (Right) Same as left but magnified in the lower stratosphere.

a "double ITCZ"-like circulation response in the tropics. In the stratosphere, however, there seems to be a shallow meridional-vertical circulation in the subtropics (around $y = 1$ to $y = 2$), as well as a much deeper, but also weaker upwelling branch near the equator.

There are quite a number caveats: for one, there is nothing to balance temperature anomalies in the stratosphere except diffusion. This is not realistic, and the results may change greatly with radiative relaxation. In addition, rising motion does not occur forever. In the tropical stratosphere, there may be a delicate balance between wave-drag (driving the tropical air polewards) and upwelling, which determines the height to which air can rise before it moves polewards. And, of course, the response in the stratosphere can be non-linear. Regardless, this mechanism may shed some light on whether or not "upwards-control" is valid in the tropics.

Appendix A

Technical Aspects of FHLO

A.1 Inversion on a Low-Resolution Grid

In FHLO, we have to remove winds associated with the TC by performing “vortex surgery" on both the ERA5 analysis fields and the forecast ensemble fields, as in Davis et al. (2008). While the analysis fields can be obtained at high grid resolution, the grid resolution (0.5°) of ensemble numerical weather prediction models is inadequate to properly resolve the vorticity maxima of a TC. One way around this is to interpolate between grid points. However, interpolation schemes must always assume some structure about the field (i.e. linear, cubic, etc). Using spherical harmonics, we can extend the number of basis functions to an arbitrary higher order by assuming that the power spectrum obeys a well-defined scaling law. Defining L as the truncation order of the original field, L' as the truncation order of the higher resolution field, $S(l')$ the desired power at degree l', and n a random coefficient with unit variance, then, the super-resoluted field f is:

$$f(\theta,\phi) = \sum_{l=0}^{L}\sum_{m=-l}^{l} f_l^m Y_l^m(\theta,\phi) + \sum_{l'=l+1}^{L'}\sum_{m'=-l'}^{l'} \left[\sqrt{S(l')}n\right] Y_{l'}^{m'}(\theta,\phi)$$

where S is determined from the power spectrum at the extended spherical harmonics. For simplicity, we use an exponentially decaying fit to the power spectrum, and use the fit to extend to higher order of harmonics. Note that this smooth interpolation can also be performed without assuming any structure about the power spectrum, as long as the original resolution is high enough such that the amplitudes of the higher order spherical harmonics are sufficiently small. In fact, we can even set the power of the higher-order spherical harmonics to zero with relatively little consequence on the resulting environmental wind fields.

A.2 Perturbations to Observed Intensity

In order to generate perturbations to the observed intensity, we model the intensity, $V(t)$, as a Gaussian process with the time-varying observations as the mean and a constant covariance kernel:

$$C_V(t_1, t_2) = \sigma_V^2 \exp(-|t_1 - t_2|/T)$$

where t_1 and t_2 are discrete time points in the observed history, $T = 1$ day, and σ^2 is the variance that represents the uncertainty associated with the observations. We write the Karhunen-Loeve expansion of the intensity as $V(t) = \mu_V(t) + \Sigma_{i=1}^{n} \sqrt{\lambda_i} \psi_i \theta_i$, where n is the total stochastic dimension, θ_i is a standard normal random variable, and λ_i and ψ_i are the ordered eigenvalues and eigenvectors with respect to the covariance kernel C_V. We only consider fluctuations of the intensity on time scales of the observations (every 6 hours), such that we take $n = 10$ to remove any high-frequency variability. Finally, we take σ_v^2 as a piecewise constant function:

$$\sigma^2(v) = \begin{cases} 5 & \text{if } v < 32 \text{ m s}^{-1} \\ 10 & \text{if } v \geq 33 \text{ m s}^{-1} \end{cases}$$

where v is the observed intensity. These values of $\sigma^2(v)$ were chosen as simple approximations to the uncertainty distributions shown in Landsea and Franklin (2013).

Appendix B

Details of the Linear Framework

B.1 Non-dimensionalization

Here, we define the non-dimensional scalings for the variables that appear in the full linear model. The scalings for the tropospheric quantities $s^{*\prime}$, s'_m, χ, α, γ, D and G are identical to those described in the appendix of KE18.

$$x \to ax \tag{B.1}$$

$$y \to L_y y \tag{B.2}$$

$$p \to (p_s - p_t)\hat{p} \tag{B.3}$$

$$z^* \to H z^* \tag{B.4}$$

$$t \to \frac{a}{\beta L_y^2} t \tag{B.5}$$

$$L_y^4 \to \frac{\Gamma_d}{\Gamma_m} \frac{d\overline{s}_d}{dz} (T_b - [\overline{T}]) H \frac{1 - \epsilon_p}{\beta^2} \tag{B.6}$$

$$u' \to \frac{aC_k|\overline{\mathbf{V}}|}{H} u' \tag{B.7}$$

$$v' \to \frac{L_y C_k|\overline{\mathbf{V}}|}{H} v' \tag{B.8}$$

$$w^{*\prime} \to C_k|\overline{\mathbf{V}}| w^{*\prime} \tag{B.9}$$

$$\phi' \to \frac{a\beta L_y^2 C_k|\overline{\mathbf{V}}|}{H} \phi' \tag{B.10}$$

$$\omega \rightarrow \frac{C_k \overline{\mathbf{V}}(p_s - p_t)}{H}\omega \tag{B.11}$$

$$N^2 \rightarrow \frac{\beta^2 L_y^4}{H^2} S \tag{B.12}$$

$$F \rightarrow \frac{aC_d|\overline{\mathbf{V}}|}{\beta L_y^2 h_b} \tag{B.13}$$

$$\overline{U}_s \rightarrow \beta L_y^2 U_s \tag{B.14}$$

$$\eta \rightarrow \frac{aC_k|V|}{\beta L_y^2}\eta \tag{B.15}$$

$$T \rightarrow \frac{\beta^2 L_y^4}{R_d} T \tag{B.16}$$

where most dimensional parameters are described in the main text and in KE18. Parameters not defined in this text are the mean radius of the Earth a, the dry adiabatic lapse rate γ_d, the moist adiabatic lapse rate γ_m, the dry entropy stratification $\frac{d\overline{s}_d}{dz}$, the precipitation efficiency ϵ_p, and the enthalpy exchange coefficient C_k. The terms on the left of the arrow are the dimensional quantities, and those on the right are the non-dimensional quantities.

B.2 Numerical Model

The full mathematical description of the numerical system (including damping terms) is below:

$$\frac{\partial u_0}{\partial t} = -ik\big[\phi_s + V_1(\hat{p}_t)s^*\big] + yv_0 - 2F(u_0 + u_1) - ru_0 \tag{B.17}$$

$$\frac{\partial v_0}{\partial t} = \delta_x\Big[-\frac{\partial}{\partial y}\big[\phi_s + V_1(\hat{p}_t)s^*\big] - yu_0\Big] - F(v_0 + v_1) - rv_0 \tag{B.18}$$

$$\frac{\partial u_1}{\partial t} = iks^* + yv_1 - 2F(u_0 + u_1) - ru_1 \tag{B.19}$$

$$\frac{\partial v_1}{\partial t} = \delta_x\Big[\frac{\partial s^*}{\partial y} - yu_1\Big] - F(v_0 + v_1) - rv_1 \tag{B.20}$$

$$\frac{\partial s^*}{\partial t} = (1 + C)s_m - w - \alpha(u_0 + u_1) - \chi s^* - rs^* \tag{B.21}$$

$$\gamma\frac{\partial s_m}{\partial t} = -Ds^* - \alpha(u_0 + u_1) - Gw + Cs_m - rs_m \tag{B.22}$$

$$w = -ik(u_0 + u_1) - \frac{\partial}{\partial y}(v_0 + v_1) \tag{B.23}$$

$$\frac{\partial u_s}{\partial t} = -ik\phi_s + yv_s - ru_s \tag{B.24}$$

$$\frac{\partial v_s}{\partial t} = \delta_x\Big[- \frac{\partial \phi_s}{\partial y} - yu_s\Big] - rv_s \tag{B.25}$$

$$\frac{\partial \phi_s}{\partial t} = -\int_{\infty}^{z} w_s^* S \, dz^* - r\phi_s \tag{B.26}$$

$$\rho_s w_s^* = -B\Big(iku_0 + \frac{\partial v_0}{\partial y}\Big) - \int_{z^*=1}^{z} \Big[\rho_s\Big(iku_s(y,z^*) + \frac{\partial}{\partial y}v_s(y,z^*)\Big)\Big]dz^* \tag{B.27}$$

$$\frac{\partial q_c}{\partial t} = w_s^*(z^* = z_c) - \overline{U}(z^* = z_c)\frac{\partial q_c}{\partial x} \tag{B.28}$$

$$\tag{B.29}$$

where all variables are defined in the main text with the exception of r, which is the sponge coefficient for the sponge layer that is applied at the boundaries of the domain.

The spectral filtering is important to prevent any small scale, undesired noise from dominating the domain, and to ensure the isolation of the mode of interest. The spectral filter, $\hat{F}(l)$ is highly selective for only the largest wavenumbers, which contain almost all of the energy for the large-scale modes:

$$\hat{F}(l) = -\frac{1}{2}\tanh\Big(\Big|\frac{l}{2.5}\Big| - 9.5\Big) + \frac{1}{2} \tag{B.30}$$

where l is the meridional wavenumber. At the end of every time step, the time tendency of each prognostic variable is transformed to Fourier space and multiplied by $\hat{F}(l)$. The time tendency of the prognostic variables is then re-transformed back into physical space (y). The constants in the spectral filter were carefully tuned over experimentation.

Bibliography

Abhik, S., and H. H. Hendon, 2019: Influence of the QBO on the MJO during coupled model multiweek forecasts. *Geophysical Research Letters*, **46 (15)**, 9213–9221.

Abhik, S., H. H. Hendon, and M. C. Wheeler, 2019: On the sensitivity of convectively coupled equatorial waves to the quasi-biennial oscillation. *J. Climate*, **32 (18)**, 5833–5847.

Adames, Á. F., and D. Kim, 2016: The MJO as a dispersive, convectively coupled moisture wave: Theory and observations. *J. Atmos. Sci.*, **73 (3)**, 913–941.

Adames, Á. F., and J. M. Wallace, 2014: Three-dimensional structure and evolution of the vertical velocity and divergence fields in the MJO. *J. Atmos. Sci.*, **71 (12)**, 4661–4681.

Ahmed, F., J. D. Neelin, and Á. F. Adames, 2021: Quasi-Equilibrium and Weak Temperature Gradient Balances in an Equatorial Beta-plane Model. *J. Atmos. Sci.*, **78 (1)**, 209–227.

Andrews, D. G., J. R. Holton, and C. B. Leovy, 1987: *Middle atmosphere dynamics*. 40, Academic press.

Arakawa, A., and W. H. Schubert, 1974: Interaction of a cumulus cloud ensemble with the large-scale environment, Part I. *J. Atmos. Sci.*, **31 (3)**, 674–701.

Baldwin, M., and Coauthors, 2001: The quasi-biennial oscillation. *Rev. Geophys.*, **39 (2)**, 179–229.

Betts, A. K., 1982: Saturation point analysis of moist convective overturning. *J. Atmos. Sci.*, **39 (7)**, 1484–1505.

Boehm, M. T., and J. Verlinde, 2000: Stratospheric influence on upper tropospheric tropical cirrus. *Geophys. Res. Lett.*, **27 (19)**, 3209–3212.

Booker, J. R., and F. P. Bretherton, 1967: The critical layer for internal gravity waves in a shear flow. *J. Fluid Mech.*, **27 (3)**, 513–539.

Bougeault, P., and Coauthors, 2010: The THORPEX interactive grand global ensemble. *BAMS*, **91 (8)**, 1059–1072, doi:10.1175/2010BAMS2853.1.

Bryan, G. H., 2008: On the computation of pseudoadiabatic entropy and equivalent potential temperature. *Mon. Wea. Rev.*, **136 (12)**, 5239–5245, doi:10.1175/2008MWR2593.1.

Chao, W. C., and B. Chen, 2001: The role of surface friction in tropical intraseasonal oscillation. *Mon. Wea. Rev.*, **129 (4)**, 896–904.

Charney, J., and P. Drazin, 1961: Propagation of planetary-scale disturbances from the lower into the upper atmosphere. *J. Geophys. Res.*, **66 (1)**, 83–109.

Chavas, D. R., and K. Emanuel, 2010: A QuikSCAT climatology of tropical cyclone size. *Geophys. Res. Lett.*, **37 (18)**, doi:10.1029/2010GL044558.

Chavas, D. R., and N. Lin, 2016: A model for the complete radial structure of the tropical cyclone wind field. Part II: Wind field variability. *J. Atmos. Sci.*, **73 (8)**, 3093–3113, doi:10.1175/JAS-D-15-0185.1.

Chavas, D. R., N. Lin, and K. Emanuel, 2015: A model for the complete radial structure of the tropical cyclone wind field. Part I: Comparison with observed structure. *J. Atmos. Sci.*, **72 (9)**, 3647–3662, doi:10.1175/JAS-D-15-0014.1.

Chumakova, L. G., R. R. Rosales, and E. G. Tabak, 2013: Leaky rigid lid: New dissipative modes in the troposphere. *J. Atmos. Sci.*, **70 (10)**, 3119–3127.

Copernicus Climate Change Service, 2017: ERA5: Fifth generation of ECMWF atmospheric reanalyses of the global climate. Copernicus Climate Change Service Climate Data Store, URL https://cds.climate.copernicus.eu/cdsapp#!/home.

Crueger, T., and B. Stevens, 2015: The effect of atmospheric radiative heating by clouds on the Madden-Julian Oscillation. *J. of Advances in Modeling Earth Systems*, **7 (2)**, 854–864.

Davis, C., C. Snyder, and A. C. Didlake Jr, 2008: A vortex-based perspective of eastern Pacific tropical cyclone formation. *Mon. Wea. Rev.*, **136 (7)**, 2461–2477, doi:10.1175/2007MWR2317.1.

Davis, S. M., C. K. Liang, and K. H. Rosenlof, 2013: Interannual variability of tropical tropopause layer clouds. *Geophys. Res. Lett.*, **40 (11)**, 2862–2866.

DeMaria, M., and J. Kaplan, 1994: A Statistical Hurricane Intensity Prediction Scheme (SHIPS) for the Atlantic basin. *Wea. Forecasting*, **9 (2)**, 209–220, doi:10.1175/1520-0434(1994)009<0209:ASHIPS>2.0.CO;2.

DeMaria, M., J. A. Knaff, R. Knabb, C. Lauer, C. R. Sampson, and R. T. DeMaria, 2009: A new method for estimating tropical cyclone wind speed probabilities. *Wea. Forecasting*, **24 (6)**, 1573–1591, doi:10.1175/2009WAF2222286.1.

DeMaria, M., C. R. Sampson, J. A. Knaff, and K. D. Musgrave, 2014: Is tropical cyclone intensity guidance improving? *Bull. Amer. Meteor. Soc.*, **95 (3)**, 387–398, doi:10.1175/BAMS-D-12-00240.1.

DeMaria, M., and Coauthors, 2013: Improvements to the operational tropical cyclone wind speed probability model. *Wea. Forecasting*, **28 (3)**, 586–602, doi:10.1175/WAF-D-12-00116.1.

Edman, J. P., and D. M. Romps, 2017: Beyond the rigid lid: Baroclinic modes in a structured atmosphere. *J. Atmos. Sci.*, **74 (11)**, 3551–3566.

Eliassen, A., and E. Palm, 1960: On the transfer of energy in stationary mountain waves. *Geophy. Publ.*, **22**, 1–23.

Emanuel, K., 1986: An air-sea interaction theory for tropical cyclones. Part I: Steady-state maintenance. *J. Atmos. Sci.*, **43 (6)**, 585–605, doi:10.1175/1520-0469(1986)043<0585:AASITF>2.0.CO;2.

Emanuel, K., 2000: A statistical analysis of tropical cyclone intensity. *Mon. Wea. Rev.*, **128 (4)**, 1139–1152, doi:10.1175/1520-0493(2000)128<1139:ASAOTC>2.0.CO;2.

Emanuel, K., 2011: Global warming effects on US hurricane damage. *Weather*, **3 (4)**, 261–268.

Emanuel, K., 2013: Downscaling CMIP5 climate models shows increased tropical cyclone activity over the 21st century. *Proc. Natl. Acad. Sci. (USA)*, **110 (30)**, 12 219–12 224, doi:10.1073/pnas.1301293110.

Emanuel, K., 2017: A fast intensity simulator for tropical cyclone risk analysis. *Nat. Hazards*, **88 (2)**, 779–796, doi:10.1007/s11069-017-2890-7.

Emanuel, K., 2020: Slow modes of the equatorial waveguide. *J. Atmos. Sci.*, **77 (5)**, 1575–1582.

Emanuel, K., C. DesAutels, C. Holloway, and R. Korty, 2004: Environmental control of tropical cyclone intensity. *J. Atmos. Sci.*, **61 (7)**, 843–858, doi:10.1175/1520-0469(2004)061<0843:ECOTCI>2.0.CO;2.

Emanuel, K., R. Sundararajan, and J. Williams, 2008: Hurricanes and global warming: Results from downscaling IPCC AR4 simulations. *Bull. Amer. Meteor. Soc.*, **89 (3)**, 347–368, doi:10.1175/BAMS-89-3-347.

Emanuel, K., and F. Zhang, 2016: On the predictability and error sources of tropical cyclone intensity forecasts. *J. Atmos. Sci.*, **73 (9)**, 3739–3747, doi:10.1175/JAS-D-16-0100.1.

Emanuel, K., and F. Zhang, 2017: The role of inner-core moisture in tropical cyclone predictability and practical forecast skill. *J. Atmos. Sci.*, **74 (7)**, 2315–2324, doi:10.1175/JAS-D-17-0008.1.

Emanuel, K. A., 1987: An air-sea interaction model of intraseasonal oscillations in the tropics. *J. Atmos. Sci.*, **44 (16)**, 2324–2340.

Emanuel, K. A., J. David Neelin, and C. S. Bretherton, 1994: On large-scale circulations in convecting atmospheres. *Quart. J. Roy. Meteor. Soc.*, **120 (519)**, 1111–1143.

Fu, Q., M. Baker, and D. L. Hartmann, 2002: Tropical cirrus and water vapor: An effective earth infrared iris feedback? *Atmospheric Chemistry and Physics*, **2 (1)**, 31–37.

Fueglistaler, S., A. Dessler, T. Dunkerton, I. Folkins, Q. Fu, and P. W. Mote, 2009: Tropical tropopause layer. *Rev. Geophys.*, **47 (1)**.

Galarneau, T. J., and C. A. Davis, 2013: Diagnosing forecast errors in tropical cyclone motion. *Mon. Wea. Rev.*, **141 (2)**, 405–430, doi:10.1175/MWR-D-12-00071.1.

Gentry, M. S., and G. M. Lackmann, 2010: Sensitivity of simulated tropical cyclone structure and intensity to horizontal resolution. *Mon. Wea. Rev.*, **138 (3)**, 688–704, doi:10.1175/2009MWR2976.1.

Gill, A. E., 1980: Some simple solutions for heat-induced tropical circulation. *Quart. J. Roy. Meteor. Soc.*, **106 (449)**, 447–462.

Gneiting, T., and A. E. Raftery, 2005: Weather forecasting with ensemble methods. *Science*, **310 (5746)**, 248–249, doi:10.1126/science.1115255.

Goerss, J. S., 2000: Tropical cyclone track forecasts using an ensemble of dynamical models. *Mon. Wea. Rev.*, **128 (4)**, 1187–1193, doi:10.1175/1520-0493(2000)128<1187:TCTFUA>2.0.CO;2.

Goerss, J. S., 2007: Prediction of consensus tropical cyclone track forecast error. *Mon. Wea. Rev.*, **135 (5)**, 1985–1993, doi:10.1175/MWR3390.1.

Gopalakrishnan, S. G., F. Marks Jr, X. Zhang, J.-W. Bao, K.-S. Yeh, and R. Atlas, 2011: The experimental HWRF system: A study on the influence of horizontal resolution on the structure and intensity changes in tropical cyclones using an idealized framework. *Mon. Wea. Rev.*, **139 (6)**, 1762–1784, doi:10.1175/2010MWR3535.1.

Hamill, T. M., J. S. Whitaker, M. Fiorino, and S. G. Benjamin, 2011: Global ensemble predictions of 2009's tropical cyclones initialized with an ensemble kalman filter. *Mon. Wea. Rev.*, **139 (2)**, 668–688, doi:10.1175/2010MWR3456.1.

Hendon, H. H., and S. Abhik, 2018: Differences in vertical structure of the Madden-Julian Oscillation associated with the quasi-biennial oscillation. *Geophys. Res. Lett.*, **45 (9)**, 4419–4428.

Hendon, H. H., B. Liebmann, M. Newman, J. D. Glick, and J. Schemm, 2000: Medium-range forecast errors associated with active episodes of the Madden–Julian Oscillation. *Mon. Wea. Rev.*, **128 (1)**, 69–86.

Hendon, H. H., and M. L. Salby, 1994: The life cycle of the Madden–Julian oscillation. *J. Atmos. Sci.*, **51 (15)**, 2225–2237.

Hersbach, H., 2016: The ERA5 Atmospheric Reanalysis. *Amer. Geophys. Union Fall Meeting*, San Francisco, CA, Amer. Geophys. Union.

Hersbach, H., and Coauthors, 2020: The ERA5 global reanalysis. *Quart. J. Roy. Meteor. Soc.*, **146 (730)**, 1999–2049.

Horel, J. D., and J. M. Wallace, 1981: Planetary-scale atmospheric phenomena associated with the Southern Oscillation. *Mon. Wea. Rev.*, **109 (4)**, 813–829.

Hsu, P.-c., and T. Li, 2012: Role of the boundary layer moisture asymmetry in causing the eastward propagation of the Madden–Julian oscillation. *J. Climate*, **25 (14)**, 4914–4931.

Hung, M.-P., J.-L. Lin, W. Wang, D. Kim, T. Shinoda, and S. J. Weaver, 2013: MJO and convectively coupled equatorial waves simulated by CMIP5 climate models. *J. Climate*, **26 (17)**, 6185–6214.

Judt, F., S. S. Chen, and J. Berner, 2016: Predictability of tropical cyclone intensity: scale-dependent forecast error growth in high-resolution stochastic kinetic-energy backscatter ensembles. *Quart. J. Roy. Meteor. Soc.*, **142 (694)**, 43–57, doi:10.1002/qj.2626.

Khairoutdinov, M. F., and K. Emanuel, 2018: Intraseasonal variability in a cloud-permitting near-global equatorial aquaplanet model. *J. Atmos. Sci.*, **75 (12)**, 4337–4355.

Kieu, C. Q., and Z. Moon, 2016: Hurricane intensity predictability. *Bull. Amer. Meteor. Soc.*, **97 (10)**, 1847–1857, doi:10.1175/BAMS-D-15-00168.1.

Kiladis, G. N., J. Dias, K. H. Straub, M. C. Wheeler, S. N. Tulich, K. Kikuchi, K. M. Weickmann, and M. J. Ventrice, 2014: A comparison of OLR and circulation-based indices for tracking the MJO. *Mon. Wea. Rev.*, **142 (5)**, 1697–1715.

Kiladis, G. N., K. H. Straub, and P. T. Haertel, 2005: Zonal and vertical structure of the Madden–Julian oscillation. *J. Atmos. Sci.*, **62 (8)**, 2790–2809.

Kiladis, G. N., M. C. Wheeler, P. T. Haertel, K. H. Straub, and P. E. Roundy, 2009: Convectively coupled equatorial waves. *Rev. Geophys.*, **47 (2)**.

Klotzbach, P., S. Abhik, H. Hendon, M. Bell, C. Lucas, A. Marshall, and E. Oliver, 2019: On the emerging relationship between the stratospheric Quasi-Biennial oscillation and the Madden-Julian oscillation. *Sci. Rep.*, **9 (1)**, 1–9.

Knaff, J. A., C. R. Sampson, and G. Chirokova, 2017: A global statistical–dynamical tropical cyclone wind radii forecast scheme. *Wea. Forecasting*, **32 (2)**, 629–644, doi:10.1175/WAF-D-16-0168.1.

Knaff, J. A., C. R. Sampson, M. DeMaria, T. P. Marchok, J. M. Gross, and C. J. McAdie, 2007: Statistical tropical cyclone wind radii prediction using climatology and persistence. *Wea. Forecasting*, **22 (4)**, 781–791, doi:10.1175/WAF1026.1.

Kuang, Z., 2008a: Modeling the interaction between cumulus convection and linear gravity waves using a limited-domain cloud system–resolving model. *J. Atmos. Sci.*, **65 (2)**, 576–591.

Kuang, Z., 2008b: A moisture-stratiform instability for convectively coupled waves. *Journal of the Atmospheric Sciences*, **65 (3)**, 834–854.

Landsea, C. W., and J. L. Franklin, 2013: Atlantic hurricane database uncertainty and presentation of a new database format. *Mon. Wea. Rev.*, **141 (10)**, 3576–3592, doi:10.1175/MWR-D-12-00254.1.

Levitus, S., 1982: Climatological atlas of the world ocean. NOAA Professional Paper No. 13, U.S. Government Printing Office, 173 pp. doi:10.1029/EO064i049p00962-02.

Lim, Y., S.-W. Son, A. G. Marshall, H. H. Hendon, and K.-H. Seo, 2019: Influence of the QBO on MJO prediction skill in the subseasonal-to-seasonal prediction models. *Climate Dyn.*, **53 (3)**, 1681–1695.

Lin, J., and K. Emanuel, 2022: On the effect of surface friction and upward radiation of energy on equatorial waves. *J. Atmos. Sci.*

Lin, X., and R. H. Johnson, 1996: Heating, moistening, and rainfall over the western Pacific warm pool during TOGA COARE. *J. Atmos. Sci.*, **53 (22)**, 3367–3383.

Lindzen, R. S., and J. R. Holton, 1968: A theory of the quasi-biennial oscillation. *J. Atmos. Sci.*, **25 (6)**, 1095–1107.

Liu, Q., T. Marchok, H.-L. Pan, M. Bender, and S. Lord, 2000: Improvements in hurricane initialization and forecasting at NCEP with global and regional (GFDL) models. NWS Tech. Proc. Bull., No. 472, 7 pp. [Available from NWS Office of Meteorology, Science Division, Silver Spring, MD, 20910, or online at http://www.nws.noaa.gov/om/tpb/472body.html].

Madden, R. A., and P. R. Julian, 1971: Detection of a 40–50 day oscillation in the zonal wind in the tropical Pacific. *J. Atmos. Sci.*, **28 (5)**, 702–708.

Majumdar, S. J., and P. M. Finocchio, 2010: On the ability of global ensemble prediction systems to predict tropical cyclone track probabilities. *Wea. Forecasting*, **25 (2)**, 659–680, doi:10.1175/2009WAF2222327.1.

Mapes, B. E., 2000: Convective inhibition, subgrid-scale triggering energy, and stratiform instability in a toy tropical wave model. *J. Atmos. Sci.*, **57 (10)**, 1515–1535.

Mapes, B. E., and R. A. Houze, 1995: Diabatic divergence profiles in western Pacific mesoscale convective systems. *J. Atmos. Sci.*, **52 (10)**, 1807–1828.

Marks, D. G., 1992: The beta and advection model for hurricane track forecasting. NWS Tech. Memo. NWS NMC 70, 89 pp. [Available online at https://repository.library.noaa.gov/view/noaa/7184].

Marshall, A. G., H. H. Hendon, S.-W. Son, and Y. Lim, 2017: Impact of the quasi-biennial oscillation on predictability of the Madden–Julian oscillation. *Climate Dyn.*, **49 (4)**, 1365–1377.

Martin, Z., C. Orbe, S. Wang, and A. Sobel, 2021a: The MJO–QBO relationship in a GCM with stratospheric nudging. *J. Climate*, **34 (11)**, 4603–4624.

Martin, Z., S.-W. Son, A. Butler, H. Hendon, H. Kim, A. Sobel, S. Yoden, and C. Zhang, 2021b: The influence of the quasi-biennial oscillation on the Madden–Julian oscillation. *Nature Reviews Earth & Environment*, 1–13.

Matsuno, T., 1966: Quasi-geostrophic motions in the equatorial area. *Journal of the Meteorological Society of Japan. Ser. II*, **44 (1)**, 25–43.

Matsuno, T., 1970: Vertical propagation of stationary planetary waves in the winter northern hemisphere. *J. Atmos. Sci.*, **27 (6)**, 871–883.

Matthews, A. J., B. J. Hoskins, and M. Masutani, 2004: The global response to tropical heating in the Madden–Julian oscillation during the northern winter. *Quart. J. Roy. Meteor. Soc.*, **130 (601)**, 1991–2011.

Molteni, F., R. Buizza, T. N. Palmer, and T. Petroliagis, 1996: The ECMWF ensemble prediction system: Methodology and validation. *Quart. J. Roy. Meteor. Soc.*, **122 (529)**, 73–119, doi:10.1002/qj.49712252905.

Moskowitz, B. M., and C. S. Bretherton, 2000: An analysis of frictional feedback on a moist equatorial Kelvin mode. *Journal of the atmospheric sciences*, **57 (13)**, 2188–2206.

National Centers for Environmental Prediction, 2015: NCEP GFS 0.25 Degree Global Forecast Grids Historical Archive. Research Data Archive at the National Center for Atmospheric Research, Computational and Information Systems Laboratory, Boulder CO, doi:10.5065/D65D8PWK.

National Centers for Environmental Prediction, Japan Meteorological Agency, United Kingdom Met Office, China Meteorological Administration, Meteorological Service of Canada, Korea Meteorological Administration, Meteo-France, and European Centre for Medium-Range Weather Forecasts, 2008: THORPEX Interactive Grand Global Ensemble (TIGGE) Model Tropical Cyclone Track Data". Research Data Archive at the National Center for Atmospheric Research, Computational and Information Systems Laboratory, Boulder CO, doi:10.5065/D6GH9GSZ.

Neelin, J. D., and I. M. Held, 1987: Modeling tropical convergence based on the moist static energy budget. *Mon. Wea. Rev.*, **115 (1)**, 3–12.

Neelin, J. D., and J.-Y. Yu, 1994: Modes of tropical variability under convective adjustment and the Madden–Julian oscillation. Part I: Analytical theory. *J. Atmos. Sci.*, **51 (13)**, 1876–1894.

Neelin, J. D., and N. Zeng, 2000: A quasi-equilibrium tropical circulation model—Formulation. *J. Atmos. Sci.*, **57 (11)**, 1741–1766.

Neena, J., J. Y. Lee, D. Waliser, B. Wang, and X. Jiang, 2014: Predictability of the Madden–Julian oscillation in the intraseasonal variability hindcast experiment (ISVHE). *J. Climate*, **27 (12)**, 4531–4543.

Nishimoto, E., and S. Yoden, 2017: Influence of the stratospheric quasi-biennial oscillation on the madden–julian oscillation during austral summer. *Journal of the Atmospheric Sciences*, **74 (4)**, 1105–1125.

Pielke, R. A., J. Gratz, C. W. Landsea, D. Collins, M. A. Saunders, and R. Musulin, 2008: Normalized hurricane damage in the United States: 1900–2005. *Nat. Hazards Rev.*, **9 (1)**, 29–42, doi:10.1061/(ASCE)1527-6988(2008)9:1(29).

Rappaport, E. N., and Coauthors, 2009: Advances and challenges at the National Hurricane Center. *Wea. Forecasting*, **24 (2)**, 395–419, doi:10.1175/2008WAF2222128.1.

Raymond, D. J., 2001: A new model of the Madden–Julian oscillation. *J. Atmos. Sci.*, **58 (18)**, 2807–2819.

Raymond, D. J., and Ž. Fuchs, 2007: Convectively coupled gravity and moisture modes in a simple atmospheric model. *Tellus A: Dynamic Meteorology and Oceanography*, **59 (5)**, 627–640.

Reynolds, R. W., V. F. Banzon, and N. C. Program, 2008: NOAA Optimum Interpolation 1/4 Degree Daily Sea Surface Temperature (OISST) analysis, version 2. NOAA National Centers for Environmental Information, doi:10.7289/V5SQ8XB5.

Sakaeda, N., J. Dias, and G. N. Kiladis, 2020: The unique characteristics and potential mechanisms of the MJO-QBO relationship. *J. Geophys. Res.*, **125 (17)**, e2020JD033 196.

Sampson, C. R., and A. J. Schrader, 2000: The automated tropical cyclone forecasting system (version 3.2). *Bull. Amer. Meteor. Soc.*, **81 (6)**, 1231–1240, doi:10.1175/1520-0477(2000)081<1231:TATCFS>2.3.CO;2.

Simpson, R., and R. Riehl, 1958: Mid-tropospheric ventilation as a constraint on hurricane development and maintenance. Preprints, *Tech. Conf. on Hurricanes*, Miami Beach, FL, Amer. Meteor. Soc., D4-1–D4-10.

Sippel, J. A., and F. Zhang, 2008: A probabilistic analysis of the dynamics and predictability of tropical cyclogenesis. *J. Atmos. Sci.*, **65 (11)**, 3440–3459, doi: 10.1175/2008JAS2597.1.

Sobel, A., and E. Maloney, 2013: Moisture modes and the eastward propagation of the MJO. *J. Atmos. Sci.*, **70 (1)**, 187–192.

Sobel, A., S. Wang, and D. Kim, 2014: Moist static energy budget of the mjo during dynamo. *J. Atmos. Sci.*, **71 (11)**, 4276–4291.

Sobel, A. H., and C. S. Bretherton, 2000: Modeling tropical precipitation in a single column. *J. Climate*, **13 (24)**, 4378–4392.

Sobel, A. H., J. Nilsson, and L. M. Polvani, 2001: The weak temperature gradient approximation and balanced tropical moisture waves. *J. Atmos. Sci.*, **58 (23)**, 3650–3665.

Son, S.-W., Y. Lim, C. Yoo, H. H. Hendon, and J. Kim, 2017: Stratospheric control of the Madden–Julian oscillation. *J. Climate*, **30 (6)**, 1909–1922.

Straub, K. H., and G. N. Kiladis, 2002: Observations of a convectively coupled Kelvin wave in the eastern Pacific ITCZ. *J. Atmos. Sci.*, **59 (1)**, 30–53.

Swinbank, R., and Coauthors, 2016: The TIGGE project and its achievements. *Bull. Amer. Meteor. Soc.*, **97 (1)**, 49–67, doi:10.1175/BAMS-D-13-00191.1.

Tang, B., and K. Emanuel, 2010: Midlevel ventilation's constraint on tropical cyclone intensity. *J. Atmos. Sci.*, **67 (6)**, 1817–1830, doi:10.1175/2010JAS3318.1.

Tang, B., and K. Emanuel, 2012: A ventilation index for tropical cyclones. *Bull. Amer. Meteor. Soc.*, **93 (12)**, 1901–1912, doi:10.1175/BAMS-D-11-00165.1.

Titley, H. A., R. L. Bowyer, and H. L. Cloke, 2020: A global evaluation of multi-model ensemble tropical cyclone track probability forecasts. *Quart. J. Roy. Meteor. Soc.*, **146 (726)**, 531–545.

Tracton, M. S., and E. Kalnay, 1993: Operational ensemble prediction at the National Meteorological Center: Practical aspects. *Wea. Forecasting*, **8 (3)**, 379–398, doi: 10.1175/1520-0434(1993)008<0379:OEPATN>2.0.CO;2.

Tseng, H.-H., and Q. Fu, 2017: Temperature control of the variability of tropical tropopause layer cirrus clouds. *J. Geophys. Res.*, **122 (20)**, 11–062.

Vallis, G. K., 2017: *Atmospheric and oceanic fluid dynamics*. Cambridge University Press.

Van Sang, N., R. K. Smith, and M. T. Montgomery, 2008: Tropical-cyclone intensification and predictability in three dimensions. *Quart. J. Roy. Meteor. Soc.*, **134 (632)**, 563–582, doi:10.1002/qj.235.

Vigh, J. L., and Coauthors, 2020: The Hurricane Risk Calculator: Working toward enhancing our nation's readiness, responsiveness, and resilience to hurricanes through probabilistic risk frameworks for evacuation decision support. *100th Amer. Meteor. Soc. Annual Meeting*, Boston, MA, Amer. Meteor. Soc., https://ams.confex.com/ams/2020Annual/webprogram/Paper370408.html.

Vijaya Kumar, T., T. Krishnamurti, M. Fiorino, and M. Nagata, 2003: Multimodel superensemble forecasting of tropical cyclones in the Pacific. *Mon. Wea. Rev.*, **131 (3)**, 574–583, doi:10.1175/1520-0493(2003)131<0574:MSFOTC>2.0.CO;2.

Virts, K. S., and J. M. Wallace, 2010: Annual, interannual, and intraseasonal variability of tropical tropopause transition layer cirrus. *J. Atmos. Sci.*, **67 (10)**, 3097–3112.

Virts, K. S., and J. M. Wallace, 2014: Observations of temperature, wind, cirrus, and trace gases in the tropical tropopause transition layer during the MJO. *J. Atmos. Sci.*, **71 (3)**, 1143–1157.

Vitart, F., and Coauthors, 2017: The subseasonal to seasonal (S2S) prediction project database. *Bull. Amer. Meteor. Soc.*, **98 (1)**, 163–173.

Wang, B., 1988: Dynamics of tropical low-frequency waves: An analysis of the moist Kelvin wave. *J. Atmos. Sci.*, **45 (14)**, 2051–2065.

Wang, B., and H. Rui, 1990: Dynamics of the coupled moist Kelvin–Rossby wave on an equatorial β-plane. *J. Atmos. Sci.*, **47 (4)**, 397–413.

Wang, S., M. K. Tippett, A. H. Sobel, Z. K. Martin, and F. Vitart, 2019: Impact of the qbo on prediction and predictability of the mjo convection. *J. Geophys. Res.*, **124 (22)**, 11 766–11 782.

Wheeler, M., and G. N. Kiladis, 1999: Convectively coupled equatorial waves: Analysis of clouds and temperature in the wavenumber–frequency domain. *J. Atmos. Sci.*, **56 (3)**, 374–399.

Wheeler, M. C., and H. H. Hendon, 2004: An all-season real-time multivariate MJO index: Development of an index for monitoring and prediction. *Mon. Wea. Rev.*, **132 (8)**, 1917–1932.

Wilks, D. S., 2011: *Statistical Methods in the Atmospheric Sciences*, Vol. 100. Academic Press.

Williford, C. E., T. Krishnamurti, R. C. Torres, S. Cocke, and Coauthors, 2003: Real-time multimodel superensemble forecasts of Atlantic tropical systems of 1999. *Mon. Wea. Rev.*, **131 (8)**, 1878, doi:10.1175//2571.1.

Winker, D. M., M. A. Vaughan, A. Omar, Y. Hu, K. A. Powell, Z. Liu, W. H. Hunt, and S. A. Young, 2009: Overview of the CALIPSO mission and CALIOP data processing algorithms. *J. Atmos. Oceanic Technol.*, **26 (11)**, 2310–2323.

Xu, K.-m., and K. A. Emanuel, 1989: Is the tropical atmosphere conditionally unstable? *Mon. Wea. Rev.*, **117 (7)**, 1471–1479.

Yamaguchi, M., T. Nakazawa, and S. Hoshino, 2012: On the relative benefits of a multi-centre grand ensemble for tropical cyclone track prediction in the western North Pacific. *Quart. J. Roy. Meteor. Soc.*, **138 (669)**, 2019–2029.

Yang, G.-Y., B. Hoskins, and L. Gray, 2012: The influence of the QBO on the propagation of equatorial waves into the stratosphere. *J. Atmos. Sci.*, **69 (10)**, 2959–2982.

Yano, J.-I., and K. Emanuel, 1991: An improved model of the equatorial troposphere and its coupling with the stratosphere. *J. Atmos. Sci.*, **48 (3)**, 377–389.

Yoo, C., and S.-W. Son, 2016: Modulation of the boreal wintertime Madden-Julian oscillation by the stratospheric quasi-biennial oscillation. *Geophys. Res. Lett.*, **43 (3)**, 1392–1398.

Zhang, C., 2005: Madden-julian oscillation. *Reviews of Geophysics*, **43 (2)**.

Zhang, C., and M. Dong, 2004: Seasonality in the Madden–Julian oscillation. *J. Climate*, **17 (16)**, 3169–3180.

Zhang, F., and J. A. Sippel, 2009: Effects of moist convection on hurricane predictability. *J. Atmos. Sci.*, **66 (7)**, 1944–1961, doi:10.1175/2009JAS2824.1.

Zhang, F., and D. Tao, 2013: Effects of vertical wind shear on the predictability of tropical cyclones. *J. Atmos. Sci.*, **70 (3)**, 975–983, doi:10.1175/JAS-D-12-0133.1.